LABEL FREE OPTICAL DETECTION OF ELECTRICAL ACTIVITY IN MAMMALIAN NEURONS

by

SARMISHTHA SATPATHY

Presented to the Faculty of the Graduate School of

The University of Texas at Arlington in Partial Fulfillment

of the Requirements

for the Degree of

DOCTOR OF PHILOSOPHY

THE UNIVERSITY OF TEXAS AT ARLINGTON

December 2017

Dedicated to my mother, the best teacher I have ever had.

Acknowledgements

This work is the result of collaborative effort, whether directly or indirectly, by a lot of people. I was lucky to have worked with so many brilliant minds, and would like to thank UT Arlington for giving me this opportunity in the first place. I was blessed with the support of the Electrical, BE and the Physics departments. And while there are far too many people to name individually, please understand that I truly appreciate your help and guidance in making the journey easier.

To my committee- Dr. Yuze Sun, Dr. Michael Vasilyev and Dr. Juhyun Lee - thank you all for your interest in me and your timely guidance and wisdom. You have been truly supportive and I am glad I had your direction to keep me going. To Dr. Weidong Zhou- yours was the first optics class I took in UTA, and I fell decidedly in love with optics. Thank you for always being available for me and for being my co-supervisor.

To Dr. Samarendra Mohanty- I would not have dared to start my PhD if not for you. Thank you for believing in me, introducing me to the wonderful world of biophotonics and imparting so many skills in so little time. Your tough love helped me get through many milestones in a very short time, and has instilled a thirst to do better, every time.

To Dr. Digant Dave- no thanks is enough to acknowledge the role you played in my life. Getting my PhD has been a lifelong dream and you brought me to the finish line with your hardwork and mentorship. I have enjoyed spending this time with you, and it has been educational on so many levels. Thank you for inspiring me with your pure love and enthusiasm for optics, innovation and research, your kindness and humanity. I am so proud of being your mentee.

To our various collaborators, specially Dr. Young Tae Kim and Dr. Robert Bachoo, thank you so much for making these experiments possible. The work you do is not easy, and I really appreciate your skill, your wisdom and support.

To my labmates and colleagues- Bryan Black and Kamal Dhakal- thank you for training me to take over the reins. Loan and James- I truly admire your dedication to your work. Thank you for lending me your precious time and expertise. To Subrata- I learnt so much from you. I was in constant awe of how well rounded and skilled you are, with equal amounts of talent and effort. Thank you for your help and guidance with many, many things. I cherished your company and wisdom. I am glad I got to work with all of you.

To my teachers thoughout the years, and the guides and mentors in different forms and shapes- thank you. Know that I remember you and your teachings.

To my friends, at every stage in life- thank you for your company in the good times, and the bad. Many of you have inspired me to be better and kinder.

To my sisters and the families they begot- I love you, and am eternally grateful to you. The cost of my education has been distance from you and the kids, and that is the only part I regret.

To my extended family and my in laws- thank you so much for your love and for taking pride in the smallest of my achievements and giving me my dopamine fix for the right reasons!

To Om- my life is so much better with you in it. With due respect to everything, I don't think any of this would matter as much if I couldn't share it with you. I feel grateful to have you as my partner.

To my parents- my father, who inspired and guided me even in his absence, and my mother who did it with her sheer presence, perseverance and indomitable spirit - thank you doesn't begin to cover it. I owe everything I have and am to you, and I am proud to say that I am the result of your toil. I can only hope you feel the same way.

November 20, 2017

Abstract

LABEL FREE OPTICAL DETECTION OF ELECTRICAL ACTIVITY IN MAMMALIAN NEURONS

Sarmishtha Satpathy, PhD

The University of Texas at Arlington, 2017

Supervising Professor: Digant P. Dave'

We describe an optical technique for label-free detection of the action potential in cultured mammalian neurons. Induced morphological changes due to action potential propagation in neurons are optically interrogated with a phase sensitive interferometric technique. Optical recordings composed of signal pulses mirror the electrical spike train activity of individual neurons in a network. The optical pulses are transient nanoscale oscillatory changes in the optical path length of varying peak magnitude and temporal width. Exogenous application of glutamate to cortical neuronal cultures produced coincident increase in the electrical and optical activity; both were blocked by application of a Na-channel blocker, Tetrodotoxin. The observed transient change in optical path length in a single optical pulse is primarily due to physical fluctuations of the neuronal cell membrane mediated by a yet unknown electromechanical transduction phenomenon. Our analysis suggests a traveling surface wave in the neuronal cell membrane is responsible for the measured optical signal pulses.

In addition, we describe various optical techniques that may be used to design and create a neural circuit, and manipulate it with various inputs to decode the transfer function of the circuit. Together, these techniques, with the proposed optical detection technique can help understand the neural signaling in simple neural networks.

Preface

The text and figures included in this dissertation are drawn heavily from works (published), listed below in which, I (Sarmishtha Satpathy) am primary or secondary author, and principal experimental contributor. No duplicacy, infringement, or redundancy is intended. Permissions have been obtained from the responsible entities and publications to include the work in this dissertation.

Journal Publications:

1. Batabyal, Subrata, Sarmishtha Satpathy, Loan Bui, Young-Tae Kim, Samarendra Mohanty, Robert Bachoo, and Digant P. Davé. "Label-free optical detection of action potential in mammalian neurons." *Biomedical optics express* 8, no. 8 (2017): 3700-3713.
2. Satpathy, Sarmishtha, Subrata Batabyal, Kamal R. Dhakal, John Lin, Young-tae Kim, and Samarendra K. Mohanty. "Broad spectral excitation of opsin for enhanced stimulation of cells." *Optics letters* 40, no. 11 (2015): 2465-2468.

Table of Contents

Acknowledgements ..... **iv**

Abstract ..... **vi**

Preface ..... **vii**

List of Illustrations ..... **x**

Chapter 1 Introduction **16**

1.1 Overview **16**

Chapter 2 System description **24**

2.1 Introduction to interferometry **24**

2.1.1 History of Interferometry 24

2.2 Fundamentals of Optical Interferometry 26

2.2.2 Common path geometry: 29

2.2.3 Phase sensitive FDI: 30

2.2.3.2 Sensitivity drop off as a function of depth: 35

2.2.3.2 Remapping to k-space: 37

2.3 Phase Sensitive Spectral Domain Low Coherence Interferometry system setup **40**

2.3.1 Choosing sample housing 43

2.3.1.1 Fabrication of neuronal cell culture device 48

2.4 Data analysis **49**

Chapter 3 Label free optical detection of cellular activity in mammalian neurons **52**

3.1 Methods and materials: **53**

3.1.1 Cortical neuron culture 53

3.1.2 Immunostaining of fixed cortical neuron 53

3.1.3 Patch-clamp recording 54

3.2 Results **56**

3.3. Discussion **62**

3.3.1 Estimation of physical displacement from measured optical path-length changes 68

Chapter 4 All Optical construction, manipulation, stimulation and detection of electrical activity in a neural circuit **72**

4.1 Introduction **72**

4.2 Optical positioning **74**

4.2.1 Materials and methods 76

4.2.1.1 Rat Cortical Neuron culture 76

4.2.1.2 Optical setup 76

4.2.2 Results for optical trapping 78
4.3 Optoporation 80
4.3.1 Introduction 80
4.3.2 Materials and methods 81
4.3.2.1 Sample preparation 81
4.3.2.2 Optical setup 81
4.3.3 Results 82
4.4 Optical Stimulation 85
4.4.1 Optogenetics 85
4.4.1.2 Methods 87
4.4.1.3 Results 88
4.4.2 FS NIR stimulation 92
4.4.2.1 Methods and materials 92
4.4.2.2 Results 94
4.5 Optical detection of optogenetically stimulated activity 97
4.5.1 Materials and methods 98
4.5.2 Results and discussions 99
4.5. Conclusion 103
Chapter 5 Conclusion 105
Appendix A License and copyright of materials 108
References 110
Biographical Information 118

List of Illustrations

Figure 2.1: Illustration of Fourier transform relationship between the Gaussian-shaped coherence function γ(z) (characterized by the coherence length l_c), and the light source spectrum S(k) (characterized by the central wavenumber k_0 and wavenumber bandwidth Δk).....36

Figure 2.2: (top) Intensity spectrum of SLD source as captured by a known spectrometer (Oceanoptics USB 4000) and (bottom) as recorded in the photodetector array as a function of pixels. As it can be noticed by comparing the top and bottom figures, the spectrum is flipped in the x axis. The peaks and the middle valley, as well as the half power points can be used as the feature points for remapping to k-space.....39

Figure 2.3: Basler camera response. The portion in red corresponds to the wavelength range of the source. 40

Figure 2.4: Spectrometer setup: BD- Beam Dumper, 50:50 Coupler, SLD- Superluminescent Diode, FC- Fiber Coupler, DG- Diffraction Grating, CCD- Charge Coupled Device.....41

Figure 2.5: Schematic diagram of the interferometric instrument which consists of a (A) broadband SLD source, fiber coupler, high-speed spectrometer and computer for data acquisition. (B) Output port of the fiber coupler is attached to the side port of an inverted microscope that transmits and focusses light on the soma of a neuron (C) Illustration of neuronal cell culture device in a sandwich configuration consisting of two glass slides that are separated by a fixed gap (~80 μm) with neurons attached to the bottom glass slide, and (D) Light reflecting from the bottom (glass-cell) and top (cell-media) interfaces of the

two glass slides of the neuronal cell culture device couple back into the interferometer and mix to form spectral interference fringe signal. 42
Figure 2.6: Characterization of artifact from borosilicate glass. (A) Change in OPL in soda lime glass on stimulation by laser (represented by bars in blue). (B) Change in OPL in Borosilicate glass on stimulation by laser (represented by bars in blue). The OPL drastically changes on laser impingement. (C) and (D) show the increase of OPL change in the borosilicate class on increasing the exposure time and the intensity of the laser respectively. 45
Figure 2.7: Schematic showing reflection of beam from various surfaces in (A) coverslip and (B) sandwich arrangements. nc, nw, ng, na are the refractive indices of cell, water, glass and air respectively. dcs and dsw are thickness between reflective surfaces of coverslip and sandwich. RR and RS are reflectivity encountered by reference and sample beams respectively. 47
Figure 2.8: (A) Two slides are cleaned, sanitized and dried. (B) Two holes are drilled on to the top slide, and a thin layer of nontoxic silicon glue is applied on the top layer of the bottom slide. (C) PDMS reservoirs are centered and plasma glued on to the top slide, centered around each hole. (D) The two slides are then pressed together and allowed to dry in a sterile environment for 24-48 hours. (E) Neurons are seeded into one of the PDMS reservoirs. (F) The cell culture device is incubated at 37 ℃ for 7-14 days in an incubator with appropriate amount of humidity and CO_2. 49
Figure 2.9: Data collection and signal processing flowchart. (a)-(i) individual sequential steps involved in collection and processing of the optical signal from the sample. (k) An example of typical optical signal in presence of Glutamate stimulation with the thresholding and envelope detection. (l) An example of typical optical signal in presence of TTX inhibition with the thresholding and envelope detection. 50

Figure 3.1: Representative optical signals recorded from individual neurons in a network. (A) Fluorescence immuno-stained (primary β-III-tubulin antibody- Alexa Fluor 488) image of networked rat cortical neurons used in our experiments. (B) & (C) Temporal change in OPD under different experimental conditions (no cell, cell without any stimulation, cell with Glutamate stimulation, cell with TTX inhibition) showing a non-periodic train of optical signal oscillation from unstimulated and stimulated neurons which die out when inhibited with TTX. (D) Isolated burst of individual optical pulses that have wave packet like signal pulse characteristics and their corresponding envelopes show variation in temporal pulse width. 58
Figure 3.2: Patch clamp recording of action potential firing from single neurons. (A) Pre- and post-glutamate stimulation voltage recording (current clamp) of randomly generated action potential spikes in networked neurons. (B) Inhibition of electrical activity with addition of TTX. Recordings in (A) and (B) are from two separate experiments. 60
Figure 3.3: Analysis of extracted features from individual optical pulse (Fig. 2) (N=5 neurons). (A) Optical signals are rectified, followed by envelope detection of each pulse. (B) Firing rate of unstimulated vs stimulated/inhibited neurons, ($p<0.05$ for -Glu vs +Glu and -Glu vs +TTX). (C)-(D) scatter plots of envelope width, envelope peak under no stimulation, Glutamate stimulation, and TTX inhibition conditions, respectively. 61
Figure 3.4: Analysis of extracted features from individual optical pulse (Fig. 2) (N=5 neurons). (A) Optical signals are rectified, followed by envelope detection of each pulse. (B) Firing rate of unstimulated vs stimulated/inhibited neurons, ($p<0.05$ for -Glu vs +Glu and -Glu vs +TTX). (C)-(D) scatter plots of envelope width, envelope peak under no stimulation, Glutamate stimulation, and TTX inhibition conditions, respectively. 63
Figure 3.5: Optical pulses of varying temporal characteristics (A) Raw (blue) and filtered (orange) 60 sec extract of optical recording from a signal neuron showing a train of

randomly spaced optical pulses, (i-iv) Zoomed section of select windows from optical recordings in (A) showing single or multicyclic oscillation of optical pulses with varying temporal widths (scale-bar=50 ms). The red overlay is a filtered version of the unfiltered (blue) signal. 66
Figure 3.6: Illustration of two different types of cellular deformation under isovolumetric condition which can result in measured OPD changes. (A) Geometry of the neuron used to calculate change in physical thickness for whole cell (B) and membrane (C) deformation, respectively. 69
Figure 4.1: A flowchart diagram outlining the major components of an all optical neural circuit construction, manipulation and read out system. 74
Figure 4.2: A schematic diagram showing the optical setup to implement optical trapping system used. BFL- Bright-field Lamp, CL- Condenser Lens, BE- Beam Expander. 75
Figure 4.3: A schematic diagram showing the principle of optical trapping system used to position cells at preassigned locations. MO: Microscope Objective. 78
Figure 4.4: Patterns achieved by optically trapping and positioning of rat cortical neurons- (A) straight line, (B) Rabbit paw (C) Triangle. (D) Single neuron held in an optical trap. Scale bar: 10 μm. 79
Figure 4.5: Astrocyte-neuron co-culture. Neurons are cultured on a petridish and astrocytes are optically trapped and placed sequentially on the axon and dendritic networks. Scale bar: 10 μm. 80
Figure 4.6: Demonstration of optoporation in retinal cells of rat eye. (A)-(I) Fluorescence images demonstrating the step by step delivery of Alexa 594 Phalloidin in neurons to create a circular pattern. (J) Brightfield and fluorescence image before the optoporation, and (K) Brightfield and fluorescence image after the optoporation to show that the dye

has permeated the cells. Optoporation is performed with a 10X microscope objective (0.25 NA) objective. Scale bar: 50 μm. 83
Figure 4.7: Demonstration of optoporation in retinal cells of rat eye. (A)-(H) fluorescence images demonstrating the step by step delivery of Rhodamine Phalloidin in neurons to create a pyramidal pattern. (I) Brightfield and fluorescence image before the optoporation to demonstrate the lack of dye in the neurons. Optoporation is performed with a 20X microscope objective (0.5 NA). Scale bar: 50 μm. 84
Figure 4.8: Quantitative comparison between broad-band and narrow-band optogenetic activation. Representative light-induced inward current in a ReaChR-expressing HEK cell upon illumination of (a) broad-band white light, and spectrally-filtered narrow-band blue, green and red light. Inset: Zoomed current profile for spectrally-filtered narrow-band blue, green and red light (pulse width: 100 ms). (b) Measured inward peak-current in ReaChR-HEK cell upon light stimulation with different spectral profiles at varied intensity levels. (c) Channel-on and (d) channel-off rate for ReaChR-HEK cell upon light stimulation with different spectral profiles and intensity levels. N=10 for each light wavelength and intensity. Average ± S.D. *p<0.01 between white and others. #p<0.01. 90
Figure 4.9: Optical setup for femtosecond laser stimulation of neurons. BF Lamp- Bright Field Lamp, Con- Condenser, Obj- Objective, Em F1- Emission Filter 1, Em F2- Emission Filter 2, FL- Fluorescence Lamp, DM1- Dichroic Mirror 1, DM2- Dichroic Mirror 2, DM3- Dichroic Mirror 3. Inset- Laser beam as seen on the camera at a low exposure. 94
Figure 4.10: (A) Electrical activity recorded from a neuron before fs stimulation (control). (B) Image of the neuron being stimulated and patched. The red lightning bolt represents the laser stimulation and the blue triangle represents the position of the electrode. (C) NIR stimulated neuron, a neighboring neuron attached to it that is being recorded. 95

Figure 4.11: Electrical activity recorded from a neuron after fs stimulation. (right) Zoomed in voltage recording of a single action potential firing.....95
Figure 4.12: Electrical activity recorded from a neuron after stimulating a neighboring, synaptically attached neuron is stimulated by fs stimulation. (right) Zoomed in voltage recording of a single action potential firing. 96
Figure 4.13: Optical signal recorded from the neuron soma-axon junction without (green) and with (blue) laser stimulation. 100
Figure 4.14: Zoomed in regions of the recorded optical signal are displayed. The region zoomed is represented by the yellow rectangle. 101
Figure 4.15: Single optical pulses displaying positive and negative lobes. (i)-(iii) are taken from the signal recorded after laser stimulation, while (iv) is taken from signal recorded before stimulation.....102

Chapter 1

Introduction

1.1 Overview

Neural networks have engaged the curiosities of researchers for many decades now, as it offers solutions to a wide range of issues- from diagnosing, treating and preventing diseases and anomalies, to generating better human-machine interfaces, creating smarter and more intuitive prosthetics, to mimicking the most efficient computer known to man- the human brain. It holds the key to unlock the full potential of the human brain and to better understand the mechanism and functioning of the the 100 billion neurons (and 10X that number of glial cells)[1] that seem to determine almost every apect of human behavior, functioning and existence. Scientists approach this challenge in one of two ways- Reductionist, or Holistic[2]. The Holistic approach studies the brain as a system instead of looking at individual elements. This is a top down approach. Reductionist approach is a bottom-up approach that studies the building bricks of the brain, i.e., the neurons, and builds up to better understand the behaviour of the more complex circuits and the brain as a whole.

In order to understand the behaviour of neural networks, it is essential to study the communication and signaling occuring in these networks[3], which propagates on the basis of electro-chemical gradients[4]. It is critical to stimulate and detect this cellular activity in sub-millisecond timescale and micrometer resolution without using invasive means in order to study these networks without external factors disrupting the indigenous environment, giving a faithful representation of unbiased cellular communication.

The most widely used existing methods for studying *in vitro* neuronal activity can be clasified as: (1) Electrical (2) Chemical (optical) and (3) Intrinsic optical imaging methods.

Electrical methods like patch clamp recording and multi-electrode arrays are considered to be the gold standard for measuring cellular activity in single cells because of high spatial and temporal specificity, fidelity and relative ease of measurement. These give precise, direct measurement of the actual voltage and current across the membrane, in real time, with microsecond time resolution and high spatial specificity. This is a direct measurement of the electrical potentials, unlike other methods which measure these changes indirectly, and then convert the signal to an electrical equivalent[5] if needed. It is even possible to determine which ion channel group is responsible for the signal, and to collect the signal from single ion channel[6], which provides great insight into the mechanics of electrical behaviour of neurons. Owing to all these unique advantages, this has been the preffered technique to study neurons[6]. Hodgkin-Huxley derived their widely accepted HH model for neurons that gives us an idea of the action potential by employing electrodes to study the electrical behaviour of a neuron in a circuit[6]. That said, these methods are generally invasive and disruptive in nature and the throughput is limited by the number of electrical probes (electrodes), which makes it challenging to capture unaltered cellular responses in an indigenous environment[7]. Also, it is arduous to study multiple cells in a region as it would mean puncturing the cells with different electrodes to collect the data which poses logistical, noise and ergonomical issues[6]. Studying the same in vitro sample for extended period of time also is a challenge as the patch cannot be mainatined for more than a few hours at a time[8]. This is a very important aspect of in-vitro studies specially for applications like drug effect studies and behavioral studies. Apart from that, the intergrity of the signal recorded might be compromised by the stress of the damage to the cell, which might add artifacts/responses that might not have been a part of the natural response of the cell in an indigeneous, unaltered and stress-free environment. To overcome some of these challenges, platforms like MEAs have been

developed[9]. Multi electrode arrays (MEA) are arrays of electrodes on a glass, silicone or plastic base on which cells can be cultured and electrical stimulations and recording can be done from the cells that are seated on these electrodes[5]. This improves the efficiency by making multiple sites accesible to recording, is mostly non invasive and simplifies the recording process by eliminating the need to patch the cell, but it is still not an ideal method for neural action potential recording as it sacrifices spatial specificity and depends on the cell being grown on the electrode, which is an arbitrary process. The size of the MEA also limits the area of the neural network that can be studied, which resticts studies of different parts of the brain/ neural network simultaneously. This is a very important aspect in neurological studies as the interdependence of different regions of the brain, the coherence and and seriality of the signaling can be indicative of the degree of health and revealing of disease states.

A widefield method that can make simultaneous measurements from multiple spots without introducing injury or stress is thus of great interest, and can be achieved by non contact techniques like optical detection. Optical changes during membrane potential changes have been observed and exploited to detect membrane potential by many researchers, since 1950s and earlier[10]. Historically, these changes have been too small to be measured on their own. Aided with contrast agents, dyes and fluorescent markers, these changes become more visible and meaningfully measurable, while still requiring signal averaging and long stimulation and exposure times. Other techniques employ fluorescence of externally applied dyes or molecules to optically image membrane potential changes. Chemical methods provide an optical (though not label free) method of detecting cellular activity with high throughput,and have been universally accepted since their introduction in the late 1970s[11]. These methods use an exogenous dye or fluorescent protein (essentially molecular reporters) to generate or enhance optical

signals representative of electrical activity in cells. Due to their ease of use and high throughput detection of membrane voltage in cellular networks and tissues, these have been ubiquitously[12,13] used by researchers trying to decode neural communications. These can be broadly classified as calcium indicators and voltage indicators. While calcium indicators mainly represent the flow of calcium currents which are modulated by the propagation of cellular/neural firing, voltage indicators are indicative of actual membrane potential in the cells. Intracellular Ca^{2+} ion is a universal secondary messenger that can be studied by using calcium indicators which are a hybrid of Ca^{2+} binding molecules tagged with chromophores that indicate a binding event with a change in absorption/emission[14,15]. Calcium imaging is often implemented as bulk imaging technique to monitor the relative activity of cell clusters[16]. Voltage indicators have their fluorescence states directly coupled to the membrane potentials and hence give a more accurate measurement of neural signaling. Although the initial constructs had many drawbacks like low SNR, high cytotoxicity, low retention, deletrious compartmentalization[17], slow kinetics, and high autofluorescence leading to background noise, over the decades many iterations have led to improved varieties like Genetically Encoded Voltage Indicators (GEVI) and Genetically Encoded Calcium Indicators (GECI)[18], along with the more recent developments like Rhodopsin based Fluorescent Proteins which have overcome many of the challenges with better SNR, and temporal resolution, genetically selective target, reduced cytotoxicity, photobleaching and phototoxicity[17]. Using the 100+ available options for GECIs, calcium imaging[17] and voltage sensing, many research groups have been able to map signaling in brain and brain models, as well as membrane voltage at the circuit and system level[19,20]. Coupled with other optical techniques like optogenetics, it is now possible to build all optical

stimulation and detection neural interfaces[21] for studying neural functions and brain mapping, even achieving 3D imaging in rodent brain[22].

However, despite the many recent improvements, there are several drawbacks associated with using external fluorescent markers or labels, like photo-bleaching and photo-toxicity, as well as with the inherent characteristics like high background fluorescence and low intensity of the fluorescence, which necessitate the use of high exposure time, signal averaging and also specific imaging techniques like two photon microscopy to reduce/reject background noise and enhance the signal from the plane of interest[14,23]. Also, one of the major concerns with using external markers is the pharmacological or photodynamic effect they may have on the functionality of the sample[24]. While certain assays can be used to determine cell health and viability, there is very little knowledge that can be procured from such tests regarding any changes to functional behavior of the sample cells, or to check if the added marker interferes with the inherent characteristics of sub cellular processes. With these considerations in sight, researchers have been trying to achieve label free, noninvasive detection of cellular activity as label free detection is always preferable if an optical signal reflective of individual action potential spikes can be reliably recorded.

Intrinsic optical imaging techniques have been used far and wide for detecting cellular activity by measuring inherent changes to optical properties that are modulated during action potential propagation. These methods use a probing beam to measure optical, mechanical and/or physiological property changes that occur in a cell or a region of a biological sample in concurrence or as an effect of cellular signalling processes. Scientific studies since 1950s[17] have established that a multitude of optical properties including birefringence, optical path length changes (due to displacements or refractive index change), opacity and scattering are modulated during and in concurrence with

action potential propagation[23]. Extensive studies have been carried out showing changes in scattering[25] to the order of 10^{-5} to 10^{-3} [23,26,27]over a few milliseconds, depending on the sample, and changes in birefringence[28,29] of the sample to 10^{-6} to 10^{-4}. Changes in refractive index and displacement of membranes[29,30] (0.5 nm- 5 nm) are also manifested as changes in scattering. This opens possibilities for optical, label free detection, which is free from challenges like toxicity and invasiveness, and can be developed to achieve high spatial and temporal resolution with high throughput detection.

Many attempts have been made to detect action potential firing in neural networks in a non invasive, label free manner, most of them capitalizing on intrinsic optical signals to indicate a signal reflective of action potential propagation. The major challenge with this is the low signal to noise ratio. The optical changes that occur are much smaller in magnitude than the background changes, which makes them tough to detect. Some studies have managed to image membrane potentials optically like: Watanabe *et al*[31] in 1987, who measured birefringence changes in a dissected lobster leg nerve, or Schei *et al*[32,33]who measured changes in polarized light in transmission and reflectance mode in a stimulated lobster leg nerve, or Graf *et al*[34] who detected scattering intensity changes in abdominal ganglion neurons of Alypsia Californica using OCT and fluorescent dyes, with a signal averaging. Islam *et al* achieved single shot detection without using extragenous dyes although in nerve bundles, like horseshoe crab nerve bundle[35] (10-15 nerves in a bundle), using phase resolved-OCT. Other techniques have also been used that use activated surfaces, nano particles and quantum dots to achieve label free detection at the specialized surface[36-38]. Quantum effect in diamonds has also been exploited by many research groups to detect action potential[38], as has Surface Plasmon Resonance[39] and Raman Spectroscopy. Others have detected membrane potential on non neuronal cells like Oh *et al*[40,41].

Through these many attempts, there has not been much success in detecting action potential in a single shot, label free manner in single mammalian neurons. Most of them either (a) resort to signal averaging to enhance the signal[29,42], or (b) use fluorescent dyes as a contrast agent[43,44], or (c) can only measure the changes on special, functionalized surfaces[34,42,45], at certain discreet spatial positions[45] or membrane conditions[46], and (d) use nonexcitable cells[47], or neurons and nerve bundles of non-mammalian organisms[38,48] like lobster or frog leg nerves[49], sea slug ganglion neurons[50], or giant squid axons as their sample because the physical membrane changes associated with action potentials are much larger and better reflected in these sample because of their large diameters (upto 3-5 mm) compared to mammalian neurons (10 μm) and hence the optical effect of AP propagation can be detected more easily. However, in order to understand the neural communication in the appreciably more complex mammalian neural system, it is vital to study mammalian neurons which are much smaller, and hence, it is harder to detect any membrane potential changes in a label free manner, without averaging multiple signals.

In this doctoral project, I propose the use of a low coherence interferometric detection technique to optically detect action potentials in individual mammalian neurons in network in a single shot, label free manner. The method we have used here can be categorized as an Intrinsic Optical Imaging technique as it measures the nanoscale optical path length changes associated with cellular firing. It has potential use in applications requiring to gauge neural functionality in vitro, which range from drug testing, to functionality and recovery assays, migration studies, studying various disease models and neural regeneration under various conditions and cues. All these applications require a method that detects action potential with preferably subcellular resolution (to study individual regions of the cell) without disturbing the indigenous environment either

mechanically (electrodes or other invasive procedures) or chemically (with the use of exogenous dyes). This method fits these requirements, and has the sensitivity and temporal resolution to study these changes as they happen, even in mammalian neurons. It is also very uniquely suited to better understand action potential propagation itself, as it can detect any opto-mechanical processes accompanying the electrochemical signaling, which might be as pivotal and telling as the electrical signals themselves. In future, this technique can potentially be developed into a 2D highthroughput detection system by using a swept source or by using galvanometric mirrors to scan the sample, which would allow mapping of action potential propagation in a neuronal network.

Chapter 2

System description

2.1 Introduction to interferometry

The method used here is an Intrinsic Optical Imaging technique using Common Path Phase Sensitive Low Coherence Near Infrared Interferometry which is capable of measuring the nanoscale optical path length changes associated with cellular firing due to change in refractive index, or physical path length changes or both using near infrared light. Interferometry is a classic technique that has been widely used in different applications, but is especially popular in the fields of biological and material sciences since it is a non-contact, high resolution, sensitive, depth resolved imaging technique which can be used to visualize microstructures in real time. It can also be used to develop 2-D and 3-D image by scanning the sample, and such multidimensional mapping implementation of interferometry is known as Optical Coherence Tomography, which has become increasingly popular in biomedical applications, especially for ophthalmology. When compared to conventional noninvasive techniques, optical biopsy by OCT performs much better in terms of resolution as well as speed. Combined with fiber optics, and other delivery devices and techniques it has also gained popularity as a tool for minimally invasive surgeries.

2.1.1 History of Interferometry

The first instances for interferometric studies can be attributed to Grimaldi (in 1655), Newton, Hooke and Huygens, Fizeau and Foucoult as early as 1800s. Young's double slit experiment, which was done as early as 1801, also proved that light and matter can exhibit wave as well as particle properties in a definitive study of interference from two point sources of light. Fizeau was the first to propose Stellar Interferometry in 1868, and suggested a method to calculate the diameter of a source star by studying the extinction

of the fringe contrast. Michelson independently discovered and developed optical interference in 1890s, and continued up until 1920s. Intensity Interferometry was developed by Hanbury Brown and Twiss in 1956. Invention of laser, better detectors and optoelectronics in the 70s and 80s led to a more widespread interest in optical interferometry. White light interferometry or low coherence interferometry was first described by Isaac Newton. But the first biological sample to be measured was reported in 1988[51].

Interferometry is used to measure optical path length changes between the sample and reference arms as indicated by the detected intensity. There are many popular interferometric setups such as Mach-Zehnder interferometer, Michelson interferometer, Fabry Perot and Sagnac interferometer. In case of Michelson interferometer setup (which has been employed in this project), the incident light beam is divided into a reference and a sample beam and these are superimposed on each other to give an interference signal (fringes). If there is no relative change in the two paths, the fringes remain constant. Any change is encoded as a change in intensity value as detected by the sensors. By using a long coherence light source, interference patterns can be seen up to a large depth of the sample. The recent breakthrough in measuring gravitational waves (LIGO) was achieved by employing a Michelson interferometer, albeit with huge arms (some 4 km in length) and a very powerful laser, to detect extremely minute changes. When sectioning the sample into smaller regions of interest for the sake of collecting signal from a thin optical slice is required, Low Coherence Optical interferometry is the more suitable technique. Using low coherence (broadband) light source ensures coherence gating, which means that signal is collected only from a short depth from the focal point of the interrogating beam (which depends majorly on the coherence length of the beam). The coherence length also determines the axial resolution of the measurement, which is one of the many

advantages of interferometry based imaging systems in that the axial resolution is independent of beam focusing and spot size. This has the added advantage of avoiding flooding a large volume of the sample with the focused probe beam, hence mitigating phototoxicity and photobleaching issues.

2.2 Fundamentals of Optical Interferometry

Light is an electromagnetic wave consisting of oscillating electric and magnetic fields that are perpendicular to each other and to the direction of propagation. Maxwell's equations help us derive the scalar wavefunction which satisfies the equation:

$$\nabla^2\psi(r,t) = \frac{1}{c^2}.\frac{\partial^2\psi(r,t)}{\partial t^2} \quad \text{Eq. 2.1}$$

where ∇^2 is the Laplacian operator, c is speed of light, t represents time, r represents position variable.

Representing light as a complex field, in simplified form, for a wave propagating in z-direction,

$$\nabla^2\psi(r,t) = E_0.\exp\big(i(kz-\omega.t)\big) \quad \text{Eq. 2.2}$$

where E_0 is the field amplitude, k is the wave vector, ω is the angular frequency of the light. Interference is the superimposition of two waves, which is given by

$$E_{Tot} = E_1.\exp\big(i(kz-\omega.t+\varphi_1)\big) + E_2\exp\big(i(kz-\omega.t+\varphi_2)\big) \quad \text{Eq. 2.3}$$

where E_1 and E_2 are the field amplitudes and φ_1 and φ_2 are the phases of the two superimposing waves respectively.

In terms of intensity, this becomes:

$$I_{TOT} =< (E_1+E_2).(E_1+E_2)^* > \quad \text{Eq. 2.4}$$

$$I_{TOT} = |E_1|^2 + |E_2|^2 + 2|E_1||E_2|\cos(\phi_1-\phi_2) \quad \text{Eq. 2.5}$$

$$I_{TOT}(\omega) = I_1(\omega) + I_2(\omega) + 2\sqrt{I_1(\omega).I_2(\omega)}\cos(\phi_1-\phi_2) \quad \text{Eq. 2.6}$$

where I_1 and I_2 are the intensities, ϕ_1 and ϕ_2 are phases of the interfering beams respectively.

Fringe visibility contrast or modulation depth which is a measure of the quality of the interference is defined as the ratio of the difference of the maximum and minimum intensities to the sum of the maximum and minimum intensities. The maximum occurs at constructive interference when the phase difference between the two light beams is an even multiple of π (where $\cos(\phi_1 - \phi_2)$ is 1) and the minima occurs at $\cos(\phi_1 - \phi_2) = -1$, which occurs when the phase difference between the two light beams is an odd multiple of π.

So, Fringe visibility contrast is defined as:

$$V = \frac{I_{max} - I_{min}}{I_{max} + I_{min}} = \frac{2\sqrt{I_1 I_2}}{I_1 + I_2} \qquad \text{Eq. 2.7}$$

V is maximum when these interfering waves have nearly the same intensity. In case of equal intensities, V becomes 1, which is ideal in terms of fringe quality.

2.2.1 Time domain vs Frequency/spectral domain interferometry:

Interferometry can be achieved in time domain (Time domain interferometry or TDI) as well as spectral/frequency domain (Frequency domain interferometry or FDI). In TDI, interference is recorded as a function of reflector position. Information is collected at a single point at each instant, and the reference arm is swept to get depth information from the sample. A single photodetector is used, and the point of measurement is chosen by mechanically moving or sweeping the reference arm, which sweeps the reference beam to interfere with light collected from the sample at a depth of the coherence length matching the position of the reference arm. This limits the speed of measurement to the speed of the mechanical sweep and the speed/resolution of the detector (minimum time required to move to the next measurement).

Spectral Domain Interferometry on the other hand, collects data from all depths simultaneously on a photodetector array, as a function of optical wavelength. Spectral/Fourier Domain interferometry was first proposed by Fercher *et al* in 1995[52]. In the next decade, multiple groups demonstrated increased speed, SNR and sensitivity performance in Spectral Domain Interference when compared to TDI[53,54]. SDI systems benefit from significant reduction in shot noise by replacing the single element detector in TDI systems by multi-element detector arrays, and spectrally dispersing each wavelength to an element of the array, hence eliminating the cross shot noise, which is otherwise present with a white noise characteristic at all frequencies in TDI systems[55]. Because of such SNR and speed advantage over TDI, SDI has gained ground in biological imaging in the last two decades, particularly in its implementation of OCT. Volumetric scanning of sample is much more straightforward and stable, making it ideal for developing compact imaging systems.

In spectral domain interferometry, interference is recorded as a function of optical wavelength using either a Swept Source (SS) or a Broad-spectrum source. The spectrally dispersed output is detected to give depth information. Using broad spectrum source, each wavelength sees a different depth of the sample, interfering with the reference beam at different depths, corresponding to the optical path lengths as seen by the wavelength.

$$OPL_{\lambda,i} = n(\lambda)_i \, . d_i \qquad \text{Eq. 2.8}$$

where $OPL_{\lambda,i}$ =Optical Path Length for wavelength λ at an instant 'i', $n(\lambda)_i$ = refractive index for light of wavelength λ at instant 'i', d_i = physical distance at instant 'i'. This spectrally dispersed output can then be incident upon a photodetector array where the interference intensity corresponding to different depths can be viewed on individual pixels.

Naturally, the execution of low coherence interferometry in the frequency domain is more robust and faster, in general, as opposed to TDI because of fewer moving parts and the ability to get depth information without scanning the reference arm, which would limit the speed to the maximum speed of mechanical components. It also performs significantly better in terms of noise/SNR as shown by various experiments[56].

The spectral interference spectrum intensity in FDI is given by:

$$I_{SI}(\omega) = I_R(\omega) + I_S(\omega) + 2\sqrt{I_R(\omega).I_{S(\omega)}}\cos[\varphi_S(\omega) - \varphi_R(\omega) - \omega.\tau] \qquad \text{Eq. 2.9}$$

where $I_{SI}(\omega)$ is the interferometer output intensity as a function of optical frequency, $I_R(\omega)$ is the intensity spectrum of reference arm, $I_S(\omega)$ is the intensity spectrum of the sample arm, $\varphi_S(\omega)$ is the phase of the sample arm, $\varphi_R(\omega)$ is the phase of the reference arm, and τ is the fixed optical delay.

2.2.2 Common path geometry:

In this case, we are using a common path geometry, which means that there is no separate reference arm. Rather, the reference beam is provided by the sample holder surface, and follows the same path as the sample beam. By using a common path setup, we eliminate the need to have an external reference path, which diminishes noise and the need to make compensating adjustments in one arm because of a change in the other, resulting in many advantages, like- automatic compensation for polarization and dispersion effects, easier alignment, common mode noise cancellation, smaller footprint, decreased sensitivity to vibrations, and as a result, a more stable construct[57]. The low coherence beam from the sample and a reflecting surface near the sample (usually the sample holder) recombine to interfere and the output from the interferogram is resolved by the detector (Photodetector/CMOS/EMCCD camera) to give us the interference fringes, which encodes the depth resolved information from the sample.

Reflections from surfaces other than the desired sample and reference surfaces can also interfere and appear on the detected signal. Sometimes multiple signals can be present in a single interferogram, with one frequency riding on top of another frequency. The signal strength decides the prominence of each signal. By changing the focal plane and modulation depth, we can tune into different signals. Such signals between each pair of reflecting surfaces within the coherence length have an interference pattern, each with their own specific frequencies depending on the distance between these surfaces (closer the surfaces, lower the frequency). This makes it easier to filter out interference signals from surfaces other than the sample as these are encoded in a different frequency channel, and hence the information content is impervious to these changes. The distance between the reflecting surfaces also determine the signal strength and modulation depth, which will be discussed later in this chapter.

In common path mode, the spectral interference is given by:

$$S_o(k,t) = \alpha S_i(k)\{R_1 + R_2 + 2\sqrt{R_1 R_2}|\mu(k)|\, cos[4\pi p(t)k]\} \qquad \text{Eq. 2.10}$$

where, S_i is the spectral density of the broadband light source, α is the coupling efficiency of back reflected light from the reference surface to the interferometer. R_1 and R_2 are the reflectivity of the sample and reference surface, respectively. $\mu(k)$ is the spectral coherence function, and $p(t)$ is the optical path difference (OPD) between the sample and reference surface. k is the wavenumber given by $2\pi/\lambda$. Replacing p(t) by its value in terms of physical path length difference (Δx), at a given instant,

$$S_o(k) = \alpha S_i(k)\{R_1 + R_2 + 2\sqrt{R_1 R_2}|\mu(k)|\, cos[2.n.k\Delta x]\} \qquad \text{Eq. 2.11}$$

2.2.3 Phase sensitive FDI:

From this detected interferogram, we can derive information about the optical path length changes in the sample beam with respect to the reference beam. The sinusoidal component of the fringes encodes the depth/ phase information, while the first two terms

contribute to the DC signal. To get higher sensitivity, we derive this information from the phase signal at the appropriate frequency channel. A change in physical distance Δx during the time interval between two A-lines will introduce a phase change of the reflected light given by $\Delta\varphi = 2n.k_0\Delta x$ [58], where n is the refractive index of the sample and k_c is the average wavenumber of the broadband source ($k_0=2\pi/\lambda_0$).

In terms of OPL (optical path length) changes, $\Delta\varphi = 2.\ k_0.\Delta OPL$, which implies that a phase change of pi encodes an optical path length change of one wavelength ($\lambda/2$) (since it is a reflection mode measurement, the beam travels the same path difference twice). Calculating this phase difference at each time instant reveals the optical path length changes over time. By deriving information from the phase measurements instead of just the magnitude of the interference, the sensitivity of the system can be increased multifold, allowing subwavelength fluctuations to be measured. An interferogram intensity value is decided by the intensities of the interfering beams as well as the phase difference between them. While the intensities can be affected by random events like mechanical vibrations, noise and other events, anywhere in the optical path, changes in phase are only caused by a change in the optical path length between the two reflecting surfaces (which can also include a mechanical disturbance) which can be because of physical path length differences or refractive index changes. Information encoded in phase change is more immune to noise and is more sensitive to actual changes in the interferometer geometry due to change in optical path length of either arms.

To glean data from the interferogram, the interferogram (Eq. 2.11) is Fourier Transformed and gives peak values at $x = \pm 2n\Delta x$. The FT value at this peak is calculated to be

$$\tilde{I}(\pm 2n\Delta x) = (\alpha/2)S_i\Delta t\sqrt{R_1\,R_2}\,|\mu(2n\Delta x)|\exp(\pm j2nk_0\delta x) \qquad \text{Eq. 2.12}$$

where, Δx is the physical separation between the two reflecting surfaces, S_i is the total input power from the broadband light source, α is the coupling efficiency of back reflected

light from the reference surface to the interferometer. R_1 and R_2 are the reflectivity of the sample and reference surface, respectively, $\mu(2n\Delta x)$ is the spectral coherence function, k_0 is the source center wavenumber. The phase of $\tilde{I}(\pm 2n\Delta x)$ can be used to measure Δx with higher resolution. This can be done by measuring changes in phases over a time t from an initial or reference time t_0.

$$\Delta x\,(t) = \lambda_0/4n\pi[\angle\tilde{I}(\pm 2n\Delta x, t) - \angle\tilde{I}(\pm 2n\Delta x, t_0)] \qquad \text{Eq. 2.13}$$

where $\angle$ is the phase operator and λ_0 is the central wavelength of the source.

If $\Delta\varphi(t)$ be the phase change as a function of time, it brings us back to the relation $\Delta\varphi = 2n.k_0.\Delta x$. Eq. 2.13 assumes no or negligible change in refractive index. A more accurate representation of this would be in terms of Optical Path Length change, or p(t)

$p(t) = (\lambda_0/4\pi)[\angle\tilde{I}(\pm 2n\Delta x, t) - \angle\tilde{I}(\pm 2n\Delta x, t_0)] = (\lambda_0/4\pi).\Delta\varphi(t)$

From Eq. 2.10, temporal change in phase can also be calculated by the expression,

$$\Delta\varphi(t) = (4\pi/\lambda_0)\; p(z,t)|_{z=d} = \tan^{-1}\left\{\frac{Im\, S_0(z)}{Re\, S_0(z)}\right\} \qquad \text{Eq. 2.14}$$

where, $S_o(z)$ is the Fourier transform of Eq. 2.10 calculated at the peak value of the coherence function corresponding to spatial location $z = d$, which is equivalent to the gap of the cell culture device, $p(z,t)|_{z=d}$ is the optical path length difference.

2.2.3 Characteristics of Low Coherence Interferometry system:

The lateral resolution (δ_X) of the low coherence interferometry system is interpreted as[59] the point spread function of the system at the position of the focal plane. The axial resolution (δ_Z) is the same as the coherence length (l_C) of the source. These values are given by:

$$\delta_X = 0.37\,\frac{\lambda_0}{NA} \qquad \text{Eq. 2.15}$$

$$\delta_Z = l_C = 2\ln(2)\,\frac{{\lambda_0}^2}{\pi.\Delta\lambda} \qquad \text{Eq. 2.16}$$

The depth range is inversely proportional to the spectral resolution (δ_Z) and is given by

$$z = \frac{{\lambda_0}^2}{4n\delta\lambda} \quad \text{Eq. 2.17}$$

2.2.3.1 Signal and noise characteristics:

Further characterization for getting the SNR of the system requires characterization of the noise and signal in the system. These quantities depend on the interference signal itself, as well as the detector used. The detector detects the signal and noise, converts optical power to electrical output which is taken as a readout. For convenience, the signal and noise terms are often expressed in terms of charge squared (e^2).

The signal detected in SD- LCI is given as:

$$S_{SD} = \frac{\eta^2.e^2 P_{ref} P_{sample} {\tau_i}^2}{{E_v}^2}[e^2] \quad \text{Eq. 2.18}$$

with e being the electron charge, P_{ref}, and P_{sample}, respectively, the reference arm and sample arm power per detector element at the detection arm fiber tip, τ_i the integration time, and E_v the photon energy[60].

The read out and dark noise, shot noise and relative intensity noise (RIN) contributions to the overall noise in electrons squared per detector element are characterized as follows:

$${\sigma^2}_{noise} = {\sigma^2}_{r+d} + \frac{\eta e^2 P_{ref} \tau_i}{E_v} + \left(\frac{\eta e P_{ref}}{E_v}\right)^2 \tau_i \tau_{coh}[e^2] \quad \text{Eq. 2.19}$$

where ${\sigma^2}_{r+d}$ is the sum of read-out noise and dark noise, $\tau_{coh} = \sqrt{2ln2/\pi}{\lambda_0}^2/c\delta\lambda$ the coherence time[61]. The assumption here is that the sample arm power is much lower than the reference arm power[62].

The condition for optimal SNR is when shot noise dominates both read out noise and Relative Intensity Noise. The condition for shot noise to dominate Read Out Noise is $\frac{\eta e^2 P_{ref} \tau_i}{{\sigma^2}_{r+d}.E_v} > 1$ and for it to dominate Relative Intensity Noise is $\frac{E_v}{\eta P_{ref} \tau_{coh}} > 1$.

Under shot noise limited conditions, the SNR in spectral domain system is given by:

$$SNR_{SD} = \frac{\eta P_{sample} \tau_i}{E_v} \quad \text{Eq. 2.20}$$

where η is the spectrometer efficiency, P_{sample} is the sample arm power, τ_i is the detector integration time, and E_v is the photon energy.

Shot noise is an electronic noise and depends on the A/D resolution (which corresponds to the number of electrons required for an incremental increase of 1 pixel intensity value of the detector), originating from the discrete nature of electric charge and is associated with the particle nature of light. It is determined with the illumination of only the reference arm and calculating variance at each pixel of the camera with a high 'n' number. It can be expressed in terms of electrons as, $\sqrt{I_{PV}(\lambda)/\Delta e}$ where $I_{PV}(\lambda)$ is the pixel value corresponding to the intensity at each photodetector array element, with values ranging from 0 to 2048 (12-bits) and Δe is the A/D conversion resolution. The variance as measured in pixel values is defined as:

$$\sigma^2(\lambda) = \frac{I_{PV}(\lambda)}{\Delta e} + \sigma^2{}_{r+d} \qquad \text{Eq. 2.21}$$

Here, the first term is the shot noise contribution and the second term corresponds to the read-out noise.

The interferometry system being used is not shot noise limited, but rather sits much higher than the shot noise floor. While care has been taken to reduce as much noise as practically possible, by making the setup mechanically stable, providing insulation from ground vibrations by placing it on a floated optical table, keeping the optical fibers relatively fixed, fixing the sample housing in the sample holder with clamps, there is still a lot of noise, even from the sample itself, which has a lot of motion. Most of the other responsible factors and parameters are determined by the components used and cannot be improved beyond a certain point, or have been optimized for the system performance keeping in mind the various tradeoffs (like speed and noise).

In best case scenario, assuming a shot noise limited performance, the shot noise is given by:

$$A(z) = \left(\frac{\rho}{e} S\Delta t R_R\right)^{\frac{1}{2}} \exp(-j\varphi_{rand}) \quad \text{Eq. 2.22}$$

where A(z) is the shot noise, given by an additive, uncorrelated Gaussian white-noise term, with a random phase given by φ_{rand}. Phase error is maximum when the signal and noise terms are orthogonal to each other, which is achieved when $\varphi_{rand} = 2k_0 n\delta z \pm \pi/2$. In this case, the sensitivity becomes:

$$\delta z_{sens} = \frac{\lambda_0}{4n\pi} arctan\left[\frac{A(z)}{I_i(z)}\right]$$

$$\approx \frac{\lambda_0}{4n\pi}\left[\frac{2e}{\rho S\Delta t R_s}\right] \quad \text{Eq. 2.22}$$

Hence, to improve sensitivity, we need to either (a) increase the source power, or (b) increase the integration/exposure time, or (c) increase the Reflectivity of the sample surface. Of these parameters, (a) and (b) cannot be changed much as the available power is fixed by the source being used, and the maximum output is being used; and increasing integration time will reduce the speed of acquisition which is an important feature of the detection system, considering that the timescale of the process being detected is in milliseconds. So, to get a better sensitivity, efforts have been made to increase R_s. It has been almost tripled from the original value of 0.11% to 0.3% by changing the housing system, as is discussed in greater details in section 2.3.

2.2.3.2 Sensitivity drop off as a function of depth:

In spectral domain low coherence interferometry, the reflectivity in z -space is given by the square of the Fourier component in k-space. The magnitude of the Fourier component is proportional to the magnitude of the modulation depth of the spectrum, multiplied by the number of illuminated pixels of the camera, which helps achieve a high dynamic range in z-space (exceeding 40–60 dB) with a relatively small modulation depth. In case of reflections between multiple surfaces, each such pair produces a periodic modulation of a frequency that depends on the distance between these surfaces. These

modulations are summed and are present as modulations riding atop each other on the DC component.

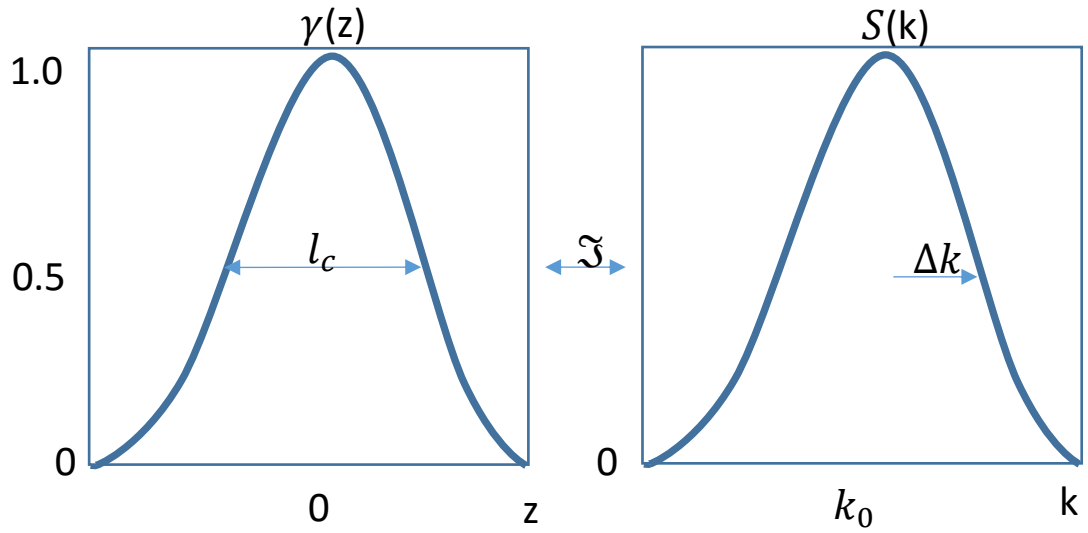

Figure 2.1: Illustration of Fourier transform relationship between the Gaussian-shaped coherence function γ(z) (characterized by the coherence length l_c), and the light source spectrum S(k) (characterized by the central wavenumber k_0 and wavenumber bandwidth Δk).

The spectrometer resolution is finite and hence introduces a sensitivity decay across the measurement range. This sensitivity reduction is given as the convolution of the finite pixel size with the Gaussian spectral resolution, as a function of imaging depth (z).
This is expressed as:

$$R(Z) = \frac{\sin^2(\frac{\pi z}{2d})}{\left(\frac{\pi z}{2d}\right)^2} exp\left[\frac{\pi^2\omega^2}{8ln2}\left(\frac{z}{d}\right)^2\right]$$

where d is maximum scan depth and ω is the ratio of spectral resolution to the sampling interval.

So, the greater the separation or path difference between the sample and reference arms, the lower is the sensitivity of the interferometer, and weaker the signal. This can be visualized as moving away from the center of the Gaussian beam (as shown in Fig. 2.1) in the x-axis, resulting in a drop-off of sensitivity (represented by the y-axis). This implies that for better sensitivity, the distance between the sample and reference surfaces should be minimized as far as practical application and other constraints allow. This is another reason to choose the sample housing system that has been chosen, as the separation is reduced as compared to conventional systems.

2.2.3.2 Remapping to k-space:

The spectrometer spectrally disperses the interferogram, and maps the interference to the camera/photodetector array pixels based on the wavelength. The optical spectrum is then Fourier transformed to relate the physical distance to the wave number k. Since k varies inversely with the wavelength ($k = 2\pi/\lambda$), the spectra are not evenly spaced in k-space. So, an accurate mapping needs to be performed to obtain a proper depth profile. Incorrect wavelength mapping generates a depth-dependent broadening of the coherence peak.

This can be done by a number of methods like- imposing a known modulation on to the spectrum which can be used for calibration. Some auto calibration techniques have also been suggested which might be better for the system as a whole to compensate for any thermal or mechanical drift occurring between the measurements. These techniques reiterate the mappings till a perfect sinusoidal modulation is achieved from the initial wavelength array (W) calculated from grating equation. Corrections are made iteratively to W and W is used to interpolate the spectral interference fringes to evenly spaced k values, with zeroes padded to improve the interpolation quality. The phase nonlinearity wavelength assignment is iteratively determined and reduced. A third order polynomial is

fitted on the phase of this interpolated k-space spectrum. Assuming that the nonlinearity stems from mismatched wavelength assignments, the nonlinear part ($\sigma(k)$) of the fit is used to make corrections to W. A new k- array k' is calculated from the initial $k = 2\pi/W$ array and ($\sigma(k)$), using the equation $k' = k + \sigma(k)/z_{peak}$, where $z_{peak} = 2\pi Peakindex/$ (k_{max}-$k_{\min}$), where Peakindex refers to the location of the coherence peak. This is iteratively applied till $W' = 2\pi/k'$ is achieved that is a wavelength array corresponding to the linear phase as a function of evenly spaced k'.

Another technique is to use a known spectrometer to characterize a spectrum, and use the feature points to map the spectrum on the spectrometer being calibrated. By using more such feature points, the mapping can be done more accurately, but ideally, at least five points are required. This gives equations to solve for the relationship between pixel position and wavelength. For example, the reference spectrum from the source is recorded by Oceanoptics USB 4000, a commercially available spectrometer as well as by the custom designed spectrometer (Fig. 2.2). Some of the feature points could be the peaks the valley, and the half power points. It should also be noted that the spectrum is flipped in k-space (as seen in the recording by the custom built spectrometer)

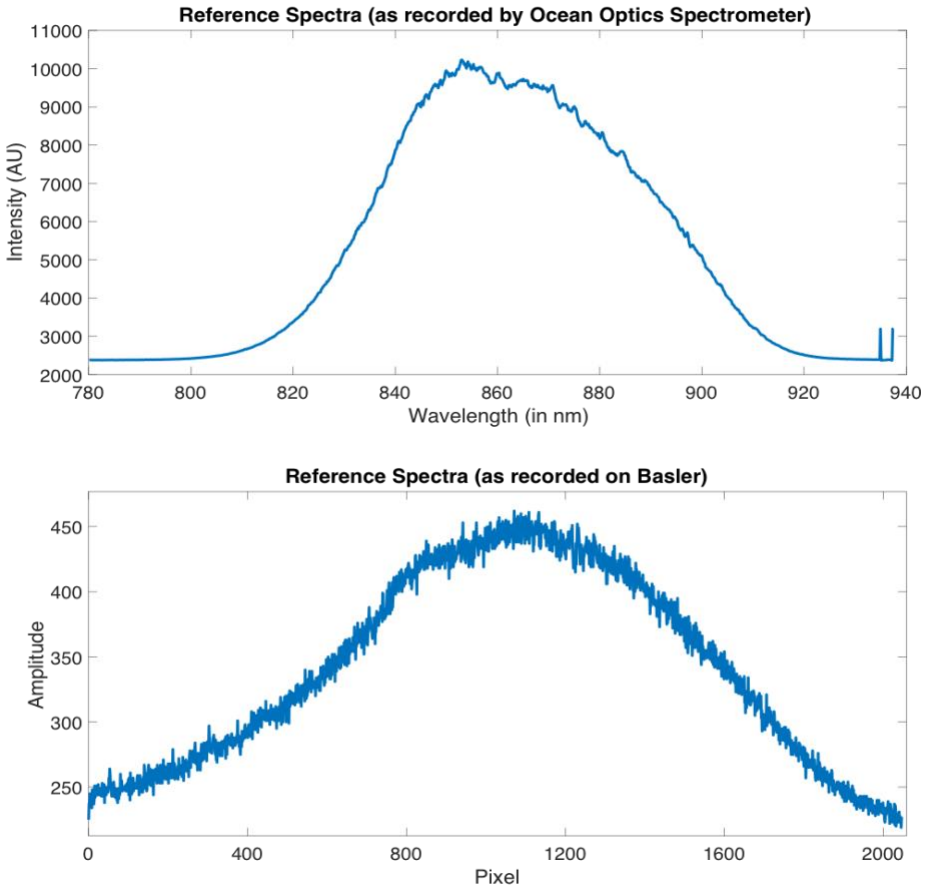

Figure 2.2: (top) Intensity spectrum of SLD source as captured by a known spectrometer (Oceanoptics USB 4000) and (bottom) as recorded in the photodetector array as a function of pixels. As it can be noticed by comparing the top and bottom figures, the spectrum is flipped in the x axis. The peaks and the middle valley, as well as the half power points can be used as the feature points for remapping to k-space.

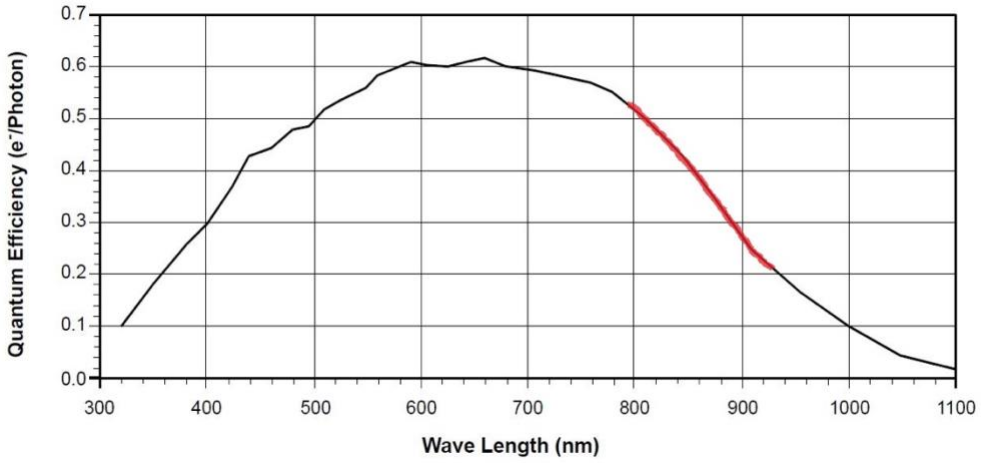

Figure 2.3: Basler camera response. The portion in red corresponds to the wavelength range of the source.

There might also be a need to correct for the photodetector array spectral response. Since the photodetector sensitivity might not be linear over the entire range of wavelength, some corrections might be needed to ensure a uniform response to intensity. The spectral response is achieved in terms of the wavelength, and an inverse is multiplied to the output of the photodetector array to normalize the detector sensitivity across the operating wavelength range.

2.3 Phase Sensitive Spectral Domain Low Coherence Interferometry system setup

The Phase Sensitive Spectral Domain Low Coherence Interferometry (PS SD-LCI) setup is implemented by using a broadband SLD source. Since the application of this technique is in biological specimen imaging, the choice of the probing beam is dependent on various factors like optimal depth penetration, low scattering, low absorption while maintaining the health of the sample, i.e., avoiding phototoxicity or overheating. Keeping these factors in mind, the probing beam has been chosen to be in the biological optical

window which is from 650nm-1350 nm where the lowest absorption in water and blood is observed around 790-900 nm. This also overlaps with the wavelength range where the Quantum Efficiency of commonly used photodetectors (Si based) is the highest. This determined the desired spectrum of the light source to be around 840-860 nm. The source chosen in a Super-Luminescent Diode (SLD) with a spectrum from 830-920 nm, with a FWHM of 63 nm, and peak at 860 nm. The source is a very important aspect of the system as the source spectrum determines the axial field of view, axial resolution and the lateral resolution.

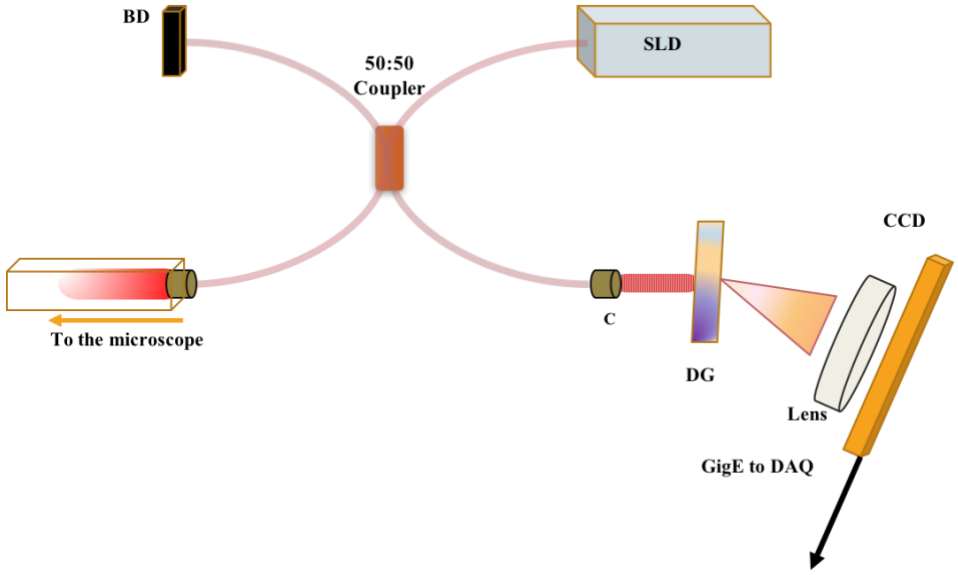

Figure 2.4: Spectrometer setup: BD- Beam Dumper, 50:50 Coupler, SLD- Superluminescent Diode, FC- Fiber Coupler, DG- Diffraction Grating, CCD- Charge Coupled Device.

The interferometer is implemented with optic fibers, using fiber couplers to divide the light in a 50:50 ratio from the broadband source. One input arm is connected to the source and the other connects to the spectrometer. Of the two sample/output arms, one is blocked, as this is a common path implementation of low coherence interferometry.

The other sample arm is attached to a modular opto-mechanical unit which consists of 30 mm cage system with a fiber connector (FC/APC) and a collimator mounted on a two axis (tip/tilt) kinematic mirror mount on one end and a C-mount on the other end that is attached to the microscope side port. Light exiting the single mode fiber is expanded, collimated, and relayed to the microscope objective (10X, 0.25 NA) of the inverted microscope (Zeiss Axio Observer). The 80/20 beam splitter inside the microscope side port allows for simultaneous sample visualization and interferometry. Reflected light from the sample is collected by the microscope objective and coupled back to the fiber port. Light incident on the sample is partially reflected from the two reflecting surfaces, which creates an interference. This spectral interference is then coupled to the same arm of the fiber coupler that delivers light to the microscope objective and feeds it into the spectrometer.

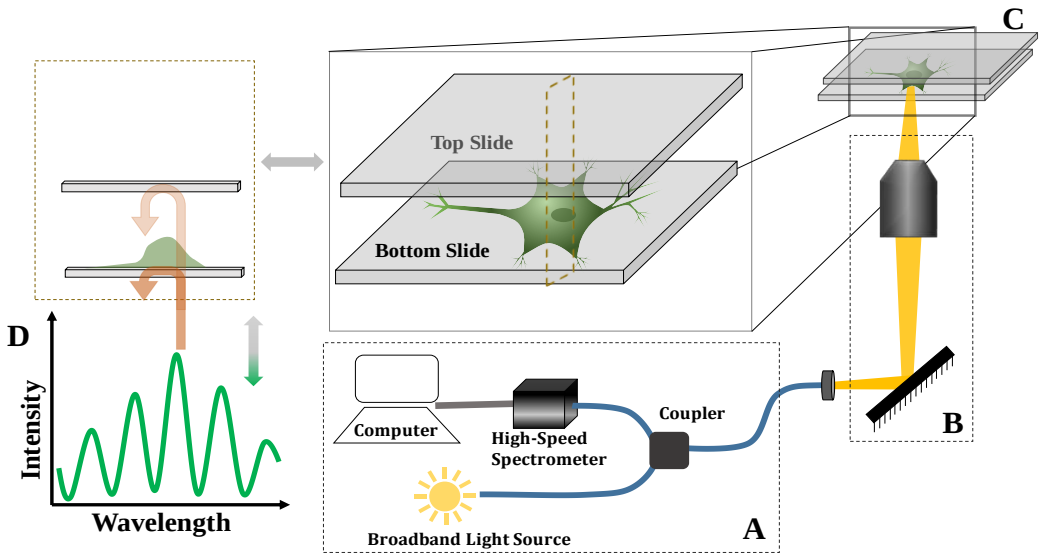

Figure 2.5: Schematic diagram of the interferometric instrument which consists of a (A) broadband SLD source, fiber coupler, high-speed spectrometer and computer for data acquisition. (B) Output port of the fiber coupler is attached to the side port of an inverted

microscope that transmits and focusses light on the soma of a neuron (C) Illustration of neuronal cell culture device in a sandwich configuration consisting of two glass slides that are separated by a fixed gap (~80 μm) with neurons attached to the bottom glass slide, and (D) Light reflecting from the bottom (glass-cell) and top (cell-media) interfaces of the two glass slides of the neuronal cell culture device couple back into the interferometer and mix to form spectral interference fringe signal.

The spectrometer consists of a fiber collimator that collimates the beam exiting from the fiber, a diffraction grating (Wasatch Photonics, 1800 lines per mm) that spectrally disperses the light, and a lens that collects and focuses the dispersed light on to the camera. The camera used here is a Basler Racer (2048 gm) GigE line scan camera, which houses a single array of 7 μm photodetectors. The camera is connected to the computer with Ethernet cable for data transfer to the DAQ card (NI PCIe-8231) and software interface (LabView) was used for data collection. Further, there is an option to trigger the acquisition by a hardware trigger line, which is driven by the Digitizer (Axon Clamp Digitizer).

The entire setup is constructed on a floated/isolated optical table to isolate it from environmental noise and vibrations which can give spurious artifacts.

2.3.1 Choosing sample housing

For biological in vitro studies the most commonly used sample housing are petri dishes, made of either plastic or with a glass bottom for better imaging. For the sake of getting a better reflection from the surface and fewer thermal effects we chose to go with glass as the sample seeding surface.

The commercially available glass bottom dishes appeared to give artifacts with laser light, with a prominent change in optical path length on illumination with the stimulation

laser. To ensure that no such optical artifacts are produced that contaminate the results and to find alternatives for the sample housing, we decided to investigate the artifact further. We discovered that most commonly available glass bottom petridish, even from different manufacturers, gave this artifact, while the coverslips available for slide preparation did not appear to suffer from this artifact. It appears that the glass used for glass bottom petridishes are sourced from the same manufacturer (Schott glass) and are made of Borosilicate glass. The coverslips, however, are made of Soda lime glass, which might constitutionally differ from Borosilicate glass in a way that does not allow noticeable change in OPL on light illumination. Characterization of this artifact confirmed expected behavior, with the change in optical path length increasing with the increase in the power of the laser, as well as with exposure time, and with no such change being observed in soda lime glass. This characterization is summarized in the Fig 2.6.

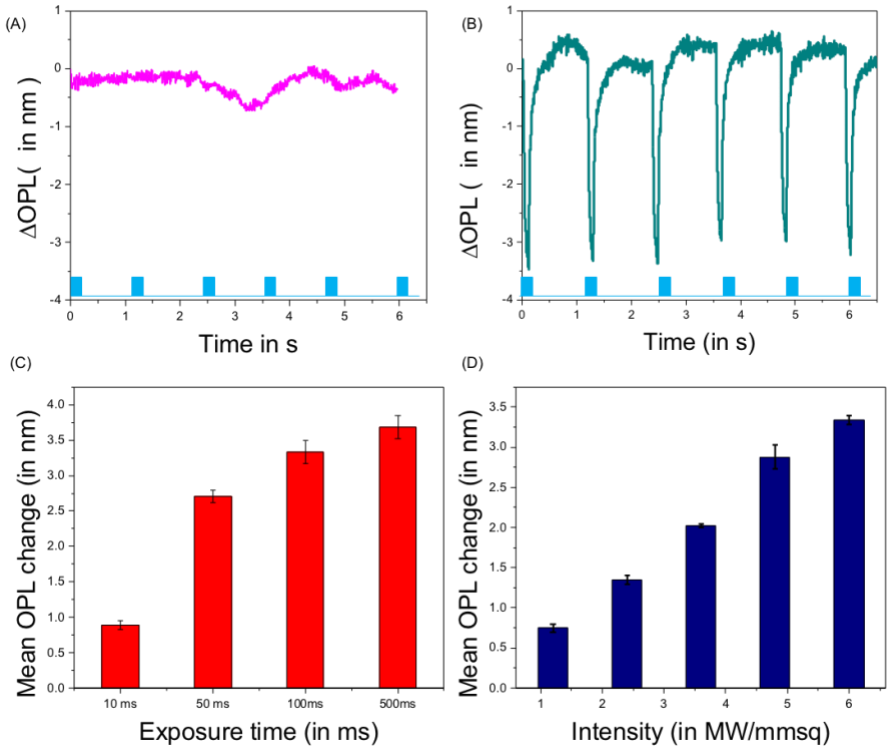

Figure 2.6: Characterization of artifact from borosilicate glass. (A) Change in OPL in soda lime glass on stimulation by laser (represented by bars in blue). (B) Change in OPL in Borosilicate glass on stimulation by laser (represented by bars in blue). The OPL drastically changes on laser impingement. (C) and (D) show the increase of OPL change in the borosilicate class on increasing the exposure time and the intensity of the laser respectively.

To avoid these artifacts, we decided not to use the commercially available glass bottom petridish and instead, design custom made cell housing device with soda lime glass coverslips.

The first design was a no1 thickness coverslip with a PDMS reservoir plasma glued on the surface. The interference signal is achieved from the backscattered light from the

top and bottom surfaces of the coverslip. The reflection from the bottom of the coverslip acts as the reference signal and the reflection from the top surface (glass-cell/cell culture media) acts as the sample signal. Changes in the cell are encoded in this beam and reflections from other portions of the cell are merged into this beam as well since they can't be distinctly resolved. The physical distance between these two surfaces is equal to the thickness of the coverslip (d_{cs}, as shown in figure below), which is around 160 μm for No.1 coverslip which is the most commonly used in our experiments.

It also needs mentioning that the interference signal would have higher SNR if thinner coverslips are used so that the signal is stronger (as it sits closer to the center of coherence function, where the correlation of the signals is higher). No.0 coverslips, with a thickness of 85-130 μm, are better in terms of signal but are too delicate to be handled or used for construction of these cell culture devices. Also, while viable for cell culture and free from artifacts, signal modulation in this arrangement is low because of mismatch in reflectivities of the two reflecting surfaces.

Calculating the reflectivity of the interfaces for sample and reference beams (refer to Fig 2.7):

$$\sqrt{R_R} = \frac{n_g - n_a}{n_g + n_a}$$

$$\sqrt{R_S} = \frac{n_g - n_c}{n_g + n_c}$$

Using values of refractive indices for these substrates as used in literature (n_g= 1.5, $n_a = 1, n_w = 1.33, n_c = 1.4$)[63], the values were calculated to be $R_R = 4\%$ and $R_S = 0.11\%$. For good visibility (V), nearly equal intensities of both beams is essential. Because of this large difference in reflectivity of two surfaces, the beams are not of equal intensities, with the reference beam being much more intense than the sample beam.

Better signal could be achieved by making the reflectivity of the two surfaces nearly equal, and reducing the distance between them to ensure higher intensity, and hence, higher SNR.

This can be achieved by designing another construct that uses 1 mm microscope slides glued together with a gap in between to culture cells. This gap can be increased or reduced by controlling the thickness of the layer of glue applied. In most cases, this thickness was around 80 μm, which is about half the thickness of a no.1 coverslip.

Calculating the reflectivity of the interfaces for sample and reference beams for slide sandwich construct (refer to Fig. 2.7):

$$\sqrt{R_R} = \frac{n_g - n_c}{n_g + n_c}$$

$$\sqrt{R_S} = \frac{n_g - n_w}{n_g + n_w}$$

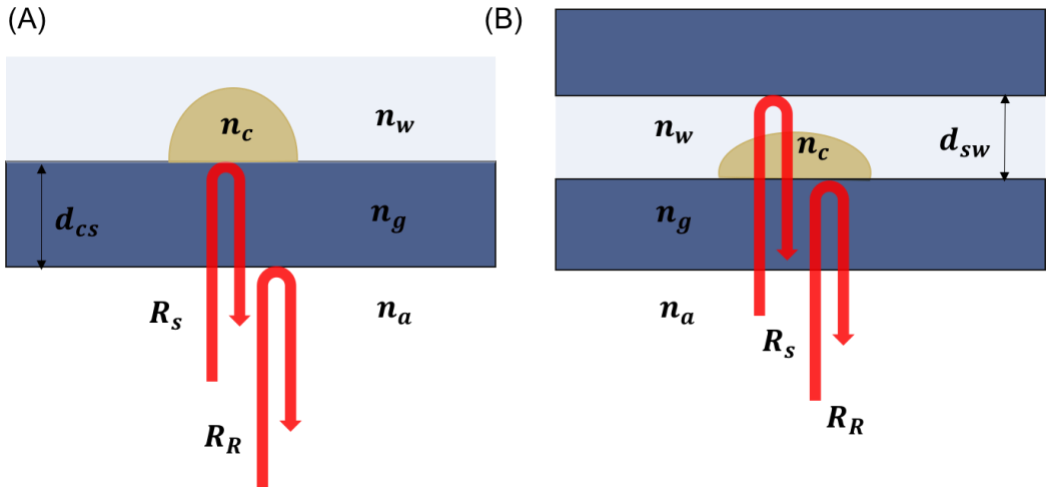

Figure 2.7: Schematic showing reflection of beam from various surfaces in (A) coverslip and (B) sandwich arrangements. n_c, n_w, n_g, n_a are the refractive indices of cell, water, glass and air respectively. d_{cs} and d_{sw} are thickness between reflective surfaces of

coverslip and sandwich. R_R and R_S are reflectivity encountered by reference and sample beams respectively.

Using values of refractive indices for these substrates as used in literature (n_g= 1.5, n_w = 1.33, n_c = 1.4)[63], the values were calculated to be $R_R = 0.11\%$ and $R_S = 0.3\%$. The values of reflectivity for reference and sample beams are much closer, leading to better visibility (V). Also, the reference beam passes twice through the entire cell (sample) and hence carries more information about changes occurring in the sample, making the measurement more sensitive and increasing the SNR.

2.3.1.1 Fabrication of neuronal cell culture device

Shown in Fig 2.8 is the stepwise fabrication process of neuronal cell culture device. Two regular grade laboratory glass slides (25×75×1 mm) were used to make each sandwich neuronal cell culture device. First, two holes with ~50 mm separation were drilled (~2 mm diameter) in one glass slide (top slide) using a diamond drill-bit. The surface was submerged in a thin layer of water while drilling to dissipate heat in order to prevent glass breakage. Next, glass slides were thoroughly cleaned using isopropyl alcohol and distilled water. On the top slide, two media reservoirs made from Polydimethylsiloxane (PDMS) were attached and bonded on top of each hole using plasma treatment. Nontoxic silicone glue was applied on the surface edges of the bottom glass slide, and the top slide was placed on it to fluidically seal the sandwich culture device. The layer of glue in between the glass surfaces generates a gap of approximately 80 microns. The devices were coated with poly D-lysine before culturing the neurons. Neurons were seeded through the PDMS reservoir and the culture media was changed every 24-48 hours to maintain healthy growth of neurons.

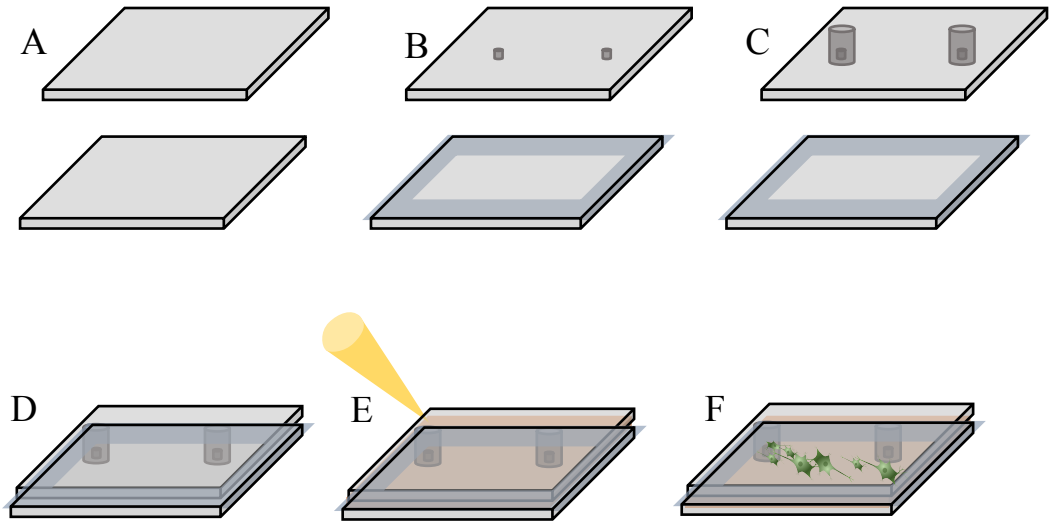

Figure 2.8: (A) Two slides are cleaned, sanitized and dried. (B) Two holes are drilled on to the top slide, and a thin layer of nontoxic silicon glue is applied on the top layer of the bottom slide. (C) PDMS reservoirs are centered and plasma glued on to the top slide, centered around each hole. (D) The two slides are then pressed together and allowed to dry in a sterile environment for 24-48 hours. (E) Neurons are seeded into one of the PDMS reservoirs. (F) The cell culture device is incubated at 37 ℃ for 7-14 days in an incubator with appropriate amount of humidity and CO_2.

2.4 Data analysis

A data acquisition card (NI PCIe-8231) and software interface (LabView) was used for data collection. Spectral interferograms are digitized and stored as binary files for post-processing. Each spectral interferogram after *k*-space conversion is Fourier transformed and phase at a spatial frequency channel corresponding to cell culture device gap is calculated as a function of time. Temporal phase difference (at a given time was calculated by subtracting the measured phase of A-Scan at time t_n from the first

(baseline) A-Scan at the start of the experiment. Change in OPD is calculated from the phase difference by using equation (Eq. 2.14).

$$\Delta p(d, t_n) = \frac{\lambda_0}{4\pi} \Delta\varphi(d, t_n) = \frac{\lambda_0}{4\pi} [\Delta\varphi(d, t_n) - \Delta\varphi(d, t_0)\,]$$

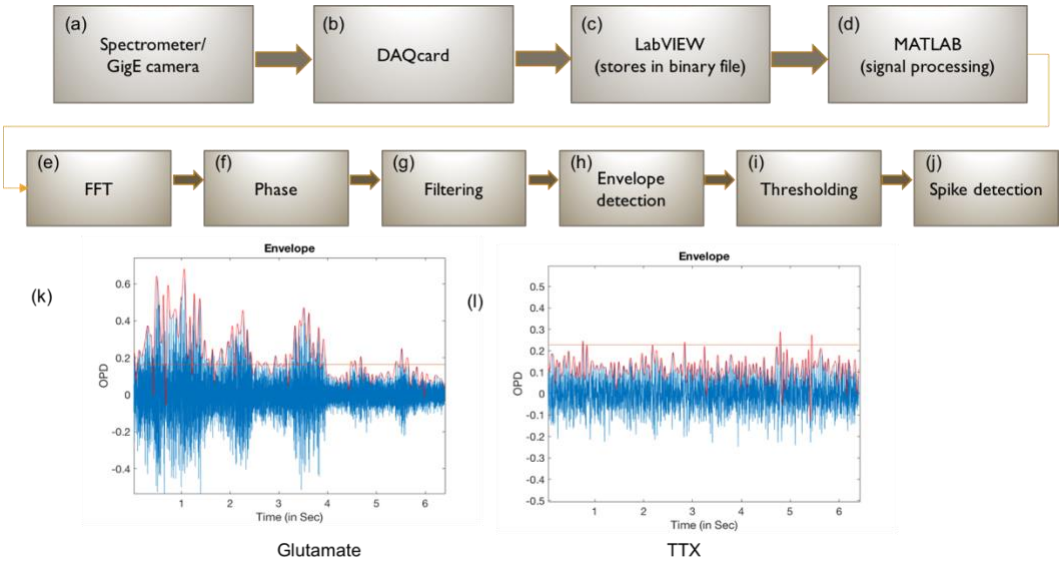

Figure 2.9: Data collection and signal processing flowchart. (a)-(i) individual sequential steps involved in collection and processing of the optical signal from the sample. (k) An example of typical optical signal in presence of Glutamate stimulation with the thresholding and envelope detection. (l) An example of typical optical signal in presence of TTX inhibition with the thresholding and envelope detection.

For counting and characterizing individual optical pulses, envelope detection (rectification and filtering) and thresholding was done on the measured change in OPD to determine pulse width, peak amplitude, and firing rate. Change in OPD was baselined, filtered and threshold was set above the baseline noise prior to the envelope detection. Second order bandpass Butterworth filter with low pass and high pass cut-off frequencies

of 200-300 Hz and 20-30 Hz, respectively, depending on the spectrum acquisition rate (A-Scan), were used to filter the rectified signal. Data was collected in 60 s segments and only segments that contained optical pulses were considered for feature extraction analysis. Continuous wavelet analysis (Morlet wavelet) was carried out in MATLAB software using 45 ms time windows for time-frequency analysis of optical pulses. the data is collected in 60 s segments in order to keep the file size from getting too large. Because of the high acquisition speed, even a 1 minute segment of collected data can approach 1 GB in size. To be able to record for longer period of time without using up too much memory, we record 1 min segments every alternate minute or so. This is purely specific to the computer and constrained by the availability of memory space in this case- the system retains the ability to continuously collect data if required.

Chapter 3

Label free optical detection of cellular activity in mammalian neurons

Phase sensitive NIR low coherence interferometry is used to detect cellular activity in mammalian neurons. This is done by measuring optical path length changes occuring in conjunction with action potential propagation. Rat cortical neurons are chosen as the sample because of the strong literature support available. Rat cortical neurons have been studied widely for a range of applications, including drug studies, neuronal injury and recovery states, and have been studied under a variety of scientific methods to investigate in-vitro neural processes. These neurons can also be genetically modified to introduce mutations and have also been used in optogenetic studies, which provides a steady resource base and literature.

The neurons are cultured as described in the section below in the sandwich cell culture. Chemical stimulation is used to excite firing in the neuronal network. Neuronal networks are known to communicate even without any external stimulation, so a neural inhibitor is used to temporarily reduce the firing, without changing any other morphological conditions. By subjecting the sample to these conditions that only alter the neuronal firing, we can ensure that the differences observed in the optical signals are caused by the presence or absence of action potential firings. Much of this work has been discussed in the published jounal article by Batabyal *et al*[64] and has been reprinted with permission.

3.1 Methods and materials:

3.1.1 Cortical neuron culture

All experimental procedures were conducted according to UT Arlington Institutional Animal Care and Use Committee approved protocol. Cortical neurons were isolated from 18-day rat embryos after cortical tissues were dissected, cleaned (meningeal layer), enzymatically dissociated (0.125% trypsin in L-15 medium) for 20 minutes at 37 ^{0}C. Dissociated cortical neurons (40,000/device) were seeded on Poly-D-lysine (PDL, 0.01%, Sigma) pre-coated neuronal cell culture devices. Each device was made by gluing two sterile, glass slides using silicone glue, as described in the previous chapter. The culture media (Neurobasal medium supplemented B-27 with BDNF and NT-3, 10 ng/ml) in these devices was changed every 24 hours. For patch clamp experiments, neurons were grown in 35 mm glass bottom petri dishes, coated with Poly-D-Lysine and the culture media was changed every 3 days. Glutamate used for chemical stimulation was obtained from Sigma Chemical and TTX for inhibition was from Tocris Bioscience.

3.1.2 Immunostaining of fixed cortical neuron

Cultured neurons were fixed with 4% paraformaldehyde in phosphate-buffered saline (PBS). Fixed cells were immunostained by standard procedure. Cells were briefly treated with blocking solution that contained 4% goat serum in washing solution (0.5% Triton in PBS solution) for 1 hour. Mouse anti-β III tubulin monoclonal (mIgG2b, 1:1000; Sigma) primary antibodies were diluted in blocking solution and precooled at 4^{o}C before use. Secondary antibodies Goat anti-mouse IgG2b Alexa Fluor® 488 (Green, 1:250; Jackson Immuno Research) were prepared in the washing solution. After blocking, the cells were incubated overnight with primary antibodies at 4^{o}C. Next day, cells were washed three times with washing solution followed by incubation with secondary antibody for 1 hour at room temperature and protected from light. Post antibody incubation, cells

were washed and stored in PBS solution. Stained cells were imaged using a fluorescence microscope.

3.1.3 Patch-clamp recording

The patch-clamp set up for computer controlled voltage and current clamp consisted of a recording system, and a digitizer and amplifier (Multiclamp 700B, and Digidata 1440, Molecular Devices). Borosilicate micropipettes of resistance from 3 to 5 MΩ were used for whole-cell patch-clamp. The micropipette was filled with electrolyte solution containing (in mM) 130 K-Gluoconate, 7 KCl, 2 NaCl, 1 $MgCl_2$, 0.4 EGTA, 10 HEPES, 2 ATP-Mg, 0.3 GTP-Tris, and 20 sucrose. The micropipette was mounted on a three-axis motorized micromanipulator (Sutter Instruments). The standard extracellular solution contained (in mM): 150 NaCl, 10 Glucose, 5 KCl, 2 $CaCl_2$, 1 $MgCl_2$ was buffered with 10 mM HEPES (pH 7.3). The neuronal electrical signals were digitized and recorded using the Molecular Devices set up. The pClamp10 software was used for data analysis.

3.1.4 Optical setup

Optical setup used for the detection of action potential in a network of cultured cortical neurons consists of the fiber interferometer, high speed spectrometer and an inverted microscope setup described in the earlier chapter (Fig 2.5). Broadband low coherence light from a super-luminescent diode (SLD) is coupled to the input port of the fiber coupler. Light exiting the fiber coupler propagates to the sample (Fig. 2.5 (B)) and is partially back reflected from the two reference surfaces of the sandwich neuronal cell culture device. In this common path geometry, components of back reflected light propagate along the same path except at the sample, generating a highly phase stable spectral interference signal (Fig. 2.5 (D)). Choosing two interfaces (bottom glass slide-neuron interface and top glass slide- media interface, zoomed inset of Fig. 2.5 (C)) of the neuronal cell culture device provides stable reference surfaces between which any

change in optical path difference (OPD) can be measured with ultra-high sensitivity. Spectral interference signal generated from light reflecting bottom (glass-cell interface) and top (media-glass interface) of the culture device can be written as expressed in Eq. 2.10,

$$S_o(k,t) = \alpha S_i(k)\{R_1 + R_2 + 2\sqrt{R_1 R_2}\,|\mu(k)|\,cos[4\pi p(t)k]\} \quad \text{Eq. 3.1}$$

where, S_i is the spectral density of the broadband light source, α is the coupling efficiency of back reflected light from the neuronal cell culture device to the interferometer. R_1 and R_2 are the reflectivity of the bottom and top interfaces of the cell culture device, respectively. $\mu(k)$ is the spectral coherence function, and $p(t)$ is the optical path difference (OPD) between top and bottom interfaces of the cell culture device. Temporal change in OPD is calculated by the expression,

$$p(t)|_{z=d} = \tan^{-1}\left\{\frac{Im\,S_0(z)}{Re\,S_0(z)}\right\} \quad \text{Eq. 3.2}$$

where, $S_o(z)$ is the Fourier transform of Eq.2.10 calculated at the peak value of the coherence function corresponding to spatial location $z = d$, which is equivalent to the gap of the cell culture device. The spectrometer acquires spectra at a frame rate of 6000 fps with a spectral resolution of 0.05 nm. Spectral fringe modulation frequency is proportional to OPD, which is the gap between the two glass (top and bottom) surfaces. Since the physical gap of the neuronal cell culture device remains constant barring any fast thermal and/or mechanical drift in the device or the spectrometer, transient physical changes in the cells will modulate the OPD. Shift in spectral phase which is proportional to the change in OPD can be quantified by calculating the change in phase (Eq. 3.2) of the spectral fringe signal in cultured neuronal system under different stimulation conditions. Although partially reflected light from other interfaces (top and bottom air-glass interfaces) mix to generate additional interference terms, they are encoded in a different spatial frequency channel and hence do not contribute to OPD in Eq. 3.2.

3.2 Results

Rat cortical neurons were maintained under standard neuronal culture for a period of 14-17 days, over which time they formed an interconnected network of synaptic connection capable of generating self-sustained spontaneous electrical activity. This neural activity can be modulated to be more or less frequent by the use of stimulating or inhibiting cues, like optical, electrical, or chemical. In this case, we have used chemical stimulant (Glutamate) to increase the neural activity, and a chemical inhibitor (TTX) to inhibit, or minimize the neural activity[65] to distinguish between the optical signals collected under three different stimulation conditions (i. no stimulation-only spontaneous firing, ii. Glutamate stimulation, increased firing, and iii. TTX inhibition, reduced firing). To detect action potential with the interferometric setup, a neuronal cell culture device containing cultured network of cortical neurons (Fig. 3.1 (A)) was firmly mounted on the inverted microscope stage using a custom stage insert, followed by adjustment of microscope objective (10X, N.A = 0.25) focal position to obtain maximum interference fringe signal modulation depth for optimal SNR. Recording experiments were started by first measuring baseline interference signal from a blank region (without any neurons or axons) of the device (Fig. 3.1 (B)) to establish the OPD noise floor. To collect the optical signal from an individual neuron, probe beam was parked on the neuron soma by laterally translating microscope stage while imaging their relative positions with a camera attached to microscope visualization port. Interference signal was recorded from a neuron for a period of 3-4 minutes. Next, Glutamate (Glu: 500 μM final concentration) was added into the cell culture device reservoir for stimulation and interference signal was collected. After 10-12 minutes of data collection, Na-channel inhibitor Tetrodotoxin (TTX: 500 nM final concentration) was added to the device and interference signal was

collected for a further 6 minutes. Typical temporal changes in OPD observed from these experiments are summarized in Fig. 3.1 (C). OPD changes in the form of optical pulses above the baseline are clearly visible in neurons with (+Glu) and without stimulation. Cultures of cortical rat neurons are well known to form interconnected neuronal networks of excitatory glutaminergic synapses that produce spontaneous random firing in absence of external stimuli. With the addition of exogenous Glutamate, neuronal firing rate is increased which is reflected in greater number of transient optical pulses. The effect of TTX, a highly potent sodium ion channel blocker known to effectively kill neuronal firing[65], is clearly noticeable by a reduction in optical pulses. Recorded optical pulses appear to exhibit single or multicyclic oscillations with short to relatively broad temporal widths (Fig. 3.1 (D)). In-depth analysis of the optical pulses and their temporal characteristics are discussed in the subsequent sections.

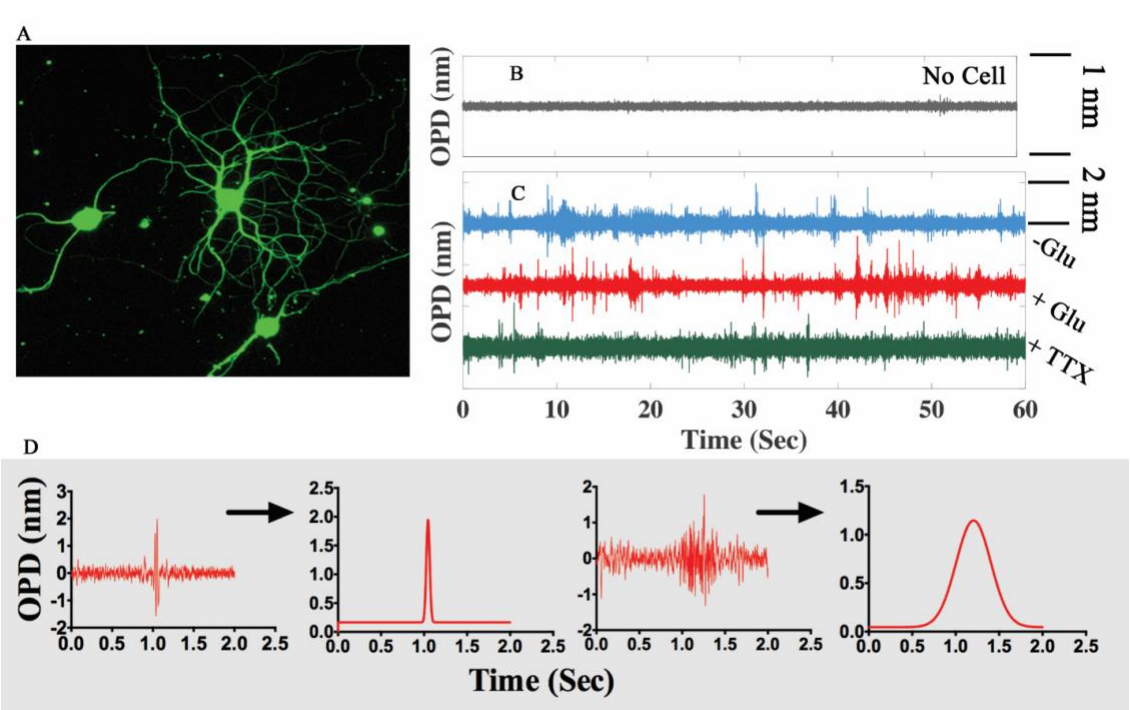

Figure 3.1: Representative optical signals recorded from individual neurons in a network. (A) Fluorescence immuno-stained (primary β-III-tubulin antibody- Alexa Fluor 488) image of networked rat cortical neurons used in our experiments. (B) & (C) Temporal change in OPD under different experimental conditions (no cell, cell without any stimulation, cell with Glutamate stimulation, cell with TTX inhibition) showing a non-periodic train of optical signal oscillation from unstimulated and stimulated neurons which die out when inhibited with TTX. (D) Isolated burst of individual optical pulses that have wave packet like signal pulse characteristics and their corresponding envelopes show variation in temporal pulse width.

To compare the electrical firing of the neurons under these different stimulation conditions and for comparison of the detected optical signal with electrical signal generated during neuronal firing, electrophysiology studies were carried out on cultured

cortical neurons. For each experiment, a single neuron was patched in a network of cultured cortical neurons, and under current clamp of whole cell patch-clamp recording, voltage trace was recorded over time. Spontaneous electrical activity of a networked neuron is reflected in the electrical spikes (Fig. 3.2 (A)) in the absence of exogenous Glutamate stimulation. After few minutes of recording, the same patched cell was stimulated by adding Glutamate in the culture media. Time lapse recording of neuron firing after addition of Glutamate is shown in Fig. 3.2 (A), which clearly shows that Glutamate increases the rate of firing. In another experimental set, patched neuron was subjected to stimulation by Glutamate and subsequently TTX was added to block the sodium ion current. As shown in Figure 3.2 (B), the TTX diminishes firing activity significantly. A few sub-threshold firings can be seen in presence of TTX, which explains the presence of some small optical pulses. The optical results are in close agreement with the electrophysiology recording, where similar outcomes for stimulation and inhibition were observed in the detected optical signal.

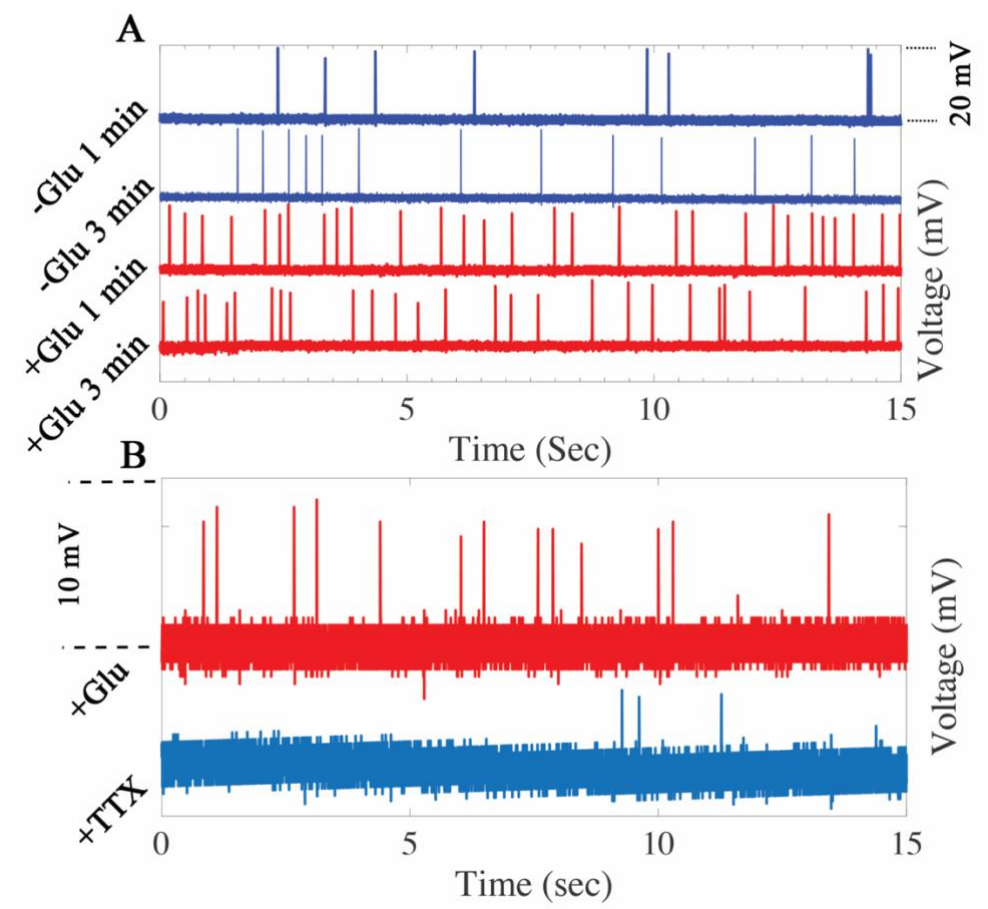

Figure 3.2: Patch clamp recording of action potential firing from single neurons. (A) Pre- and post-glutamate stimulation voltage recording (current clamp) of randomly generated action potential spikes in networked neurons. (B) Inhibition of electrical activity with addition of TTX. Recordings in (A) and (B) are from two separate experiments.

Rectified optical signal (Fig. 3.3 (A)) shows a train of optical pulses and each optical pulse envelope can be characterized by its peak magnitude and temporal width. Results summarizing the firing rate (no. of pulses), peak magnitude, and temporal width for unstimulated (-Glu), stimulated (+Glu), and inhibited (TTX) neurons are shown in Fig. 3.3

(B)-(D). As expected, the firing rate increases in case of stimulated neurons and diminishes under TTX inhibitions. In the case of TTX administered neurons, few optical pulses were observed, predominantly with short temporal activity window- probably due to the weak, subthreshold firing. In case of spontaneous and stimulated neuronal firing, wider optical temporal period was observed. Wider temporal activity windows are more prominent in the unstimulated neurons, arguably because of the recuperation time availed by the neurons due to lack of aggressive firing. In case of peak amplitudes of the optical pulses, a wide range of distribution was observed (Fig. 3.3 (D)), which is almost identical in case of stimulated and unstimulated neurons (as Glutamate stimulation only enhances the firing rate, and does not affect the amplitude of action potentials), and close to the baseline in case of TTX inhibition.

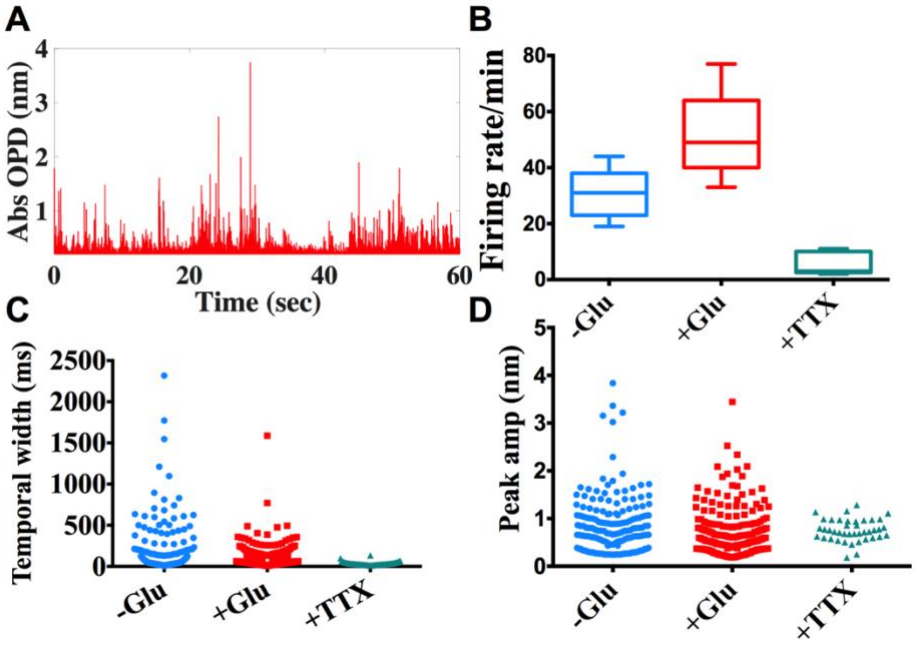

Figure 3.3: Analysis of extracted features from individual optical pulse (Fig. 2) (N=5 neurons). (A) Optical signals are rectified, followed by envelope detection of each pulse. (B) Firing rate of unstimulated vs stimulated/inhibited neurons, ($p<0.05$ for -Glu vs +Glu

and -Glu vs +TTX). (C)-(D) scatter plots of envelope width, envelope peak under no stimulation, Glutamate stimulation, and TTX inhibition conditions, respectively.

3.3. Discussion

Detected optical pulses quantify change in OPD, which is a product of physical path length and refractive index. Any modulation of OPD is either due to changes in cell morphology resulting in alterations in cell thickness (height) or refractive index, or a combination of both. Electro-optic effect and dynamic mass redistribution due to depolarization of the cell membrane are potential mechanisms that can modulate cell's refractive index. Modulation in refractive index due to electro-optic effect is expected to temporally follow the AP signal. Electrical activity in the cell membrane is not known to trigger a downstream cellular pathway that could potentially induce cellular mass redistribution resulting in bulk refractive index change. The optical pulses do not follow the AP signal temporally, and hence each optical pulse is a result of change in geometry morphology of the neuronal cell body.

To understand the nature of morphological changes we have analyzed the magnitude, frequency and temporal characteristics (width and shape) of individual optical pulses. Morphological changes can manifest as whole cell deformation (isovolumetric or non-isovolumetric), or fluctuations of the cell membrane. Swelling and contraction have been observed in neurons (nerve fibers, giant squid axons) following action potential, and displacement changes of 0.5-5 nm have been reported[66-69]. While some have proposed underlying cause to be transport of water and ions between the cell and extracellular media[70], others have suggested cation exchange could change the membrane density and generate electrostatic forces in the nerve fibers, creating lateral expansion[71].

Cellular deformation in excitable HEK cells has been studied with interferometry to explore various plausible mechanistic pathways for electromechanical-optical transduction[72]. The study by Oh *et al*. concluded that direct coupling between membrane potential and membrane tension results in whole cell deformation giving rise to measured change in optical phase signal. No such experimental studies have been reported on mammalian neuron. Membrane displacements can be induced by a transient change in membrane potential, mediated by electromechanical coupling phenomena such as flexoelectricity and piezoelectricity[73]. Previous theoretical[74,75] and experimental[66,76] studies using AFM/Electrophysiology have shown that voltage-dependent motions can arise from a fundamental electromechanical coupling between membrane potential and membrane mechanical properties.

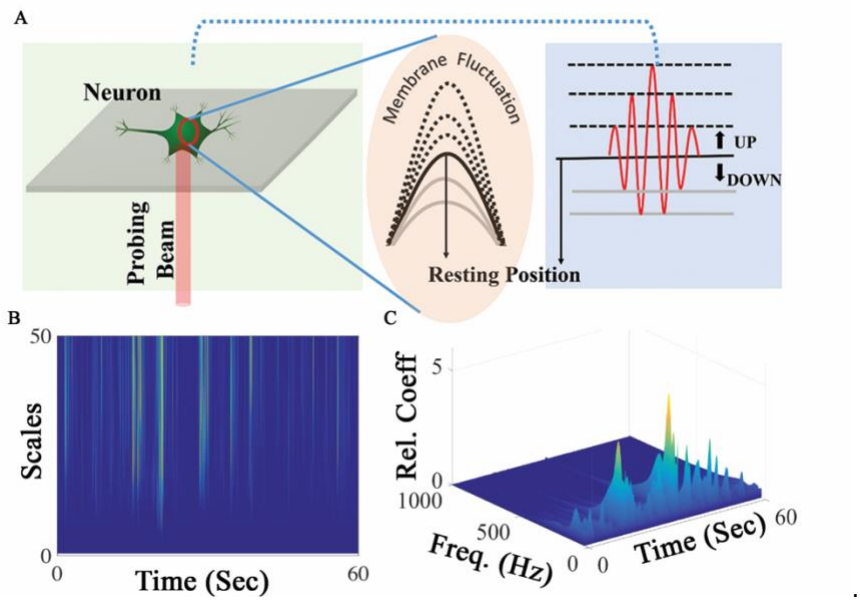

Figure 3.4: Analysis of extracted features from individual optical pulse (Fig. 2) (N=5 neurons). (A) Optical signals are rectified, followed by envelope detection of each pulse. (B) Firing rate of unstimulated vs stimulated/inhibited neurons, ($p<0.05$ for -Glu vs +Glu

and -Glu vs +TTX). (C)-(D) scatter plots of envelope width, envelope peak under no stimulation, Glutamate stimulation, and TTX inhibition conditions, respectively.

We consider the two aforementioned different types of cellular deformation under isovolumetric conditions which can result in membrane displacement: whole cell deformation or localized deformation of the lipid bilayer (Fig. 3.6). Assuming the cell refractive index remains constant, estimated average membrane displacement values are 9 nm and 2.4 nm for whole cell and lipid bilayer deformation cases, respectively (calculation shown in next section, section 3.3.1). These values are larger in magnitude compared to experimentally measured membrane displacement in giant squid axons, nerve bundles, and HEK cells. Even after considering differences in cell types and inaccuracies in refractive index values due to paucity of experimental data in live cells, our displacement estimates are large. The sandwich geometry of the cell culture device with two references surfaces to generate interference signal can significantly amplify the measured OPD. Cell membrane deformation (Fig. 3.6), be it local or global, will deflect the membrane plane with respect to the direction of incident light. Even slight membrane deflection can dramatically alter the geometrical path traversed by light and hence the OPD. For example, a 0.5^{o} deflection in membrane plane can change the OPL by ~3 nm, for a cell culture device gap of 80 μm. Considering contribution of amplified OPD due to membrane deflection, estimated membrane displacement in the lipid bilayer are of comparable range to reported values (0.2-5 nm[66-68,72,76,77]).

Biological membranes can support stationary resonant modes of vibration as well as travelling waves of various forms including surface acoustic waves[78-81]. The top surface (cell-media interface) of the neuronal cell body is a curved membrane under tension that is attached to the bottom (cell-glass interface), and can support 2D Eigen modes of

vibration. Local temperature-dependent nano-mechanical oscillation at characteristic frequencies ranging from 0.8 to 1.6 kHz with amplitudes of 3 nm have been detected in live yeast cells[80]. Standing waves due to whole cell deformation will produce narrow and discrete frequency modes of oscillation. Any other modes besides the fundamental mode of oscillation will wash out the measured OPD change in our measurement setup. Lipid monolayers have shown to support propagating 2D pressure pulses[81]. A recent experimental study has characterized the nature of propagating acoustic waves in lipid monolayers[79]. Depending on the magnitude of excitation, different lateral compressibility regimes of lipid monolayer support propagating pulses of varying timescales and frequencies bandwidths. In the nonlinear compressibility regime, a soliton like pulse propagation with a wide frequency spread (few Hz to 300 Hz) was observed. While in the linear compressibility regime, a transient wave with a reduced amplitude and a narrow frequency distribution travels in the lipid monolayer[79]. Wavelet analysis (Fig. 3.4 (B)) of recorded optical signal shows a wide and continuous frequency bandwidth (Fig. 3.4 (C)) of membrane vibration in individual optical pulses with a bandwidth of ~200 Hz, centered around 70-100 Hz (Fig. 3.4 (C)). The characteristics frequencies and wide bandwidth of spectral frequency distribution of the optical pulses are comparable to the reported values in lipid monolayer[79].

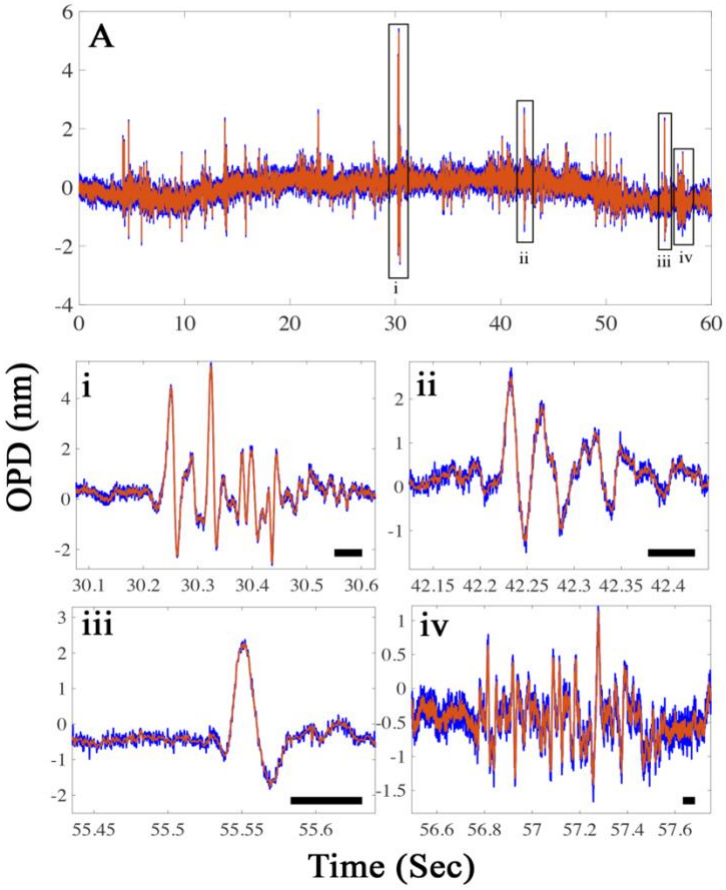

Figure 3.5: Optical pulses of varying temporal characteristics (A) Raw (blue) and filtered (orange) 60 sec extract of optical recording from a signal neuron showing a train of randomly spaced optical pulses, (i-iv) Zoomed section of select windows from optical recordings in (A) showing single or multicyclic oscillation of optical pulses with varying temporal widths (scale-bar=50 ms). The red overlay is a filtered version of the unfiltered (blue) signal.

The electromechanical coupling mechanism is pivotal in dictating the temporal characteristics of the observed optical pulses. Shown in Fig. 3.5 is the optical recording and zoomed in portions of individual optical pulses of different temporal widths. The

shape and timescale of membrane displacement as reflected in the optical pulses are different from the AP signal. Timescale of recorded AP are in the 5-7 ms range, whereas the temporal width of optical pulses ranges from 20-300 ms, with an average of 48 ms for 85% of the detected optical pulses. On closer examination of optical pulses shown in Fig. 3.5 (ii) and 3.5 (iv), it can be argued that these optical pulses are a collection of single cycle optical pulse shown in Fig. 3.5 (iii), generated by closely bunched APs. Whereas, optical signal in Fig. 3.5 (iii) is a multicyclic pulse, which appears to be a dampened oscillation. Typically, AP signal spikes in a neuronal network exhibit minimal variation in amplitude and temporal width. In our case, for a given electrical input (AP), two different types of mechanical outputs (membrane oscillation) of varying magnitude, shape and time scale are generated. There are two plausible explanations for observed multiple outputs; either the two different types of observed optical pulse are generated due to time varying electrical-to-mechanical coupling efficiency or the multicycle optical pulse is unrelated to AP propagation. It is possible that the membrane supports both, individual single cycle pulses and multicyclic pulses, depending on the mechanical input strength as has been observed in transverse oscillation of lipid monolayer in response to propagating surface wave[79]. The shape and timescales closely resemble the detected optical pulse, which strongly suggests the coexistence of a mechanical surface wave in conjunction with action potential propagation. The strength of electromechanical coupling, mode of membrane vibration, and gap between successive AP firings contribute to the observed oscillatory time-period of optical pulses. In order to tease apart the different kinds of oscillations, and to determine whether these are in response to a single AP input or a train of AP spikes, future studies will take advantage of optogenetics to analyze the concordance between single and multi-spike trains and the composition of the optical signal[82].

3.3.1 Estimation of physical displacement from measured optical path-length changes

We consider two cases under the assumption of isovolumetric condition to estimate physical displacement in the neuron during AP propagation from the measured changes in optical path-length. In case#1 physical displacement due to whole cell (Fig. 3.6 (B)) deformation is considered, whereas only deformation of lipid membrane (Fig. 3.6 (C)) is considered in case#2.

Optical path-length difference (OPD) between the two reference surfaces of the neuronal cell culture device before and after the excitation of AP for case#1 can be written as,

$$OPD_{BE}(t) = n_m d_s + \frac{1}{A}\int_A [n_c(x,y,z) - n_m]\, d_c(x,y)dA$$

$$OPD_{EX}(t) = n_m d_s + \frac{1}{A}\int_A [n_c(x,y,z) - n_m]\, d_c(x,y)dA \pm \frac{1}{A}\int_A [n_c(x,y,z) - n_m]\, \Delta d_c(x,y)dA$$

Optical path-length difference between the two reference surfaces of the neuronal cell culture device before and after the excitation of AP for case#2 can be written as,

$$OPD_{BE}(t) = n_m d_s + \frac{1}{A}\int_A [n_c(x,y,z) - n_m]\, d_c(x,y)dA + \frac{1}{A}\int_A [n_l(x,y,z) - n_m]\, d_l(x,y)dA$$

$$OPD_{EX}(t) = n_m d_s + \frac{1}{A}\int_A [n_c(x,y,z) - n_m]\, d_c(x,y)dA + \frac{1}{A}\int_A [n_l(x,y,z) - n_m]\, d_l(x,y)dA \pm \frac{1}{A}\int_A [n_l(x,y,z) - n_m]\, \Delta d_l(x,y)dA$$

where

OPD_{BE}=*OPD* before neuronal firing,

OPD_{EX}=*OPD* during neuronal firing,

n_m=refractive index of the media,

n_c=refractive index of the cell,

n_l=refractive index of the lipid bilayer,

d_s= gap thickness of the sandwich cell culture device,

d_c=height of the cell,

d_l=thickness of the lipid bilayer,

$\pm\Delta d_c$= change in cell height,

$\pm\Delta d_l$=fluctuation of the cell membrane thickness due to membrane deformation.

A=cross-section area of the incident optical beam on the neuron.

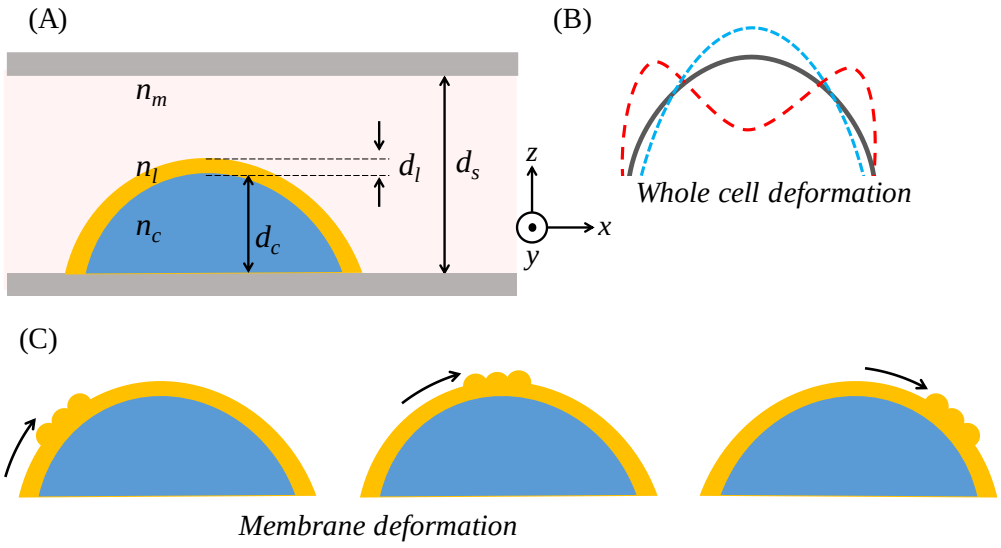

Figure 3.6: Illustration of two different types of cellular deformation under isovolumetric condition which can result in measured OPD changes. (A) Geometry of the neuron used to calculate change in physical thickness for whole cell (B) and membrane (C) deformation, respectively.

Change in OPD due to excitation of AP for case #1 (*WC*-whole cell deformation) and case #2 (*MD*- membrane deformation) is,

$$\Delta OPD_{WC} = OPD_{EX} - OPD_{BE} = \pm\frac{1}{A}\int_A [n_c(x,y,z) - n_m]\,\Delta d_c(x,y)dA$$

$$\Delta OPD_{MD} = OPD_{EX} - OPD_{BE} = \pm\frac{1}{A}\int_A [n_l(x,y,z) - n_m]\,\Delta d_l(x,y)dA$$

For Glutamate stimulated neuron, the mean *ΔOPD* changes after subtracting the baseline activity was calculated to be 0.64 nm. Assuming the refractive indices of various compartments remain constant, physical change in cell height for case #1 (Fig. 3.6 (B)) can be written as follows,

$$\int_A \Delta d_c(x,y)dA = \frac{\Delta OPD}{n_c(x,y,z) - n_m}$$

$$\Delta d_c = \frac{0.64}{1.40 - 1.33} = 9\ nm$$

For case #2 (Fig. 3.6 (C)), physical change in membrane thickness can be derived as follows,

$$\int_A \Delta d_l(x,y)dA = \frac{\Delta OPD}{n_l(x,y,z) - n_m}$$

$$\Delta d_l = \frac{0.64}{1.60 - 1.33} = 2.4\ nm$$

Available literature values of refractive index of cell culture media[83], cell[84] and cell membrane[85] have been used in the above calculations.

Recent theoretical modeling and experimental studies of electromechanical coupling in plasma membrane of axons suggests existence of some form of propagating mechanical wave. Two different theoretical models have examined the input-output relationship in an axonal system. Heimburg *et al*. have proposed the soliton model for action potential, in which the propagation of action potential ties in with changes in

hydrodynamic and thermodynamic properties of the membrane, creating local compression in membrane and forcing the transition from a fluid to gel phase, along with a release of heat, and vice versa[86]. Hady *et al*. have proposed a model of propagating mechanical action waves in axons triggered by propagation of AP with both lateral and longitudinal displacement of membrane[68]. In the soliton model proposed by Heimburg *et al*. there is one-to-one correspondence in shape and time scale of electrical and mechanical signals, though it should be noted that in soliton model, entropy driven mechanical pulse propagation induces membrane depolarization and AP propagation. The action wave model predicts membrane displacement that is concomitant to AP in timescale but not in shape. A symmetrical voltage input pulse will result in a single cycle displacement pulse, whose symmetry depends on the relative velocities of AP and mechanical pulse propagation. Single cycle optical pulses in our experiments look remarkably similar to predictions of the action wave model. It should be noted that the above-mentioned models are based on axons, which are of cylindrical geometry, as opposed to our experiment and analysis on hemispherical neuron soma. Transient oscillatory displacement of the lipid bilayer, frequency and temporal characteristics of oscillations, strongly indicates existence of a propagating surface wave on the neuronal cell membrane triggered by AP.

Chapter 4

All Optical construction, manipulation, stimulation and detection of electrical activity in a neural circuit

4.1 Introduction

The Reductionist aproach of neuronal research aims to look at neuronal interactions at the single neuron and action potential level and build up the understanding by studying these interactions first in simple, and then, in more complicated neuronal circuits, by introducing controllable variables and inputs, and observing the output signals achieved in response to these. To construct and control such a circuit in a very deliberate manner, we need tools that can enable (a) the placement of participating neurons and other cell types in known positions with respect to other neurons/ circuit components (for co-cultures), (b) microsurgery/ intentional damage or incision, or insertion of molecules to introduce known variables or control factors, (c) stimulation or inhibition of celular activity in a spatially and temporally precise manner with cellular specificity, and (d) non invasive functional imaging of such neuronal firing with cellular as well as sub cellular specificity, with millisecond time resolution to record the electrical and other cellular activities from multiple cells simultaneously. High quality widefield structural imaging is also desirable to study the morphological changes of the sample over time. While the structural imaging techniques currently available (DIC imaging, 2-ph microscopy, confocal microscopy, etc) are quite satisfactory on most counts, the tools required for the other steps mentioned have been introduced much more recently, and need more development to standardize them for wide acceptance in the scientific community. These tools need to accomplish these tasks in a non invasive, non contact manner in order to ensure unhindered, prolonged study in a sterile manner in an environment as free as possible from

unintentional deviations from the indeginous conditions. Using optical techniques to accomplish all these aims would be an ideal choice, and would have significant advantages like: a) non invasive and non destructive, b) can continue unrestricted studies for extended period of time, c) wide field implementation is relatively easy, d) no contamination issues e) high spatial and temporal specificity.

The previous chapter describes the proposed label free optical technique that can detect electrical activity in mammalian neurons without the need for signal averaging or introduction of contrast agents with sub cellular and sub millisecond resolution and demostrates it for the first time with mammalian neurons. In this chapter we briefly discuss other optical techniques that can be used to achieve the goal of all optical construction, manipulation, stimulation to allow an all optical read out in a neural circuit, with single neuron and single action potential stimulation and detection precision. The ability to implement this is a transformational advance that can help open new frontiers in neurological research with increased control over in vitro neuronal communication studies.

While majority of the text in the dissertation discusses optical detection, this chapter discusses the other components of the flowchart shown in Fig 4.1.

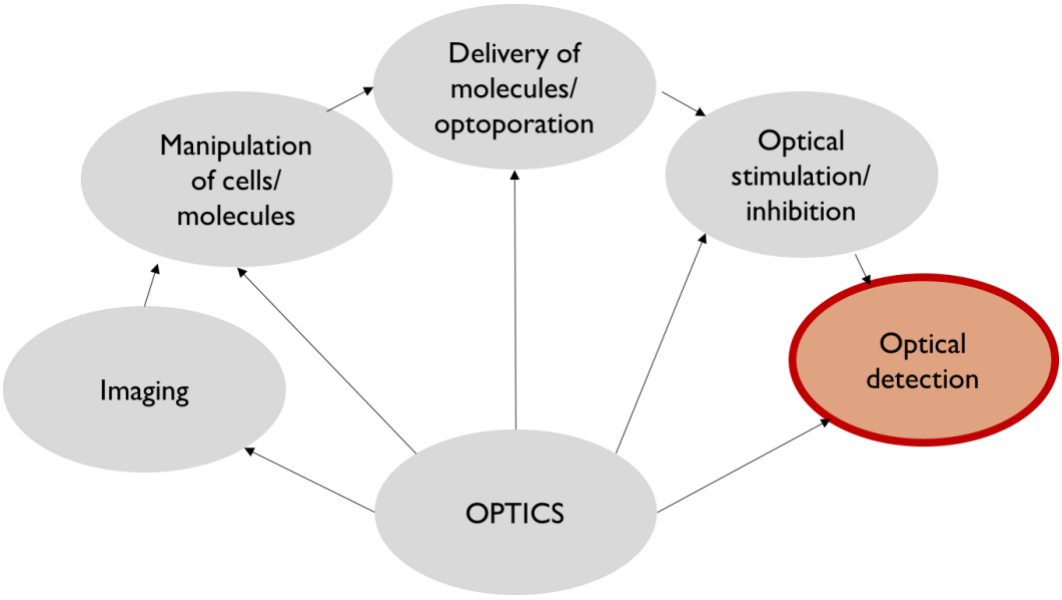

Figure 4.1: A flowchart diagram outlining the major components of an all optical neural circuit construction, manipulation and read out system.

4.2 Optical positioning

Optical positioning of cells and molecules can be achieved by using a technique commonly referred to as 'optical tweezing' or 'optical trapping', which was first experimentally demonstrated in 1986 by Ashkin *et al*[87]. They suggested that single beam gradient traps could stably trap dielectric particles ranging from 25 nm to 10 μm in size. it utilizes the two opposing forces acting on the particle at the focus or beam waist due to the gradient pressure and radiation pressure. The gradient pressure is caused due to an axial intensity gradient, giving rise to a backward force component in the direction of the gradient. The radiation pressure gives rise to a scattering force that is proportional to the optical intensity and points in the direction of the incident light. It has been shown that the single beam radiation pressure trap can be used to trap particles over the full spectrum of Mie and Rayleigh particles[87].

The scattering force is mostly a result of primary reflection at the interface, but is also due to higher-order scattering and absorption of incident photons and acts along the direction of light propagation. The gradient force on the other hand, constantly pulls the object towards the position of highest intensity, which creates an optical equilibrium position. Any displacement from this position results in a restoring force, which 'traps' the particle in this equilibrium position. The optical gradient force is typically on the order of pico-Newtons, which limits the size of the particle that can effectively be trapped. A tightly focused laser spot is necessary for a stable three-dimensional optical trapping, but some degree of this force can be achieved even with a weaker focus.

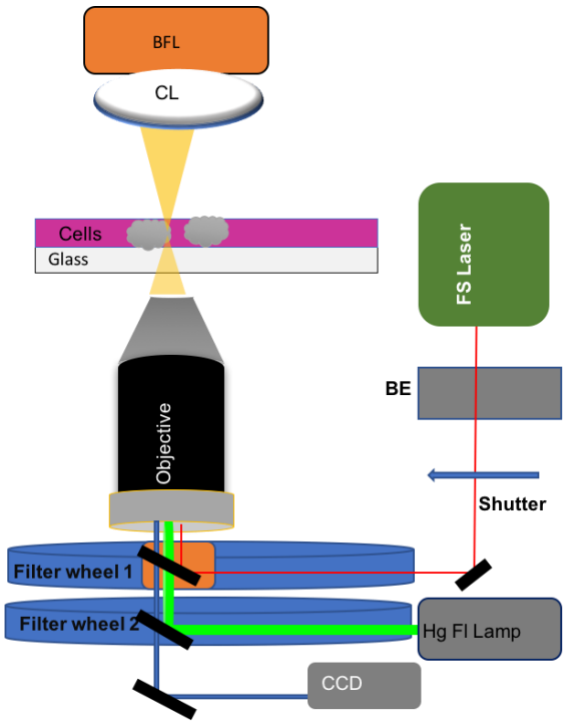

Figure 4.2: A schematic diagram showing the optical setup to implement optical trapping system used. BFL- Bright-field Lamp, CL- Condenser Lens, BE- Beam Expander.

4.2.1 Materials and methods

4.2.1.1 Rat Cortical Neuron culture

All experimental procedures were conducted according to UT Arlington Institutional Animal Care and Use Committee approved protocol. Cortical neurons were isolated from 18-day rat embryos after cortical tissues were dissected, cleaned (meningeal layer), enzymatically dissociated (0.125% trypsin in L-15 medium) for 20 minutes at 37 ^{0}C. About 50 μl of this solution is taken in a pipette and slowly pipetted into the glass bottomed petridish aftfer it is placed on the microscope stage to optically trap neurons (discussed in the next section). Glass bottomed 35 mm petridish are coated with Poly-D-lysine (PDL, 0.01%, Sigma) pre-coated and incubated at room temperature for 6-8 hours. About 1 ml culture media (Neurobasal medium supplemented B-27 with BDNF and NT-3, 10 ng/ml) at 37 ^{0}C is pipetted into these devices. For patch clamp experiments, dissociated cortical neurons (40,000/device) were seeded on Poly-D-lysine (PDL, 0.01%, Sigma) were grown in 35 mm glass bottom petri dishes, and the culture media was changed every 3 days.

4.2.1.2 Optical setup

A schematic diagram of the experimental setup is shown in Figure 4.2. A tunable (690 - 1040 nm) Ti:Sapphire laser (Newport Spectra-Physics, Inc.) with a repetition rate of 80 MHz and pulse width ~100 fs) is used in mode lock off position to produce a continuous beam which is directed toward the sample after passing through a beam expander by a dichroic mirror (in filter wheel 1) through an inverted optical microscope (Nikon eclipse Ti). A 100x (NA = 1.4) objective was used to focus the laser beam to a diffraction limited spot at the top surface of the cell. A second dichroic mirror (in filter wheel 2) was used to reflect the fluorescence excitation light from the mercury lamp (Nikon) along the same path as the fs laser, and appropriate excitation and emission

filters were used to transmit and collect the appropriate bands of visible light to and from the sample, and block any remaining backscattered laser light. All images were acquired by cooled EMCCD (Cascade, Photometrics) and processed with imageJ (NIH) software. The duration of fs laser beam irradiating each sample was controlled by Filter wheel 1, which is controlled by the same software as the motorized XY Stage (TLX 4000). There is also an external mechanical shutter (Uniblitz Inc.) which can be used for finer control of the on-off time. The sample-site laser beam power was controlled by the fs laser software (Mai Tai), with fine adjustments made by altering the orientation of the polarizer (P). The sample-site beam power (after the objective) was calculated by multiplying the transmission factor of the microscope objective with the power measured at the back aperture of the objective.

The glass bottomed petridish coated with PDL with 1ml NBM is firmly placed on the sample holder of the microscope, which also has a homemade incubator built in to maintain temperature and humidity levels, as well as CO_2 input to maintain pH levels. A thermometer is attached to the incubator to monitor the temperature.

The laser focus spot is marked with respect to the camera view and the sample stage is moved to bring the area of interest in the view. The solution containing the suspended neurons is slowly pipetted into the dish and the laser focal plane is brought up with respect to the petridish surface to trap a neuron. After trapping the neuron in a plane above the petridish surface, the objective is brought down in z–axis to a plane below the glass surface and held there for a few milliseconds to help the neuron stick to the surface of the PDL-Coated glass. This process is repeated, and after trapping each neuron, the stage in moved in XY plane to achieve the desired position, and then the neuron trapped in the beam waist is brought down to the PDL coated surface by moving the focal plane

down in z-axis. The process is diagrammatically explained in the following figure (Fig. 4.3).

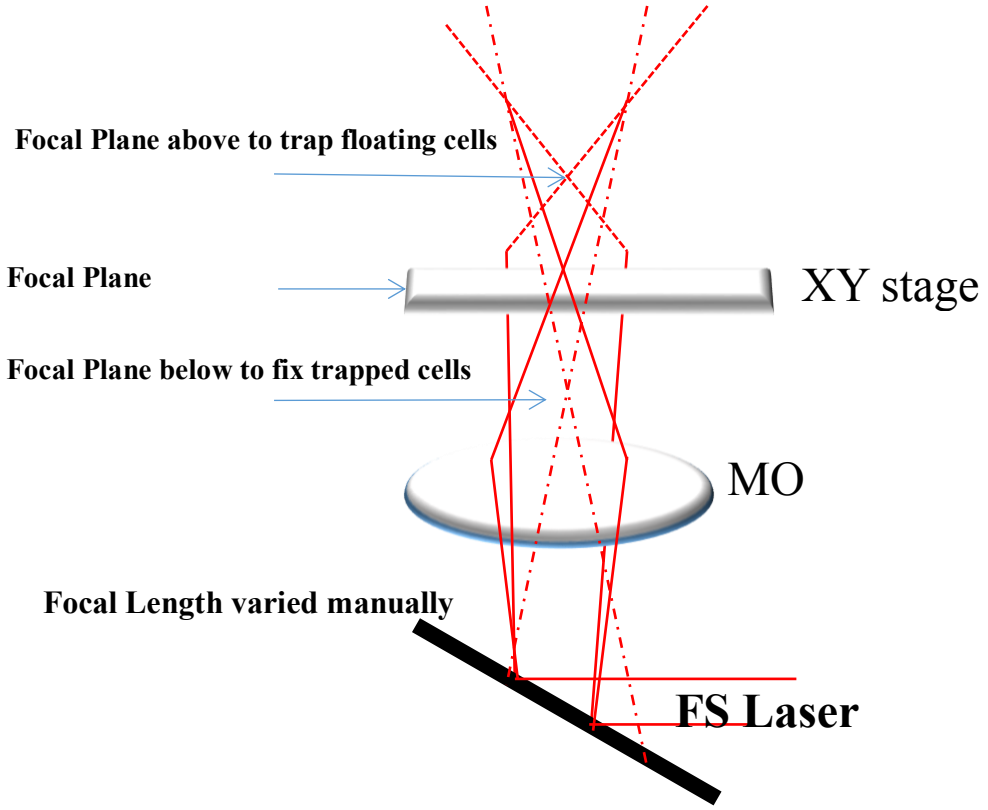

Figure 4.3: A schematic diagram showing the principle of optical trapping system used to position cells at preassigned locations. MO: Microscope Objective.

4.2.2 Results for optical trapping

Placement of neurons and other biological samples was done multiple times using optical trapping setup mentioned above. These were arranged in known and recognizable patterns to differentiate from random and naturally occurring placement of cells. Some of the results achieved are shown in the following figures.

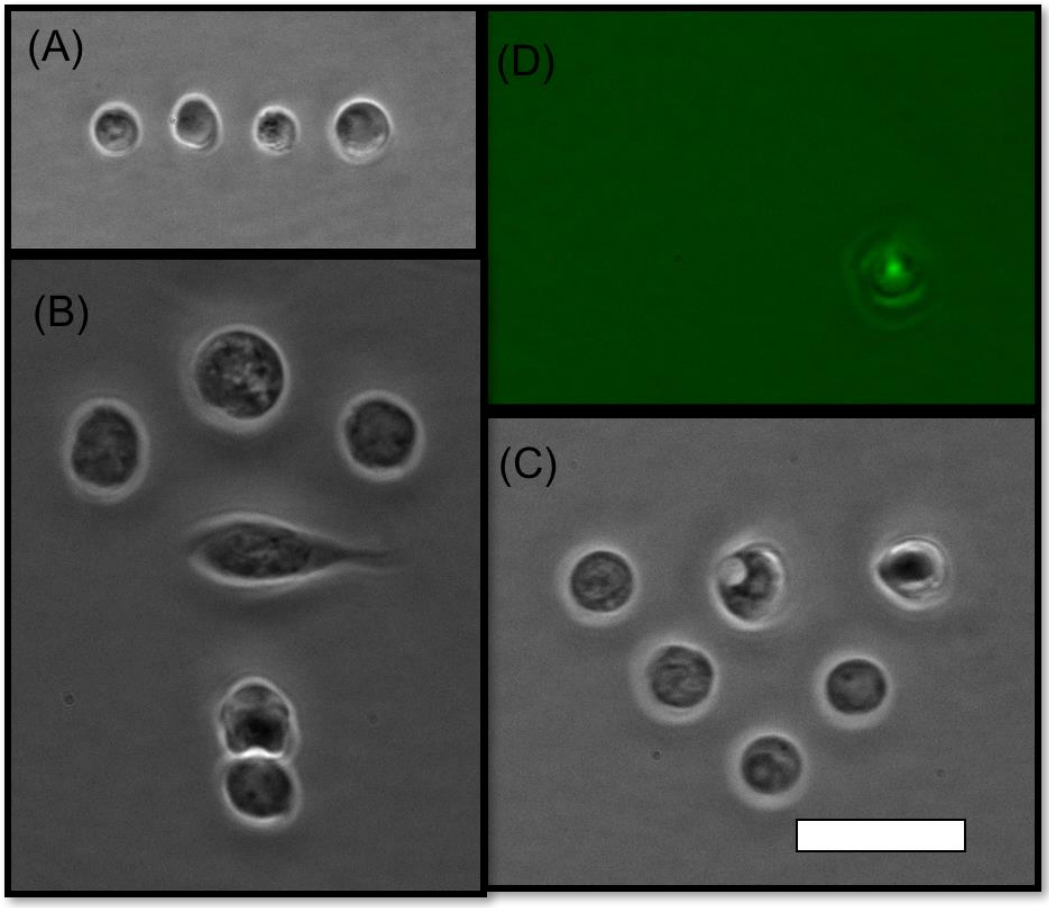

Figure 4.4: Patterns achieved by optically trapping and positioning of rat cortical neurons- (A) straight line, (B) Rabbit paw (C) Triangle. (D) Single neuron held in an optical trap. Scale bar: 10 μm.

It is also possible to create co-cultures of different cell lines and place different cells in proximity to each other to study the communication and behavior of these cells in such environment in a controlled manner. An example is shown in the figure below where astrocytes are introduced into a cultured neuron network, creating a controlled co-culture.

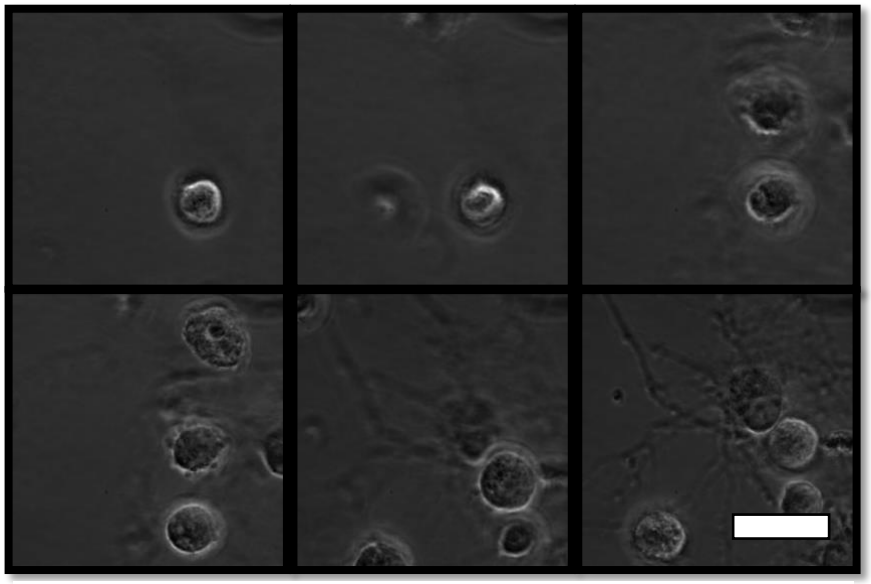

Figure 4.5: Astrocyte-neuron co-culture. Neurons are cultured on a petridish and astrocytes are optically trapped and placed sequentially on the axon and dendritic networks. Scale bar: 10 μm.

4.3 Optoporation

4.3.1 Introduction

Optoporation is a laser based optical method of delivering extraneous molecules, by creating a transient hole in the membrane of a biological sample. This is done by exposing the sample to a focused pulsed laser microbeam of sufficient intensity.[88] Optoporation enables targeted delivery of molecules with cellular specificity in a sterile, non-contact manner. Many hypotheses have been proposed, such as plasma formation, dielectric break down, cavity formation, photo-acoustic effects[89,90], local heating, shock wave formation[91,92], and the process responsible for the poration depends on the laser intensity and pulse width. In this case of femtosecond pulsing laser, direct plasma breakdown is the primary cause of the observed optoporation effect.

4.3.2 Materials and methods

4.3.2.1 Sample preparation

A rat eye was surgically removed and 5 μl of 1 μM dye (Alexa 594 Phalloidin) was injected into the retina. The eye was then placed on a glass bottomed petridish with 1 ml culture media (Neurobasal medium supplemented B-27 with BDNF and NT-3, 10 ng/ml) at 37 ^{0}C, and immediately placed on the microscope stage for the optoporation. The final concentration of the dye in the eye was about 100 nM.

4.3.2.2 Optical setup

A schematic diagram of the experimental setup is shown in Figure 4.2. A tunable (690 - 1040 nm) Ti:Sapphire laser (Newport Spectra-Physics, Inc.) with a repetition rate of 80 MHz and pulse width ~100 fs) is used in mode lock on condition to produce a pulsed beam which is directed toward the sample after passing through a beam expander by a dichroic mirror (in filter wheel 1) through an inverted optical microscope (Nikon eclipse Ti). A 10x (NA = 0.25) objective was used to focus the laser beam to a diffraction limited spot at the top surface of the cell. A second dichroic mirror (in filter wheel 2) was used to reflect the fluorescence excitation light from the mercury lamp (Nikon) along the same path as the fs laser and appropriate excitation and emission filters were used to transmit and collect the appropriate bands of visible light to (green) and from (red) the sample, and block any remaining backscattered laser light. All images were acquired by cooled EMCCD (Cascade, Photometrics) and processed with imageJ (NIH) software. The femtosecond laser beam can be blocked by using filter wheel 1, which is controlled by the same software as the motorized XY Stage (TLX 4000). The duration of fs laser pulses irradiating each sample was controlled by an external mechanical shutter (Uniblitz Inc.). The sample-site laser beam power was controlled by the fs laser software (Mai Tai), with fine adjustments made by altering the orientation of the polarizer (P). The sample-site

beam power (after the objective) was calculated by multiplying the transmission factor of the microscope objective with the power measured at the back aperture of the objective. Fluorescence and bright field images were taken before and after optoporation experiments to check if the fluorescent dye enters the desired cell.

A 20X objective (0.5 NA) and 10X objective (0.25 NA) are used, even though 100X is better suited for optoporation because of its high NA, as the sample is curved and thick, requiring a longer working distance to reach the intended plane. The wavelength used is 795- 800 nm with the average optical power being kept around 90 mW (~1 nJ/pulse). The duration of the exposure is varied from cell to cell from 20 to 40 ms.

4.3.3 Results

Optoporation was successfully done on retinal ganglion cells of a rat eye at multiple sites. Alexa 594 Phalloidin, cell-impermeable dye for staining filamentous actin dye molecule has been successfully inserted into these cells. The results are shown in the figures below. Optoporation is done in a pattern easily recognizable as intentional to differentiate from any auto fluorescence or fluorescence from dead cells or debris. Fluorescence images are taken before and after each optoporation to ensure that the dye has entered the cell(s) of interest. The change of fluorescence indicates the presence of the dye inside the cell after optoporation. The brightfield and fluorescence images are taken by using fluorescence as well as brightfield illumination with a high exposure time to allow the simulataneous visualization of structural imaging and fluorescence.

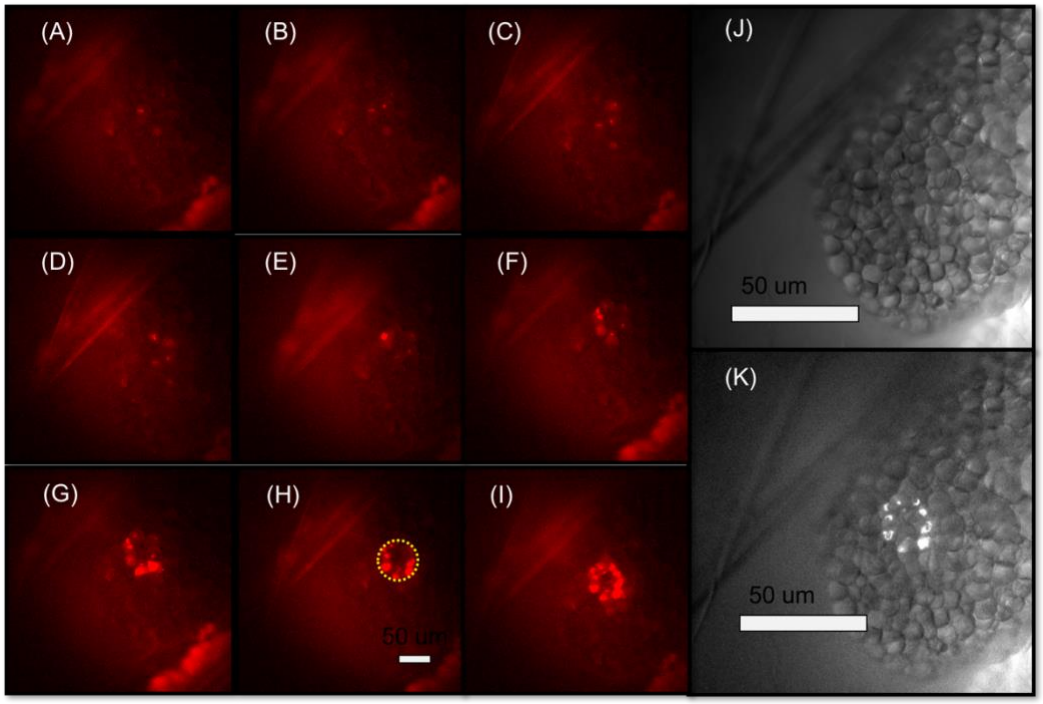

Figure 4.6: Demonstration of optoporation in retinal cells of rat eye. (A)-(I) Fluorescence images demonstrating the step by step delivery of Alexa 594 Phalloidin in neurons to create a circular pattern. (J) Brightfield and fluorescence image before the optoporation, and (K) Brightfield and fluorescence image after the optoporation to show that the dye has permeated the cells. Optoporation is performed with a 10X microscope objective (0.25 NA) objective. Scale bar: 50 μm.

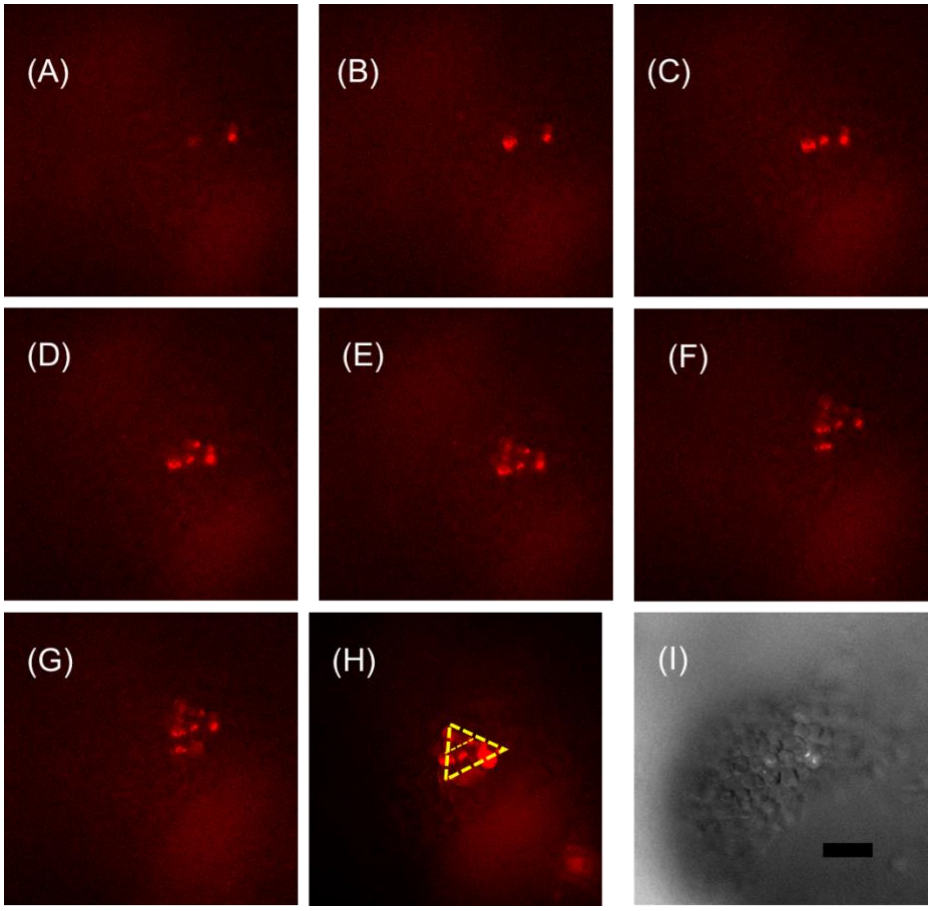

Figure 4.7: Demonstration of optoporation in retinal cells of rat eye. (A)-(H) fluorescence images demonstrating the step by step delivery of Rhodamine Phalloidin in neurons to create a pyramidal pattern. (I) Brightfield and fluorescence image before the optoporation to demonstrate the lack of dye in the neurons. Optoporation is performed with a 20X microscope objective (0.5 NA). Scale bar: 50 μm.

Parts of the images in Fig 4.6 and 4.7 are out of focus since the tissue is curved. These figures show the optoporation at different regions of the rat eye. This experiment demonstrates that optoporation can be used to deliver impermeable molecules into biological samples. This has been used to deliver opsins which can allow sensitization of cells to light, and allow optogenetic control of cellular activity.

In the next section, we will discuss how optical stimulation, including techniques like optogenetics, can be used to control cellular activity in a spatially and temporally controlled manner.

4.4 Optical Stimulation

Cellular activity can be initiated by a variety of cues, including, and not limited to, electrical, chemical, magnetic, and light. Traditionally, electrical and chemical methods of stimulation have been used to initiate electrical activity. While both these methods can target individual cells and with temporal precision, it is hard to achieve, especially with chemical methods of stimulation. This requires specific amounts of the stimulants being puffed in contact with or in vicinity of the target cell, synced with a clock to time the stimulation. In case of electrical stimulation an electrode is either embedded in the cell or placed in contact with it. This limits the number of cells that can be excited by the number of electrodes. Optical stimulation can achieve similar spatial and temporal specificity with no contact, in a wide field manner which enables precise control in neuronal studies.

4.4.1 Optogenetics

Recently, visible light-assisted activation of selected neuronal group has been made possible with high temporal precision by introducing a light-activated molecular channel: channelrhodopsin-2 (ChR2) [93-96]. Currently, use of optogenetic sensitization of retinal cells combined with photo-activation has potential as an alternative to retinal implants that would have required large density of electrodes for high visual resolution in case of

loss of vision by photodegenerative diseases such as Retinitis pigmentosa (RP) [97-100]. In addition to higher (single-cell level) resolution, optogenetics has several advantages over electrical stimulation such as cellular specificity (e.g., residual cones, bipolar or ganglion cells) and noninvasiveness. The existence of channelrhodopsins, sensitive to narrow-bands of light, makes it possible to perform combinatorial experiments[101], in which the activity of several populations of cells (each expressing a different opsin) can be manipulated simultaneously by spectrally separated light. Narrow-band (blue) light sources have been used by us and others for vision restoration in blind mice model either by nonspecific stimulation of retina [102] or in a promoter-specific manner including Thy1 for retinal ganglion cells [103-107], mGluR6 targeting ON bipolar cells [108,109]. However, use of opsins with narrow-band spectral sensitivity requires light level orders of magnitude higher than the ambient light levels encountered by a human eye.

Therefore, narrow-band spectrally sensitive opsins require active stimulation by blue laser or LED [110,111] having intensity much higher than ambient light. However, boosting up light intensity to high enough levels to activate narrow-band opsin-expressing cells, especially for chronic stimulation, may substantially damage the residual light-sensing function that might exist in the diseased or impaired retina.

In order to allow (ambient) white-light based stimulation, we utilized use of opsin having broad spectral excitability in the entire visible spectrum (400-650 nm). This will allow higher sensitivity of opsin sensitized neurons to ambient white light, and therefore, significantly lower activation-threshold in contrast to conventional approach of narrow-band, intense, blue-light based active-stimulation. The development of red-shifted variant of channelrhodopsin[112], ReaChR has benefits of less photo-damage and enhanced penetration depth over the blue/green activable opsins. In addition to red excitability, ReaChR provides spectral excitation in other visible (blue and green) wavelengths. Here,

we report use of broad spectral excitation (white light) for optogenetic stimulation of ReaChR-sensitized cells. We observed robust ReaChR excitation with white light offering higher photocurrents compared to spectrally-filtered narrow-band light stimulation. The broad-band excitation of opsins will lead to better stimulation of retina because this technology permits efficient use of ambient light for vision restoration. The work discussed in this section has been published in Optics Letters, by Satpathy *et al*[113], and has been reprinted with permission from the publishers**.**

4.4.1.2 Methods

Cell culture**:** HEK 293 cells were transfected with ReaChR construct, cloned into pcDNA3.1 neo (LifeTechnologies Inc.). After transfection, the HEK293 cells were cultured at approximately 6 Å~ 106 cells per petridishes and maintained in DMEM with 10% fetal bovine serum, 0.2 mg/mL streptomycin, and 200 U/mL penicillin. The cultures were maintained at 37^0C in a 5% CO_2 humidified atmosphere. Visualizing the fluorescence under suitable illumination identified Transgene expressing cells. The cells not expressing in the same dish were considered as control. For generating light activation, cells were loaded with all-trans retinal (ATR, 1 µM) for at least 6 hours before doing the experiment.

Optogenetic stimulation: The wide-band white light from the microscope illumination source (halogen lamp) was used for optogenetic stimulation. A shutter (S) controlled the exposure (pulse) duration and current-controller was used to control the light intensity. In order to measure the spectrum of the filtered narrow-band light, a spectrometer (Ocean Optics Inc) was used. The function generator was synchronized to the *in-vitro* and *in-vivo* electrophysiology recording system (Molecular Devices). Light power at the fiber-tip was measured using a standard light power meter (PM 100D, Thorlabs Inc).

Patch-clamp recording setup: The opto-electrophysiology set up was developed on an Olympus inverted microscope platform using an amplifier system (Axon Multiclamp 700B, Molecular Devices Inc.). Parameters of the pipette puller were optimized in order to obtain desired borosilicate micropipettes of resistance from 3 to 5 MΩ for whole-cell patch clamp. The micropipette was filled with a solution containing (in mM) 130 K-Gluoconate, 7 KCl, 2 NaCl, 1 $MgCl_2$, 0.4 EGTA, 10 HEPES, 2 ATP-Mg, 0.3 GTP-Tris and 20 sucrose. The electrode was mounted on a XYZ motorized micromanipulator (Newport Inc.). The standard extracellular solution containing (in mM): 150 NaCl, 10 Glucose, 5 KCl, 2 $CaCl_2$, 1 $MgCl_2$ was buffered with 10 mM HEPES (pH 7.3). The output from the amplifier was digitized using Digidata (Molecular devices). For electrophysiological recording, the hardware was interfaced with patch-clamp software (pClamp, Molecular Devices). Electrical recordings were performed at a holding potential of -60mV at room temperature (20-24ºC). For activation of ChR2-expressing cells, the optogenetic stimulation beam was delivered by the condenser near the desired cell being patch-clamped. For generating and controlling pulses of light, the electromechanical shutter in the light path was interfaced with a PC. TTL pulses of desired frequency were generated using Digidata card in order to generate required pulses for activation. For electrophysiological measurements subsequent to optical activation, the shutter was synchronized with the patch clamp recording electrode. The whole system was electrically isolated by means of a Faraday cage that was placed around the setup. pClamp software was used for data analysis.

4.4.1.3 Results

Broad band light was successfully used to stimulate cellular activity in HEK293 cells, and resulted in better response as compared to narrowband light. As compared to 200 nm bandwidth of the white light, the spectrally-filtered narrow-band (red, green, and blue)

lights have bandwidth of 10 nm. For evaluating the effect of light bandwidth on activation of HEK293 cells expressing ReaChR, inward currents generated by light having different spectral profiles were recorded by patch clamp. Figure 4.8 shows the representative light-induced inward current in a ReaChR-expressing HEK293 cell upon illumination of various spectral stimulations and broadband white light (pulse width: 100 ms) at different white light intensities. HEK293 cells sensitized with ReaChR showed an order of magnitude higher excitability with white light as compared to the spectrally filtered light components (blue, green, or red). To compare the intensity-dependent peak current, the ReaChR-expressing cells were exposed to pulses (100 ms) of light (broadband or narrowband) with incident white light intensity ranging from 0.002 mW/mm^2 (0.18×10^{14} photons/ mm^{-2} s^{-1}) to 0.784 mW/mm^2 (72×10^{14} photons/ mm^{-2} s^{-1}), and the variation of the inward current responses were measured [Fig. 4.8 (b)]. For the case of white light stimulation (intensity of 0 .7842 mW/mm^2 at cell membrane), the measured current was ~80 pA, which reduced to <15 pA when filter (red/blue/green) was used.

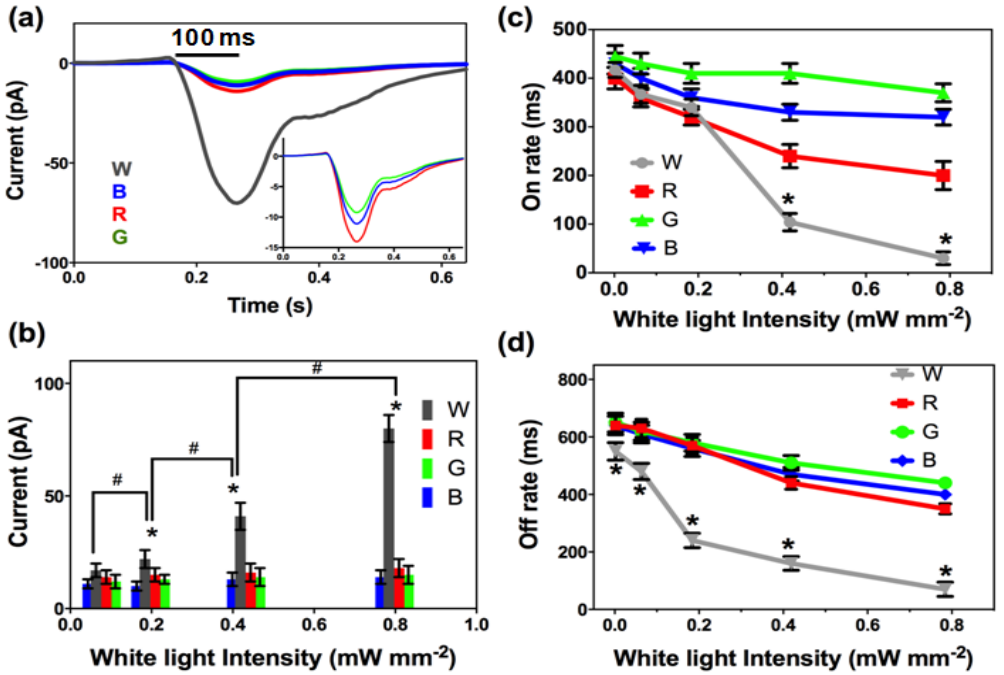

Figure 4.8: Quantitative comparison between broad-band and narrow-band optogenetic activation. Representative light-induced inward current in a ReaChR-expressing HEK cell upon illumination of (a) broad-band white light, and spectrally-filtered narrow-band blue, green and red light. Inset: Zoomed current profile for spectrally-filtered narrow-band blue, green and red light (pulse width: 100 ms). (b) Measured inward peak-current in ReaChR-HEK cell upon light stimulation with different spectral profiles at varied intensity levels. (c) Channel-on and (d) channel-off rate for ReaChR-HEK cell upon light stimulation with different spectral profiles and intensity levels. N=10 for each light wavelength and intensity. Average ± S.D. *p<0.01 between white and others. #p<0.01.

With decrease in white light intensity, the inward current decreased [Fig. 3(b)]. To compare stimulation efficacy by different spectral profiles, we define intensity spectral density as intensity divided by band width of the light spectrum. For intensity

spectral density of 0 .004 mW⁄mm^{2}nm, while white light elicited inward current of 80 $\pm$ 6 pA, the blue light induced current was 13 $\pm$ 2 pA. Statistically significant differences between inward peak current generated by white light and narrow-band stimulation were observed for intensities ≥ 0 .2 mW/mm^{2}nm.

To quantitatively compare the intensity-dependent channel-kinetics of ReaChR-sensitized cellular activation by optogenetic stimulation, the opsin-expressing cells were exposed to pulses (100 ms) of light (broadband or narrowband) with incident white light intensity ranging from 0.002 to 0.784 mW/mm^{2}nm, and the variation of the inward current responses were measured. Figures 4.8(c) and 4.8(d), respectively, show the light-activated ReaChR channel on and off rate at different light intensity levels. The onset response was found to be slow at lower intensities. With increase in light intensity, both the on and offrate decreased for all types of spectral stimulations. However, for white-light stimulation, the on and off-rate decreased more rapidly than for the spectrally filtered lights (i.e., red, green, blue). In case of white light stimulation, the channel on time decreased from 417ms (for low intensity: 0.002 mW/mm^{2}nm) to 30 ms with increasing light intensity (0.784 mW/mm^{2}nm). Similarly, the channel off-time decreased from 550 ms (at 0.002 mW/mm^{2}nm) to 70 ms at 0 .784 mW/mm^{2}nm (Fig. 4.8(d)). Though ReaChR has slower off-rate, the broad activation spectrum of ReaChR as compared to other opsins will allow utilization of more photon flux from the ambient light, thus improving the kinetics.

The motivation in using the ReaChR-opsin is to enable ambient white-light-based restoration of vision in case of photodegenerative diseases. As compared to HEK293 cells, the white light is expected to generate larger photocurrent in ReaChR-expressing RGCs owing to their larger size. By utilizing the whole visible spectrum, we expect that ambient-light can stimulate the ReaChR-sensitized RGCs to generate action potential.

This will eliminate the use of active stimulation device for restoration of vision, and is expected to provide higher resolution. The success of the proposed stimulation will enable a minimally invasive method for restoration of vision and pave the way for optogenetic treatment of photodegenerative diseases. The strategy of using ambient light could play a critical role in technology shift for vision restoration.

4.4.2 FS NIR stimulation

Neurons can be reliably targeted and focally stimulated in a non-contact manner using NIR ultrafast laser beam. While the actual mechanism responsible for initiating the cellular firing has not been understood since this method has not been studied extensively, a few theories have been suggested. During the short ms-exposure, multiphoton effects are known to occur, resulting in transient optoporation of the cell membrane, which allows extracellular Calcium into the cytoplasm because of the concentration gradient. A 'microtsunami' caused by the microcavitation bubble could also be a possible pathway for the Calcium wave. A shear flow produced by the microcavitation bubble provides mechanical stress onto every single cell to activate the release of Calcium within the cells[114]. To demonstrate neural activity being initiated by fs stimulation, we stimulate a network of rat cortical neurons and record the electrical activity with whole cell patch clamp.

4.4.2.1 Methods and materials

The neuronal cell culture was prepared the same way as detailed in section 4.2.1.1 and the patch clamp setup was the same detailed in section 4.4.1.2.

Optical setup:

The setup consists of a tunable (690 - 1040 nm) Ti:Sapphire laser (Newport Spectra-Physics, Inc.) with a repetition rate of 80 MHz and pulse width ~100 fs), coupled to an inverted microscope, which is used to produce a pulsed beam which is directed

toward the sample after passing through a beam expander by a dichroic mirror (DM1). A mechanical Uniblitz shutter in this optical path controls the duration of macro pulses being delivered to the sample. A second dichroic mirror DM2 was used to reflect the fluorescence excitation light from the mercury lamp along the same path as the fs laser, for fluorescence imaging of the sample when required. A camera is added into the optical path by introducing another dichroic mirror (DM3) to image the sample. The FS laser is operated at 800 nm and short bursts (10 ms) of pulsed are used to excite a neuron. The beam is aligned well to ensure a circular, Gaussian beam for a tight focus.

Patch clamp electrophysiology was used to record electrical activity before (control) and after fs stimulation from the same neuron that is being stimulated, and in a separate experiment, from a neighboring neuron that is connected to the one being stimulated.

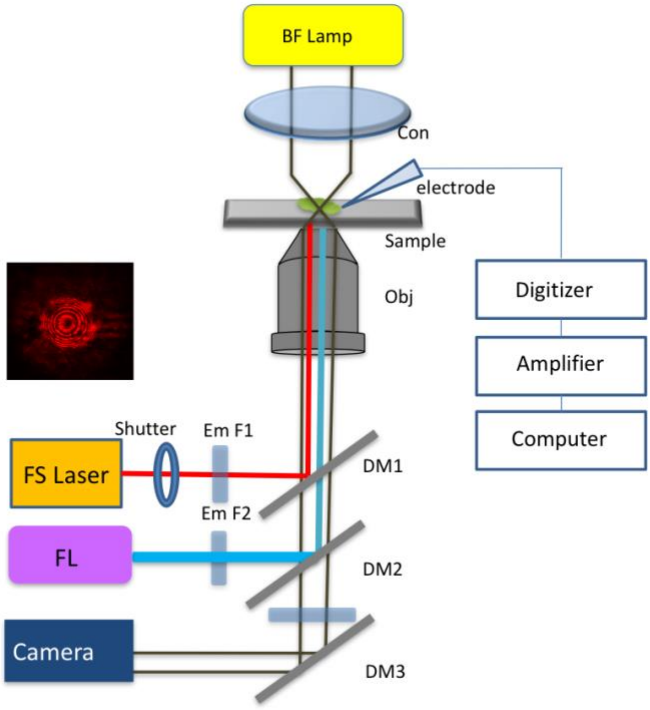

Figure 4.9: Optical setup for femtosecond laser stimulation of neurons. BF Lamp- Bright Field Lamp, Con- Condenser, Obj- Objective, Em F1- Emission Filter 1, Em F2- Emission Filter 2, FL- Fluorescence Lamp, DM1- Dichroic Mirror 1, DM2- Dichroic Mirror 2, DM3- Dichroic Mirror 3. Inset- Laser beam as seen on the camera at a low exposure.

4.4.2.2 Results

Electrical activity was recorded before and after the fs stimulation by whole cell patch clamp recording. There was an increased rate of neural firing after the fs stimulation. The recorded activity is summarized in the figures below. Figure 4.10 (A) shows the typical electrical recording of neuronal activity from a neuron before fs stimulation. Each sweep is 2.2 seconds long and are stacked atop to display more data. No firings are observed. Figure 4.10 (B) and Figure 4.10 (C) show the image of the

neurons being studied. The red lightning bolt represents the laser stimulation and the blue triangle represents the position of the electrode. In Figure 4.10 (B) the same neuron is being stimulated and recorded, whereas Figure 4.10 (C) shows one neuron being stimulated, and activity from a neighboring neuron attached to it is recorded.

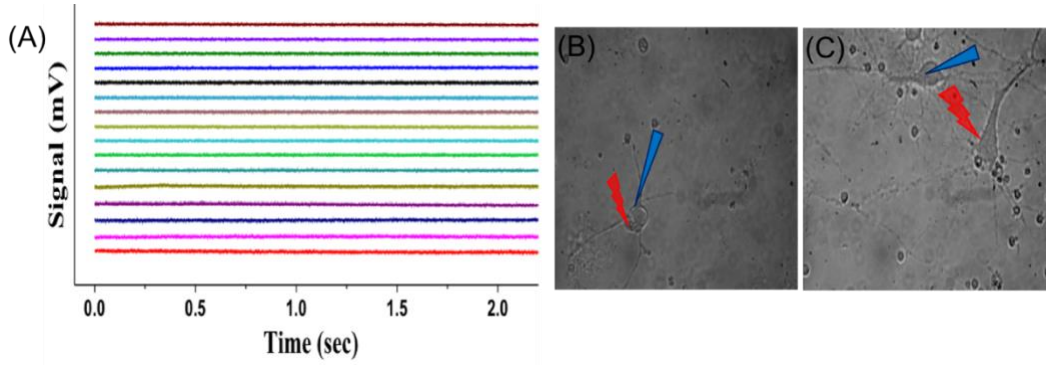

Figure 4.10: (A) Electrical activity recorded from a neuron before fs stimulation (control). (B) Image of the neuron being stimulated and patched. The red lightning bolt represents the laser stimulation and the blue triangle represents the position of the electrode. (C) NIR stimulated neuron, a neighboring neuron attached to it that is being recorded.

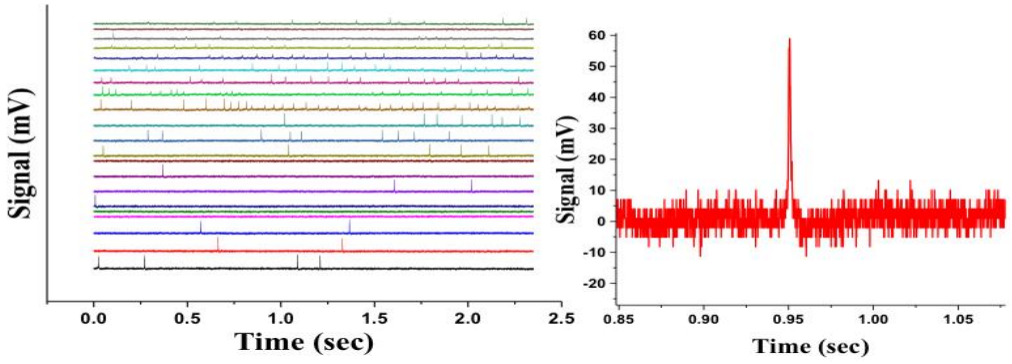

Figure 4.11: Electrical activity recorded from a neuron after fs stimulation. (right) Zoomed in voltage recording of a single action potential firing.

After fs stimulation, the neural activity increases in the neuron being stimulated, as is seen in Fig 4.10. Surprisingly, when a neighboring neuron that is synaptically attached to the neuron being stimulated is patched, we can not only see an increase in neural firing, but the increase is noticeably more significant than observed in the neuron being stimulated. This is shown in Fig 4.11, and an inset shows a single action potential.

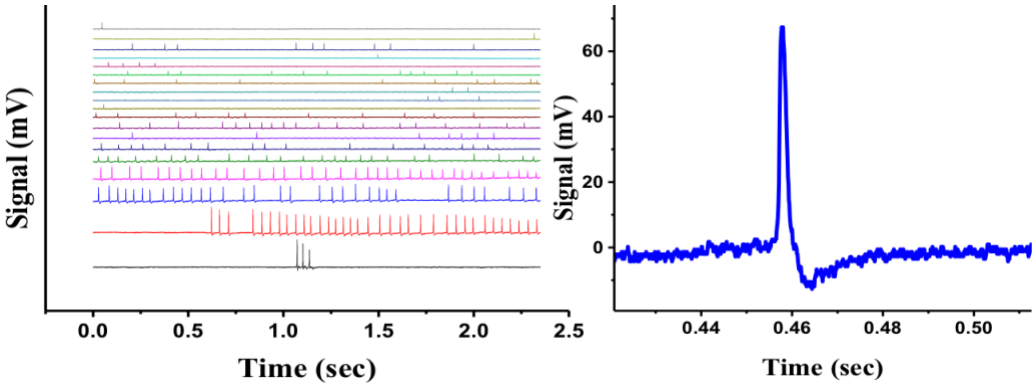

Figure 4.12: Electrical activity recorded from a neuron after stimulating a neighboring, synaptically attached neuron is stimulated by fs stimulation. (right) Zoomed in voltage recording of a single action potential firing.

While this phenomenon demands a more thorough, detailed and extensive study on it, these results do prove that NIR fs laser stimulation can be used to stimulate neural firing in a noncontact and spatially specific manner. This method merits detailed research as it promises to do so without the use of extaneous molecules, and in a wavelength corresponding to the optical window, which ensures low absorption, deeper penetration and low damage to cells and tissue.

4.5 Optical detection of optogenetically stimulated activity

In order to better sync the stimulation and optical detection of action potential, it is necessary to use a temporally specific means of stimulation, like electrical or optogenetic stimulation. Electrical stimulation with electrodes can't be used in the current setp with the sandwich cell housing device, as it requires insertion of electrodes, or the placement of gold electrodes directly in contact with the cells (similar to MEA). Instead, Optogenetic stimulation can be used to sync the neural firing to a frequency corresponding to that of the stimulation. Being able to single out individual action potentials and their equivalent optical recordings will help us distinguish the temporal signature of the opto-mechanical signaling. The features of each individual optical pulse might be indicative of the various characteristics of the causal action potential itself. That would imply that there is a significant amount of information encoded in the optical signal in terms of features like its temporal width, oscillation frequency and cycles, amplitude, shape/signature. This can provide information beyond just the membrane voltage.

In case of HEK cells, it was observed that the intracellular current corresponds precisely to the presence and timing of the stimulation. However, that is not observed in case of optogenetic stimulation of transgenic mice neurons. It appears that in case of networked neurons, stimulating a neuron at a particular frequency helps sync up the network to fire at that frequency. Repeating the experiment multiple times with different sets of optogenetically activable neurons with high 'n' number will increase the confidence and reliability of the optogenetic stimulation-neural firing relationship. Unfortunately, extracting and maintaining neuron cultures from transgenic mice is a lengthy and difficult process. The lead time between two batches of extracted cultures is often in the ballpark of 90 days, and there are a lot of variables governing the health and mortality of these cultures, and the slightest deviation from ideal conditions can kill the

entire batch. After a complicated extraction process, these cultures need to be incubated at precise temperature and humidity conditions for about a week. 4 days into the culture, Cre needs to be added in the cellular medium for the neurons to express the opsin. This step is necessary, but Cre is also toxic to the cels, which leads to cell death and fragmentation in some cases. After the cultures have been incubated for a week, they are transported to the lab for the experiment, which can also induce cell mortality and stress. Due to this stress, many cultures fail to survive, or start apoptosing. Owing to these difficulties and the time constraint not many batches were obtained for the experiment. Due to the low 'n' number, not enough data could be collected to ascertain the features of the optical signal recorded.

4.5.1 Materials and methods

All experimental procedures were conducted according to UT Arlington and UT Southwestern Medical Center Institutional Animal Care and Use Committee approved protocol. Cortical neurons were isolated from P-1 transgenic mice expressing Channelrhodopsin-2 (ChR2) after cortical tissues were dissected, cleaned (meningeal layer), enzymatically dissociated (500μL 20U Papain in 250 ml HBSS) for 20 minutes at 37 ^{0}C. A density of 120,000/ml suspended in culture media consisting of 50 mL Neurobasal medium A supplemented B-27 (with added vitamin A) 1 mL, Pen/strep 0.5 mL, 0.5 mL 200 mM L-Glutamine, at 37 ^{0}C was seeded on Poly-D-lysine (PDL, 0.01%, Sigma) coated sandwich devices (discussed in chapter 2). These cultures are grown for a week, with media changed every 2 days until the neuronal networks are apparent. Four days after seeding, the culture is treated with Adeno-Cre to ensure expression of opsin.

Optical setup:

The optical setup is the same as the one used in the Low Coherence NIR Interferometry setup discussed in Chapter 2 and 3. In addition, a DPSSL drivel blue laser

(473 nm) was coupled into the optical path with a Dichroic Mirror in the 30 mm cage path to couple the 860 nm probing beam and the 473 nm stimulation beam into the microscope objective. The Digitizer from the patch Clamp setup was used to trigger the laser on and off periodically, in sweeps that are repeated for a fixed number of times. In this case, there are three laser pulses of 50 ms width each in one sweep, repeated 20 times in a run, which roughly calculates to be 60 pulses in a minute. Control experiments were done by collecting optical signals from a single neuron in a network before optogenetic stimulation. Then optical data is collected from the same neuron after the blue laser stimulation.

4.5.2 Results and discussions

The optical signal displayed in Figure 4.13 was collected from the subcellular region of a neuron at the junction of the soma and the axon, and shows a minute of optical signal recording without laser stimulation (control) followed by 4 minutes of recording with laser stimulation. Change in optical path length are noticeable with (blue) and without (green) optical stimulation, and these changes are much higher when the neuron is stimulated with the laser. While the maximum amplitude of OPD change without laser stimulation is 0.25 nm, the maximum amplitude with the blue laser stimulation is 0.51 nm.

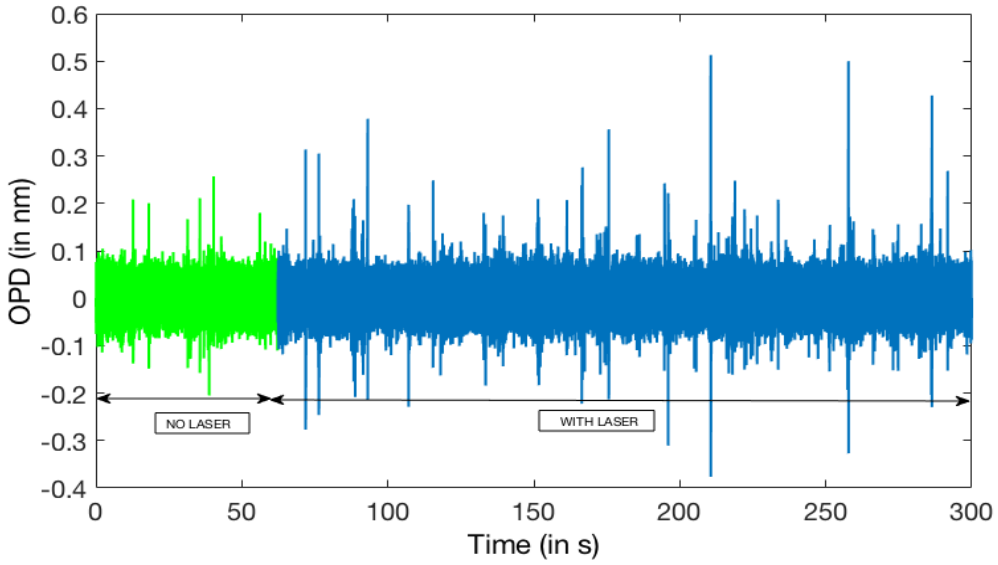

Figure 4.13: Optical signal recorded from the neuron soma-axon junction without (green) and with (blue) laser stimulation.

It is observed that these are distinct optical pulses, and even when these might appear to be bunched into a set of oscillations, individual spikes can often be discerned on zooming in, and these spikes are not led or trailed by gradually reducing oscillations, but stand alone. Zoomed in regions of the optical signal are displayed in Fig. 4.14 to display this.

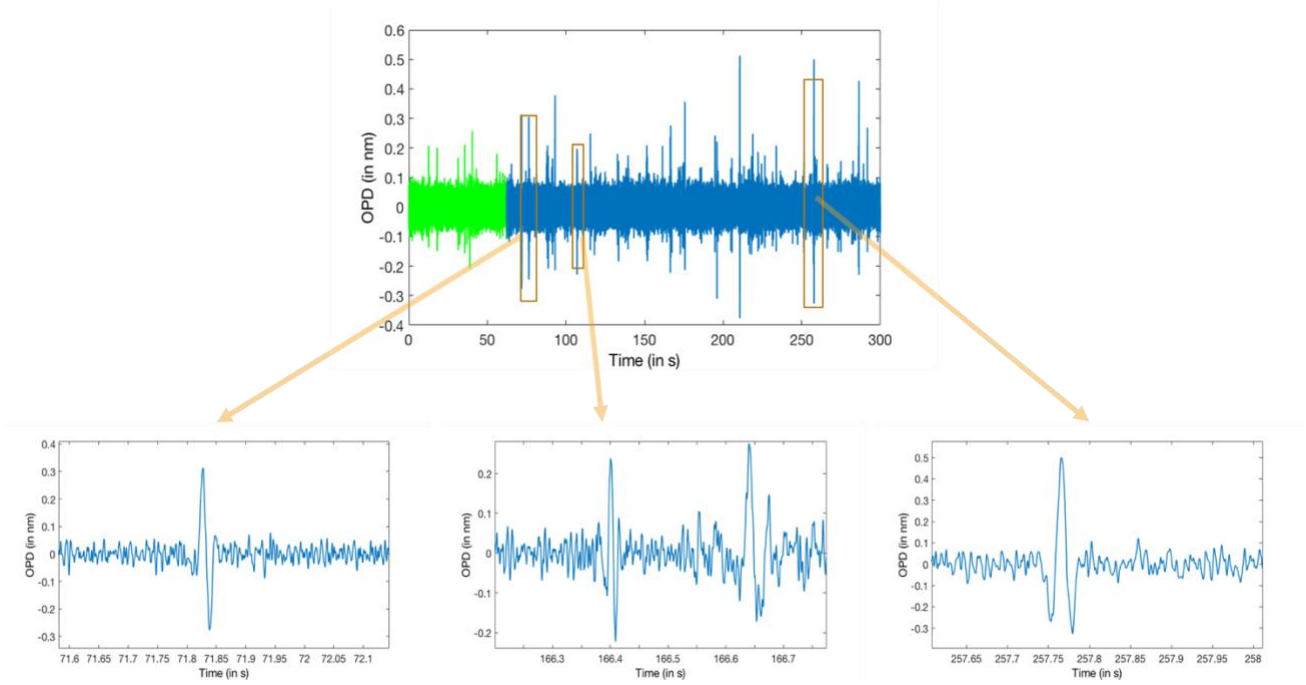

Figure 4.14: Zoomed in regions of the recorded optical signal are displayed. The region zoomed is represented by the yellow rectangle.

Interestingly, individual optical spikes mostly seem to have a common temporal signature, closely resembling the actual membrane voltage change during action potential, with a distinct initial rise to a peak, followed by a drop to the baseline, continuing the change in OPD in the negative direction, before reaching a minimum and then going back to the baseline, resembling one complete oscillation of a sinusoidal wave. In most of the cases the positive lobe appears first, followed by the negative lobe, although there are a few exceptions. Some of these optical spikes are shown in Fig 4.15. the timescales of these spikes are much more consistently within a narrow range, and lie within 10-20 ms. This also matches closely with the timescale of an electrical action potential which lasts for 7-10 ms.

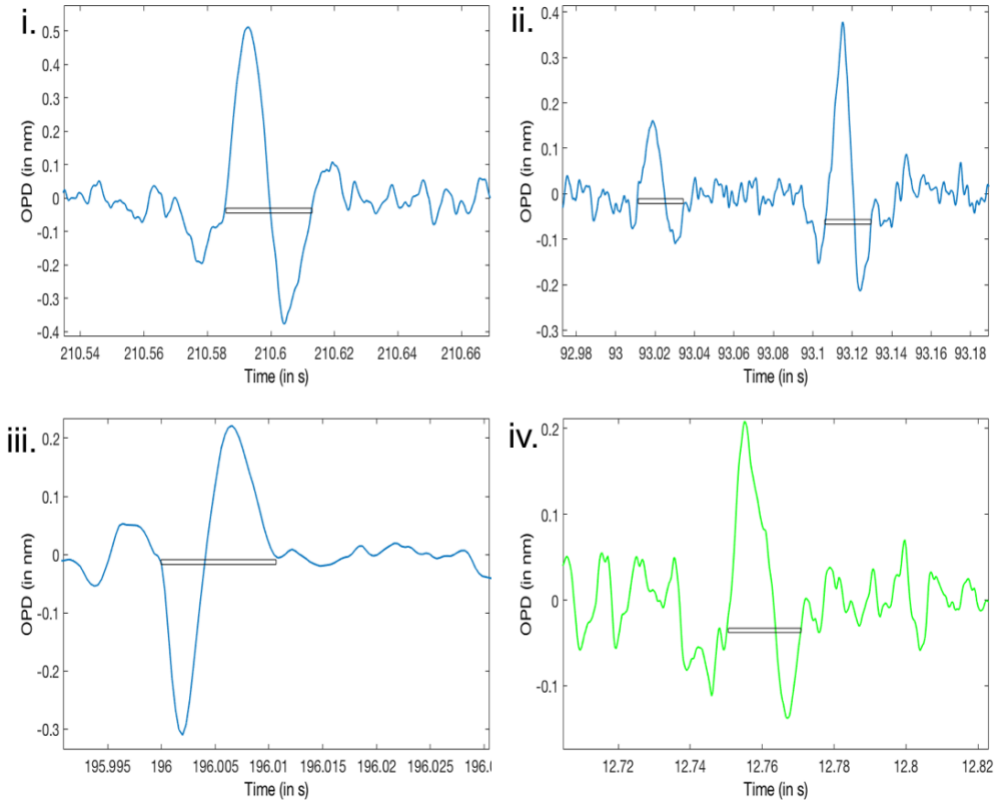

Figure 4.15: Single optical pulses displaying positive and negative lobes. (i)-(iii) are taken from the signal recorded after laser stimulation, while (iv) is taken from signal recorded before stimulation.

The action potential itself does not change much depending on the stimulation used, so it is possible that these distinct changes are more noticeable in the soma-axon junction as it is an active area, and instead of looking at only a part of the membrane, the beam actually covers the narrow region, which sees more opto-mechanical change per area because of the propagation of the action potential.

This implies that not only is this method a very viable alternative to electrophysiology, it can also be used to collect signals from subcellular regions,

effectively helping us map the electrical and opto-mechanical changes with action potential propagation, and discover more about the role of individual regions of the neuron body in action potential generation and propagation.

4.5. Conclusion

In this chapter, we were able to demonstrate individual techniques that can be used to design and create a neural circuit optically. By using optical trapping, individual cells can be placed in desired positions to create a planned network. It can be used to have a premeditated co-culture to better understand the behavior of the individual components in presence of other biological components. With optoporation, it is possible to introduce other controlling factors like opsins and dyes to cells in a noncontact, sterile, highly specific manner which can be used to give multiple inputs to the circuit without compromising the indigenous environment of the culture. This can also be used to selectively transfect some of the neurons in the circuit to be optogenetically activable, which is similar to introducing a switch in an electrical circuit. Optical stimulation can be used to stimulate neural activity with high spatial and temporal specificity. Optogenetics has been widely studied and implemented, and allows the option of selectively stimulate and inhibit firing in neurons. In addition, we have also shown stimulation of neural activity with pulsed fs laser stimulation. In addition, we demonstrated the optical detection of action potential stimulated by the optogenetic stimulation. Clear optical spikes were observed, with a distinct signature, and a timescale of 10-20 ms. Optical stimulation and detection performed together can help us better understand the fundamental mechanism of electromechanical coupling as precise, one to one relationship between stimulation input and action potential output can be studied without the need for an electrode.

All these techniques can be applied together to create a neural circuit that can be studied with a variety of inputs to decode the transfer function of the circuit. Such a study

needs to be conducted in contamination free, sterile, controlled, noninvasive manner for extended period of time- which can be achieved by employing all optical techniques.

Chapter 5

Conclusion

We were able to detect action potential spikes in single mammalian neurons in a network in a label free, noninvasive manner optically by employing a Low Coherence NIR interferometry method, without the need for signal averaging. With good spatial (subcellular) and sub-millisecond (160 μs) temporal resolution, this method can be used in complement to electrophysiology and can also be used to detect neural firing in cases where electrophysiology cannot be used. Individual spikes were observed and were compared with the electrical recordings of action potential. The ability to observe sub cellular regions effectively help us map the electrical and opto-mechanical changes associated with action potential propagation. In addition, other optical techniques were demonstrated that can help design a neural circuit to conduct controlled, extended studies on these in-vitro cultures with a variety of inputs to understand the input-output relationship for individual as well as a group of neurons. Decoding the transfer function in these cultures can help decode the behavior of more complicated circuits, like the networks present in-vivo. The techniques can also be used to observe and understand disease states, causes, and reactions to various treatment methodologies.

Our interferometry based optical detection method serves as a paradigm for developing an alternative non-invasive tool for studying electrical activity in neuronal systems from a single cell to complex networks. A 2D version of our prototype instrument will significantly increase the throughput by simultaneously recording optical signals from multiple neurons. Implementation of 2D interferometry can be achieved either by raster scanning the probe beam over the sample or acquiring hyperspectral images using a swept broadband source in a microscopy setup. This optical detection technique also benefits from the fact that signals can be selectively collected from specific regions of

neuronal circuit, e.g. axon, synaptic junction, dendrite, which is technically challenging using conventional glass microelectrode electrophysiology and thus it can be complementary to electrical recording. 2D interferometry would also be a viable alternative to optical methods using fluorescent imaging sharing advantages such as high throughput, noninvasive and noncontact detection, but without having to resort to averaging, or using high exposure time to mitigate the low SNR of the fluorescent probes. It also eliminates the drawback of using exogenous molecules that may interfere with normal physiological functioning of individual excitable cells and as a consequence, the network properties. The described technique is uniquely suited for in-vitro applications such as screening of neuro-therapeutic drugs, studying functional recovery of injured neurons and disrupted neuronal networks, and influence of electrical and magnetic field on neuronal activity. Moreover, rather than an epiphenomenon, recent studies have raised the intriguing possibility of a potential coupling between propagating mechanical wave and AP. Mechanical wave energy could feedback into the propagating AP in a coupled electromechanical system. This is potentially a very important part of the basic functioning of neurons and electrochemical signaling which plays a vital part of the physiology. Understanding this is basic to understanding the brain and until now, no studies have studied these effects in depth in neurons. Lack of information about the non-electrical phenomena associated with action potential could deter our understanding of the neural system, especially if it is the factor determining the propagation of the electrochemical signaling. Without understanding the electromechanical coupling, we cannot gain a complete knowledge of the brain.

To study the nonelectrical components and to verify the aforementioned hypothesis, we need a method that can measure these mechanical changes without hindering the natural functioning of neurons, which would imply no use of invasive techniques or

extrageneous molecules. Our label-free interferometric technique will be a uniquely suited for studying fundamental mechanism of electromechanical coupling and its implications in transmission of signals in neuronal networks

Appendix A

License and copyright of materials

Permission to use material from Subrata Batabyal, Sarmishtha Satpathy, Loan Bui, Young-Tae Kim, Samarendra Mohanty, Robert Bachoo, and Digant P. Davé, "Label-free optical detection of action potential in mammalian neurons," Biomed. Opt. Express 8, 3700-3713 (2017):

pubscopyright November 30, 2017 at 9:08 AM

To: Sarmishtha Satpathy pubscopyright

RE: Permission to use parts of authored article in my dissertation

Dear Sarmishtha Satpathy,

Thank you for contacting The Optical Society.

OSA retains copyright to the Open Access papers, including those published in our Open Access journals such as *Biomedical Optics Express*. If the article is available under the Creative Commons licensing or our new Open Access Publishing Agreement, that information will be displayed on the abstract page.

For the use of material from Subrata Batabyal, Sarmishtha Satpathy, Loan Bui, Young-Tae Kim, Samarendra Mohanty, Robert Bachoo, and Digant P. Davé, "Label-free optical detection of action potential in mammalian neurons," Biomed. Opt. Express 8, 3700-3713 (2017):

As long as the copyrighted material is included within the body, section or chapter, of the thesis, and is not posted separate from the thesis, OSA considers your requested use of its copyrighted materials to be permissible within the author rights granted in the Copyright Transfer Agreement submitted by the requester on acceptance for publication of his/her manuscript. If the entire article is being included, it is requested that the **Author Accepted** (or preprint) version be the version included within the thesis and that a complete citation of the original material be included in any publication. This permission assumes that the material was not reproduced from another source when published in the original publication.

The **Author Accepted** version is the preprint version of the article that was accepted for publication but not yet prepared and/or formatted by The Optical Society or its vendors.

While your publisher should be able to provide additional guidance, OSA prefers the below citation formats:

For citations in figure captions:

[Reprinted/Adapted] with permission from ref [x], [Publisher]. (with full citation in reference list)

For images without captions:

Journal Vol. #, first page (year published) An example: Biomed. Opt. Express 8, 3700 (2017)

Let me know if you have any questions.

Kind Regards,

Rebecca Robinson

Rebecca Robinson
November 30, 2017
Authorized Agent, The Optical Society

Permission to use material from Sarmishtha Satpathy, Subrata Batabyal, Kamal R. Dhakal, John Lin, Young-tae Kim, and Samarendra K. Mohanty, "Broad spectral excitation of opsin for enhanced stimulation of cells," Opt. Lett. 40, 2465-2468 (2015):

pubscopyright December 4, 2017 at 12:02 PM

To: Sarmishtha Satpathy, pubscopyright

RE: Permission to use parts of authored article in my dissertation

Dear Sarmishtha Satpathy,

Thank you for contacting The Optical Society.

For the use of material from Sarmishtha Satpathy, Subrata Batabyal, Kamal R. Dhakal, John Lin, Young-tae Kim, and Samarendra K. Mohanty, "Broad spectral excitation of opsin for enhanced stimulation of cells," Opt. Lett. 40, 2465-2468 (2015):

> As long as the copyrighted material is included within the body, section or chapter, of the thesis, and is not posted separate from the thesis, OSA considers your requested use of its copyrighted materials to be permissible within the author rights granted in the Copyright Transfer Agreement submitted by the requester on acceptance for publication of his/her manuscript. If the entire article is being included, it is requested that the **Author Accepted** (or preprint) version be the version included within the thesis and that a complete citation of the original material be included in any publication. This permission assumes that the material was not reproduced from another source when published in the original publication.

The **Author Accepted** version is the preprint version of the article that was accepted for publication but not yet prepared and/or formatted by The Optical Society or its vendors.

While your publisher should be able to provide additional guidance, OSA prefers the below citation formats:

> For citations in figure captions:
>
> [Reprinted/Adapted] with permission from ref [x], [Publisher]. (with full citation in reference list)
>
> For images without captions:
>
> Journal Vol. #, first page (year published) An example: Opt. Lett. 40, 2465 (2015)

Let me know if you have any questions.

Kind Regards,

Rebecca Robinson

Rebecca Robinson
December 4, 2017
Authorized Agent, The Optical Society

References

1 Herculano-Houzel, S. The human brain in numbers: a linearly scaled-up primate brain. *Front Hum Neurosci* **3**, 31, doi:10.3389/neuro.09.031.2009 (2009).

2 Albright, T. D., Jessell, T. M., Kandel, E. R. & Posner, M. I. Neural science: a century of progress and the mysteries that remain. *Neuron* **25 Suppl**, S1-55 (2000).

3 Yuste, R. From the neuron doctrine to neural networks. *Nat Rev Neurosci* **16**, 487-497, doi:10.1038/nrn3962 (2015).

4 Rees, G., Kreiman, G. & Koch, C. Neural correlates of consciousness in humans. *Nat Rev Neurosci* **3**, 261-270, doi:10.1038/nrn783 (2002).

5 Scanziani, M. & Hausser, M. Electrophysiology in the age of light. *Nature* **461**, 930-939, doi:10.1038/nature08540 (2009).

6 Sigworth, F. J. & Neher, E. Single Na+ channel currents observed in cultured rat muscle cells. *Nature* **287**, 447-449 (1980).

7 Hodgkin, A. L. & Huxley, A. F. Resting and action potentials in single nerve fibres. *J Physiol* **104**, 176-195 (1945).

8 Mueller, J. K. & Tyler, W. J. A quantitative overview of biophysical forces impinging on neural function. *Phys Biol* **11**, 051001, doi:10.1088/1478-3975/11/5/051001 (2014).

9 Spira, M. E. & Hai, A. Multi-electrode array technologies for neuroscience and cardiology. *Nat Nanotechnol* **8**, 83-94, doi:10.1038/nnano.2012.265 (2013).

10 Engel, A. K., Moll, C. K., Fried, I. & Ojemann, G. A. Invasive recordings from the human brain: clinical insights and beyond. *Nat Rev Neurosci* **6**, 35-47, doi:10.1038/nrn1585 (2005).

11 Dunlop, J., Bowlby, M., Peri, R., Vasilyev, D. & Arias, R. High-throughput electrophysiology: an emerging paradigm for ion-channel screening and physiology. *Nat Rev Drug Discov* **7**, 358-368, doi:10.1038/nrd2552 (2008).

12 Butovas, S. & Schwarz, C. Spatiotemporal effects of microstimulation in rat neocortex: a parametric study using multielectrode recordings. *J Neurophysiol* **90**, 3024-3039, doi:10.1152/jn.00245.2003 (2003).

13 Hales, C. M., Rolston, J. D. & Potter, S. M. How to culture, record and stimulate neuronal networks on micro-electrode arrays (MEAs). *J Vis Exp*, doi:10.3791/2056 (2010).

14 Ross, W. N. *et al.* Changes in absorption, fluorescence, dichroism, and Birefringence in stained giant axons: : optical measurement of membrane potential. *J Membr Biol* **33**, 141-183 (1977).

15 Hill, D. K. & Keynes, R. D. Opacity changes in stimulated nerve. *J Physiol* **108**, 278-281 (1949).

16 Perry, J. L., Ramachandran, N. K., Utama, B. & Hyser, J. M. Use of genetically-encoded calcium indicators for live cell calcium imaging and localization in virus-infected cells. *Methods* **90**, 28-38, doi:10.1016/j.ymeth.2015.09.004 (2015).
17 Horikawa, K. Recent progress in the development of genetically encoded Ca2+ indicators. *The Journal Of Medical Investigation* **62**, 25-28 (2015).
18 Looger, L. L. & Griesbeck, O. Genetically encoded neural activity indicators. *Curr Opin Neurobiol* **22**, 18-23, doi:10.1016/j.conb.2011.10.024 (2012).
19 Antic, S. D., Empson, R. M. & Knopfel, T. Voltage imaging to understand connections and functions of neuronal circuits. *J Neurophysiol* **116**, 135-152, doi:10.1152/jn.00226.2016 (2016).
20 Kralj, J. M., Douglass, A. D., Hochbaum, D. R., Maclaurin, D. & Cohen, A. E. Optical recording of action potentials in mammalian neurons using a microbial rhodopsin. *Nat Methods* **9**, 90-95, doi:10.1038/nmeth.1782 (2011).
21 Warden, M. R., Cardin, J. A. & Deisseroth, K. Optical neural interfaces. *Annu Rev Biomed Eng* **16**, 103-129, doi:10.1146/annurev-bioeng-071813-104733 (2014).
22 Hrvatin, S., Nagy, M. A. & Greenberg, M. E. Catching the Brain in the Act. *Cell* **165**, 1570-1571, doi:10.1016/j.cell.2016.06.008 (2016).
23 Cohen, L. B. Historical Overview and General Methods of Membrane Potential Imaging. 1-11, doi:10.1007/978-1-4419-6558-5_1 (2010).
24 Peterka, D. S., Takahashi, H. & Yuste, R. Imaging voltage in neurons. *Neuron* **69**, 9-21, doi:10.1016/j.neuron.2010.12.010 (2011).
25 St-Pierre, F., Chavarha, M. & Lin, M. Z. Designs and sensing mechanisms of genetically encoded fluorescent voltage indicators. *Curr Opin Chem Biol* **27**, 31-38, doi:10.1016/j.cbpa.2015.05.003 (2015).
26 Hill, D. K. The effect of stimulation on the opacity of a crustacean nerve trunk and its relation to fibre diameter by *J. Physiol.* **III**, 283-303 (1950).
27 B. Frankenhaeuser, A. L. H. The After-Effects Of Impulses In The Giant Nerve Fibres Of Loligo. *J. Physiol.* **131**, 341-376 (1956).
28 L. B. Cohen, R. D. Keynes & Hille, B. Light Scattering And Birefringence Changes During Nerve Activity. *Nature* **218**, 438 (1968).
29 I. Tasaki, A. W., R. Sandlin, L. Carnay. Changes In Fluorescence, Turbidity, And Birefringence Associated With Nerve Excitation. *Proceedings of the National Academy of Sciences of the United States of America* **61** (1968).
30 R. A. Stepnoski, A. L., F. Raccuia-Behling, G. E. Blonder, R. E. Slusher, D. Kleinfeld. Noninvasive detection of changes in membrane potential in cultured neurons by light scattering. *Proceedings of the National Academy of Sciences* **88**, 9382-9386 (1991).
31 Watanabe, A. Change in optical activity of a lobster nerve associated with excitation. *J Physiol* **389**, 223-253 (1987).
32 Christopher Fang-Yen, M. S. F. *Intrinsic optical signals in neural tissues measurements, mechanisms, and applications*. Vol. 963 219-235 (ACS Symposium Series, 2007).

33 Schei, J. L., McCluskey, M. D., Foust, A. J., Yao, X. C. & Rector, D. M. Action potential propagation imaged with high temporal resolution near-infrared video microscopy and polarized light. *Neuroimage* **40**, 1034-1043, doi:10.1016/j.neuroimage.2007.12.055 (2008).
34 Benedikt W. Graf, T. S. R., Han-Jo Ko, Stephen A. Boppart. Detecting intrinsic scattering changes correlated to neuron action potentials using optical coherence imaging *Optics Express* **17**, 13447-13457 (2009).
35 Islam, M. S. *et al.* A common-path optical coherence tomography based electrode for structural imaging of nerves and recording of action potentials. **8565**, 856565, doi:10.1117/12.2005095 (2013).
36 Marshall, J. D. & Schnitzer, M. J. Optical strategies for sensing neuronal voltage using quantum dots and other semiconductor nanocrystals. *ACS Nano* **7**, 4601-4609, doi:10.1021/nn401410k (2013).
37 Zhang, J., Atay, T. & Nurmikko, A. V. Optical detection of brain cell activity using plasmonic gold nanoparticles. *Nano Lett* **9**, 519-524, doi:10.1021/nl801891q (2009).
38 Hall, L. T. *et al.* High spatial and temporal resolution wide-field imaging of neuron activity using quantum NV-diamond. *Sci Rep* **2**, 401, doi:10.1038/srep00401 (2012).
39 Shin Ae Kim, K. M. B., Jonghwan Lee, Jung Hoon Kim, Dong-Ghi Albert Kim, & Hyoungwon Baac, M. L. S., and Sung June Kim. Optical measurement of neural activity using surface plasmon resonance. *OPTICS LETTERS* **33**, 914-916 (2008).
40 Oh, S. *et al.* Label-free imaging of membrane potential using membrane electromotility. *Biophys J* **103**, 11-18, doi:10.1016/j.bpj.2012.05.020 (2012).
41 Liu, B. *et al.* Label-free spectroscopic detection of membrane potential using stimulated Raman scattering. *Applied Physics Letters* **106**, 173704, doi:10.1063/1.4919104 (2015).
42 Badreddine, A. H., Jordan, T. & Bigio, I. J. Real-time imaging of action potentials in nerves using changes in birefringence. *Biomed Opt Express* **7**, 1966-1973, doi:10.1364/BOE.7.001966 (2016).
43 Christopher Fang-Yen, M. C. C., H. Sebastian Seung, Ramachandra R. Dasari and Michael S. Feld. Noncontact measurement of nerve displacement during action potential with a dual-beam low-coherence interferometer. *Optics Letters* **29**, 2028-2030 (2004).
44 Mariya Lazebnik, D. L. M., Kurt Potgieter, Rhanor Gillette, Stephen A. Boppart. Functional optical coherence tomography for detecting neural activity through scattering changes. *Optics Letters* **28**, 1218-1220 (2003).
45 Taner Akkin, D. P. D., Thomas E. Milner, H. Grady Rylander III. Detection of neural activity using phase-sensitive optical low-coherence reflectometry. *OPTICS EXPRESS* **12**, 2377-2386 (2004).
46 Akkin, T., Landowne, D. & Sivaprakasam, A. Detection of Neural Action Potentials Using Optical Coherence Tomography: Intensity and Phase

Measurements with and without Dyes. *Front Neuroenergetics* **2**, doi:10.3389/fnene.2010.00022 (2010).
47 Gross, D., Loew, L. M. & Webb, W. W. Optical imaging of cell membrane potential changes induced by applied electric fields. *Biophys J* **50**, 339-348, doi:10.1016/S0006-3495(86)83467-1 (1986).
48 J. F. Barry, M. J. T., J. M. Schloss, D. R. Glenn, Y. Song, M. D. Lukin, H. Park, R. L. Walsworth. Optical magnetic detection of single-neuron action potentials using quantum defects in diamond. *arXiv:1602.01056v1 [quant-ph]*.
49 Jensen, K. *et al.* Non-invasive detection of animal nerve impulses with an atomic magnetometer operating near quantum limited sensitivity. *Sci Rep* **6**, 29638, doi:10.1038/srep29638 (2016).
50 Dombeck, D. A., Blanchard-Desce, M. & Webb, W. W. Optical recording of action potentials with second-harmonic generation microscopy. *J Neurosci* **24**, 999-1003, doi:10.1523/JNEUROSCI.4840-03.2004 (2004).
51 Fercher, A. F., Mengedoht, K. & Werner, W. Eye-length measurement by interferometry with partially coherent light. *Opt Lett* **13**, 186-188 (1988).
52 Fercher, A. F., Hitzenberger, C. K., Kamp, G. & El-Zaiat, S. Y. Measurement of intraocular distances by backscattering spectral interferometry. *Optics communications* **117**, 43-48 (1995).
53 Leitgeb, R., Hitzenberger, C. & Fercher, A. F. Performance of fourier domain vs. time domain optical coherence tomography. *Optics express* **11**, 889-894 (2003).
54 De Boer, J. F. *et al.* Improved signal-to-noise ratio in spectral-domain compared with time-domain optical coherence tomography. *Optics letters* **28**, 2067-2069 (2003).
55 Podoleanu, A. G. & Jackson, D. A. Noise analysis of a combined optical coherence tomograph and a confocal scanning ophthalmoscope. *Appl Opt* **38**, 2116-2127 (1999).
56 Ha Usler, G. & Lindner, M. W. "Coherence radar" and "spectral radar"-new tools for dermatological diagnosis. *J Biomed Opt* **3**, 21-31, doi:10.1117/1.429899 (1998).
57 Vakhtin, A. B., Kane, D. J., Wood, W. R. & Peterson, K. A. Common-path interferometer for frequency-domain optical coherence tomography. *Appl Opt* **42**, 6953-6958 (2003).
58 Vakoc, B., Yun, S., de Boer, J., Tearney, G. & Bouma, B. Phase-resolved optical frequency domain imaging. *Opt Express* **13**, 5483-5493 (2005).
59 Izatt, J. A. & Choma, M. A. in *Optical Coherence Tomography: Technology and Applications* (eds Wolfgang Drexler & James G. Fujimoto) 47-72 (Springer Berlin Heidelberg, 2008).
60 de Boer, J. F. in *Optical Coherence Tomography: Technology and Applications* (eds Wolfgang Drexler & James G. Fujimoto) 147-175 (Springer Berlin Heidelberg, 2008).

61 Mandel, L. & Wolf, E. The measures of bandwidth and coherence time in optics. *Proceedings of the Physical Society* **80**, 894 (1962).
62 Sorin, W. V. & Baney, D. M. A simple intensity noise reduction technique for optical low-coherence reflectometry. *IEEE Photonics Technology Letters* **4**, 1404-1406 (1992).
63 Liang, X., Liu, A., Lim, C., Ayi, T. & Yap, P. Determining refractive index of single living cell using an integrated microchip. *Sensors and Actuators A: Physical* **133**, 349-354 (2007).
64 Batabyal, S. *et al.* Label-free optical detection of action potential in mammalian neurons. *Biomedical optics express* **8**, 3700-3713 (2017).
65 Narahashi, T., Moore, J. W. & Scott, W. R. Tetrodotoxin Blockage of Sodium Conductance Increase in Lobster Giant Axons. *J Gen Physiol* **47**, 965-974 (1964).
66 Iwasa, K. & Tasaki, I. Mechanical Changes in Squid Giant-Axons Associated with Production of Action-Potentials. *Biochem Bioph Res Co* **95**, 1328-1331, doi:Doi 10.1016/0006-291x(80)91619-8 (1980).
67 Akkin, T., Davé, D. P., Milner, T. E. & Rylander Iii, H. G. Detection of neural activity using phase-sensitive optical low-coherence reflectometry. *Opt Express* **12**, 2377-2386, doi:10.1364/OPEX.12.002377 (2004).
68 El Hady, A. & Machta, B. B. Mechanical surface waves accompany action potential propagation. *Nat Commun* **6**, doi:Artn 6697

10.1038/Ncomms7697 (2015).
69 Heimburg, T. & Jackson, A. D. On the action potential as a propagating density pulse and the role of anesthetics. *Biophysical Reviews and Letters* **2**, 57-78 (2007).
70 Cohen, L. Changes in neuron structure during action potential propagation and synaptic transmission. *Physiol. Rev* **53**, 373-418 (1973).
71 Tasaki, I. & Byrne, P. M. Volume expansion of nonmyelinated nerve fibers during impulse conduction. *Biophysical journal* **57**, 633-635, doi:10.1016/S0006-3495(90)82580-7 (1990).
72 Oh, S. *et al.* Label-Free Imaging of Membrane Potential Using Membrane Electromotility. *Biophysical journal* **103**, 11-18, doi:10.1016/j.bpj.2012.05.020 (2012).
73 Sassaroli, E. & Vykhodtseva, N. Acoustic neuromodulation from a basic science prospective. *J Ther Ultrasound* **4**, doi:UNSP 17

10.1186/s40349-016-0061-z (2016).
74 Gross, D., Williams, W. S. & Connor, J. A. Theory of Electromechanical Effects in Nerve. *Cell Mol Neurobiol* **3**, 89-111, doi:Doi 10.1007/Bf00735275 (1983).
75 Budvytyte, R. *et al.* Solitary Electromechanical Pulses in Lobster Neurons. *Biophysical journal* **110**, 150a-150a (2016).
76 Zhang, P. C., Keleshian, A. M. & Sachs, F. Voltage-induced membrane movement. *Nature* **413**, 428-432, doi:Doi 10.1038/35096578 (2001).

77 Fang-Yen, C., Chu, M. C., Seung, H. S., Dasari, R. R. & Feld, M. S. Noncontact measurement of nerve displacement during action potential with a dual-beam low-coherence interferometer. *Optics letters* **29**, 2028-2030 (2004).
78 Mueller, J. K. & Tyler, W. J. A quantitative overview of biophysical forces impinging on neural function. *Phys Biol* **11**, doi:Artn 051001

10.1088/1478-3975/11/5/051001 (2014).
79 Shrivastava, S. & Schneider, M. F. Evidence for two-dimensional solitary sound waves in a lipid controlled interface and its implications for biological signalling. *Journal of the Royal Society, Interface* **11**, 20140098, doi:10.1098/rsif.2014.0098 (2014).
80 Pelling, A. E., Sehati, S., Gralla, E. B., Valentine, J. S. & Gimzewski, J. K. Local nanomechanical motion of the cell wall of Saccharomyces cerevisiae. *Science* **305**, 1147-1150, doi:DOI 10.1126/science.1097640 (2004).
81 Griesbauer, J., Bossinger, S., Wixforth, A. & Schneider, M. F. Propagation of 2D Pressure Pulses in Lipid Monolayers and Its Possible Implications for Biology. *Phys Rev Lett* **108**, doi:Artn 198103

10.1103/Physrevlett.108.198103 (2012).
82 Boyden, E. S., Zhang, F., Bamberg, E., Nagel, G. & Deisseroth, K. Millisecond-timescale, genetically targeted optical control of neural activity. *Nat Neurosci* **8**, 1263-1268, doi:10.1038/nn1525 (2005).
83 Curl, C. L. *et al.* Refractive index measurement in viable cells using quantitative phase-amplitude microscopy and confocal microscopy. *Cytom Part A* **65A**, 88-92, doi:10.1002/cyto.a.20134 (2005).
84 Liang, X. J., Liu, A. Q., Lim, C. S., Ayi, T. C. & Yap, P. H. Determining refractive index of single living cell using an integrated microchip. *Sensor Actuat a-Phys* **133**, 349-354, doi:10.1016/j.sna.2006.06.045 (2007).
85 Locke, M. *Cellular membranes in development*. Vol. 22 (Elsevier, 2012).
86 Andersen, S. S. L., Jackson, A. D. & Heimburg, T. Towards a thermodynamic theory of nerve pulse propagation. *Prog Neurobiol* **88**, 104-113, doi:10.1016/j.pneurobio.2009.03.002 (2009).
87 Ashkin, A., Dziedzic, J. M., Bjorkholm, J. E. & Chu, S. Observation of a single-beam gradient force optical trap for dielectric particles. *Opt Lett* **11**, 288 (1986).
88 Soughayer, J. S. *et al.* Characterization of cellular optoporation with distance. *Anal Chem* **72**, 1342-1347 (2000).
89 Vogel, A., Linz, N., Freidank, S. & Paltauf, G. Femtosecond-laser-induced nanocavitation in water: implications for optical breakdown threshold and cell surgery. *Physical review letters* **100**, 038102 (2008).
90 Schaffer, C., Nishimura, N., Glezer, E., Kim, A. & Mazur, E. Dynamics of femtosecond laser-induced breakdown in water from femtoseconds to microseconds. *Optics express* **10**, 196-203 (2002).

91 Kodama, T., Doukas, A. G. & Hamblin, M. R. Shock wave-mediated molecular delivery into cells. *Bba-Mol Cell Res* **1542**, 186-194, doi:Pii S0167-4889(01)00177-X

Doi 10.1016/S0167-4889(01)00177-X (2002).
92 Kodama, T., Hamblin, M. R. & Doukas, A. G. Cytoplasmic molecular delivery with shock waves. *Faseb J* **14**, A1473-A1473 (2000).
93 Nagel, G. *et al.* Channelrhodopsin-2, a directly light-gated cation-selective membrane channel. *Proc. Nat. Acad. Sci.* **100**, 13940-13945, doi:10.1073/pnas.1936192100 (2003).
94 Boyden, E. S., Zhang, F., Bamberg, E., Nagel, G. & Deisseroth, K. Millisecond-timescale, genetically targeted optical control of neural activity. *Nat Neurosci* **8**, 1263-1268 (2005).
95 Nagel, G. *et al.* Light Activation of Channelrhodopsin-2 in Excitable Cells of Caenorhabditis elegans Triggers Rapid Behavioral Responses. *Curr. Biol.* **15**, 2279-2284 (2005).
96 Miller, G. Optogenetics. Shining new light on neural circuits. *Science* **314**, 1674-1676, doi:314/5806/1674 [pii]

10.1126/science.314.5806.1674 (2006).
97 Hartong, D. T., Berson, E. L. & Dryja, T. P. Retinitis pigmentosa. *Lancet* **368**, 1795-1809 (2006).
98 Sugawara, T. *et al.* Relationship between peripheral visual field loss and vision-related quality of life in patients with retinitis pigmentosa. *Eye (Lond)* **24**, 535-539, doi:eye2009176 [pii]

10.1038/eye.2009.176 (2010).
99 Daiger, S. P., Bowne, S. J. & Sullivan, L. S. Perspective on genes and mutations causing retinitis pigmentosa. *Arch Ophthalmol* **125**, 151-158, doi:125/2/151 [pii]

10.1001/archopht.125.2.151 (2007).
100 Mezer, E. *et al.* Attitudes Regarding Predictive Testing for Retinitis Pigmentosa. *Ophthalmic Genetics* **28**, 9-15, doi:10.1080/13816810701199423 (2007).
101 Dhakal, K., Batabyal, S., Wright, W., Kim, Y.-t. & Mohanty, S. Optical delivery of multiple opsin-encoding genes leads to targeted expression and white-light activation. *Light: Science & Applications* **4**, e352 (2015).
102 Bi, A. D. *et al.* Ectopic expression of a microbial-type rhodopsin restores visual responses in mice with photoreceptor degeneration. *Neuron* **50**, 23-33, doi:DOI 10.1016/j.neuron.2006.02.026 (2006).
103 Thyagarajan, S. *et al.* Visual Function in Mice with Photoreceptor Degeneration and Transgenic Expression of Channelrhodopsin 2 in Ganglion Cells. *J. Neurosci.* **30**, 8745-8758, doi:10.1523/jneurosci.4417-09.2010 (2010).

104 Bi, A. *et al.* Ectopic expression of a microbial-type rhodopsin restores visual responses in mice with photoreceptor degeneration. *Neuron* **50**, 23-33, doi:S0896-6273(06)00176-0 [pii]

10.1016/j.neuron.2006.02.026 (2006).
105 Zhang, Y., Ivanova, E., Bi, A. & Pan, Z.-H. Ectopic Expression of Multiple Microbial Rhodopsins Restores ON and OFF Light Responses in Retinas with Photoreceptor Degeneration. *J. Neurosci.* **29**, 9186-9196, doi:10.1523/jneurosci.0184-09.2009 (2009).
106 Tomita, H. *et al.* Channelrhodopsin-2 gene transduced into retinal ganglion cells restores functional vision in genetically blind rats. *Experimental Eye Research* **90**, 429-436 (2010).
107 Tomita, H. *et al.* Visual Properties of Transgenic Rats Harboring the Channelrhodopsin-2 Gene Regulated by the Thy-1.2 Promoter. *PLoS One* **4** (2009).
108 Lagali, P. S. *et al.* Light-activated channels targeted to ON bipolar cells restore visual function in retinal degeneration. *Nat. Neurosci.* **11**, 667-675, doi:http://www.nature.com/neuro/journal/v11/n6/suppinfo/nn.2117_S1.html (2008).
109 Doroudchi, M. M. *et al.* Virally delivered Channelrhodopsin-2 Safely and Effectively Restores Visual Function in Multiple Mouse Models of Blindness. *Mol Ther* **19**, 1220-1229, doi:http://www.nature.com/mt/journal/v19/n7/suppinfo/mt201169s1.html (2011).
110 Cao, H., Gu, L., Mohanty, S. & Chiao, J. An Integrated microLED Optrode for Optogenetic Stimulation and Electrical Recording. *IEEE Trans Biomed Eng*, doi:10.1109/TBME.2012.2217395 (2012).
111 Kim, T. I. *et al.* Injectable, cellular-scale optoelectronics with applications for wireless optogenetics. *Science* **340**, 211-216, doi:340/6129/211 [pii]

10.1126/science.1232437 (2013).
112 Lin, J. Y., Knutsen, P. M., Muller, A., Kleinfeld, D. & Tsien, R. Y. ReaChR: a red-shifted variant of channelrhodopsin enables deep transcranial optogenetic excitation. *Nat Neurosci* **16**, 1499-1508, doi:10.1038/nn.3502 (2013).
113 Satpathy, S. *et al.* Broad spectral excitation of opsin for enhanced stimulation of cells. *Opt Lett* **40**, 2465-2468, doi:10.1364/OL.40.002465 (2015).
114 He, H., Nakagawa, K., Wang, Y., Hosokawa, Y. & Goda, K. Mechanism for microtsunami-induced intercellular mechanosignalling. *Nature Photonics* **9**, 623-623, doi:10.1038/nphoton.2015.164 (2015).

Biographical Information

Sarmishtha Satpathy was born and raised in Bhubaneswar, in the state of Odisha, India. She completed her schooling at D.A.V Public school, Chandrashekharpur, with an active interest in science and cocurriclulars. She then went on to do her B.Tech in Applied Electronics and Instrumentation from Silicon Institute of Technology, Bhubaneswar from 2007-2011. After completing her Bachelors, she came to University of Texas at Arlington, TX, USA to pursue MS in Electrical Engineering in 2012. She then went on to continue with her PhD, starting in 2014, after receiving her masters degree in 2013. She worked in the Biophotonics and Physiology group under Dr. Digant P. Dave' and Dr. Samarendra Ku. Mohanty. She actively worked in the area of optics tools for construction, control and detection of neural activity in circuits, with special interest in optical detection of action potentials. She received her PhD in Electrical Engineering from UT Arlington in December 2017. Sarmishtha plans to pursue her research in Biophotonics and optical techniques for biomedical application. She intends to continue her work in labelfree optical detection techniques in biomedical applications.